Strongly interacting electrons in Sachdev-Ye-Kitaev models and Twisted Bilayer Graphene

Proefschrift

ter verkrijging van
de graad van doctor aan de Universiteit Leiden,
op gezag van rector magnificus prof.dr.ir. H. Bijl,
volgens besluit van het college voor promoties
te verdedigen op dinsdag 7 januari 2025
klokke 13:00 uur

door

Aravindh Swaminathan Shankar
Geboren te Chennai, Indië
in 1996

Promotores:
Dr. V. Cheianov
Prof.dr. K.E. Schalm

Promotiecommissie:
Dr. V. Gritsev (Universiteit van Amsterdam)
Prof.dr. S. Vandoren (Universiteit Utrecht)
Prof.dr. C.W.J. Beenakker
Dr. S. Bhattacharya
Prof.dr. S.J. van der Molen

An electronic version of this Thesis can be found at
xxxxxxx

The cover represents two ways in which Hyperbolic geometries play a role in the low energy properties of electrons. The yellow curve represents the fermi surface near a van-Hove singularity and the random colored dots represent the SYK model. The graphics were made using the manim python package.

To my mentor, Prof. Lars Fritz

Contents

1

Introduction

The thesis will concern two topics of higher interest in current research. The first part of the thesis is on the Sachdev-Ye-Kitaev(SYK) model. The SYK model at its core is a model of a strongly interacting quantum dot with many flavors of electrons in it. Its rich solutions are targeted at explaining several unsolved problems in contemporary physics, including an elusive theory for the metallic phase of the cuprate high temperature superconductors. The second part of the thesis will tackle the classic problem of the Kondo effect in a modern setting of strongly interacting electrons: Twisted bilayer graphene (TBG).

As an artistic concept to which perhaps too much meaning should not be attached, we will see that underneath the description of both of these phenomena lies a hyperbolic geometry. In TBG, this will be identified in the hyperbolic Fermi surface contours. In the SYK model, the exotic physics will be described by the breaking of an emergent conformal symmetry, which can equivalently be described through the holographic duality by fluctuations of an Anti de-Sitter spacetime, which is the Lorentzian version of the Euclidean hyperbolic space.

1

1.1. Fermions, Fermi surfaces and quasiparticles

Condensed matter physics concerns the study of the quantum properties of matter. We know that solids are composed of atoms arranged in a crystalline structure. Their quantum description at its core is given by the many-body Schrodinger equation of all the electrons and ions that make up the solid, all interacting with each other. The first simplification one can make is to observe that the ions in a solid are composed of many protons and neutrons, and are much heavier than the electrons since $m_p/m_e \approx 2000$. Then the solid's low energy dynamics can be modeled by the motion of free electrons and their interactions with each other through the electromagnetic force, and with the vibrations of the lattice, known as phonons [1].

Schematically, in the language of second quantization, the Hamiltonian of the system of electrons can be written as

$$H = \underbrace{\sum_k \epsilon_k c_k^\dagger c_k}_{T} + \underbrace{\frac{g}{\Omega} \sum_{k,k',q} c^\dagger_{k+\frac{q}{2}} c^\dagger_{k'-\frac{q}{2}} c_k c_{k'}}_{V} \quad , \tag{1.1}$$

where the kinetic and potential energy terms have been separated out. In Eq. (1.1), ϵ_k refers to the dispersion of bare electrons subject to the symmetry of the lattice, and Ω is the volume of the system under consideration. For simplicity, all interactions that the electrons are subject to are schematically represented by the constant g, which may come from their charged interactions or with phonons or impurities etc. In a real material, the interaction itself may have a long range (and hence a momentum dependence), or may even face retardation effects, but these are neglected for now.

Let's first consider the kinetic energy term, given by T, and let us also suppose the bare parabolic dispersion of free electrons in the Galilean continuum. Just the fact that electrons are fermions obeying the Pauli exclusion principle means that the large density of free electrons in a metal each fill up the energy levels one by one, and the last few electrons to fill in would correspond to a gigantic energy scale. For example, in copper [2] which has an electron density of $8.47 \times 10^{28} m^{-3}$, the energy of the topmost occupied level turns out to be $7eV$, which corresponds to about $81600K$ in units of temperature. For reference, the surface of the sun is at a temperature of $5000K$.

This mammoth Fermi energy, which represents the magnitude of the kinetic energy in the total hamiltonian Eq. (1.1), is what is responsible in most cases to the success of Landau's Fermi liquid theory. Owing to the relative unimportance of the potential energy term, to lowest approximation, electrons can be considered to be completely non-interacting, from which weak interactions can be included perturbatively [3–5].

This can be understood mathematically using the language of Green's functions. Typically, the Green's function for free fermions has the defining feature of having

a pole whenever the frequency matches the energy of an excitation:

$$G^0(\boldsymbol{k},\omega) = \frac{1}{\omega + i\eta - \epsilon_{\boldsymbol{k}}}. \tag{1.2}$$

The physically accessible information here is the spectral function, which is the negative imaginary part of the self energy. As a function of frequency, this has a delta function peak at $\omega = \epsilon_k$.

When interactions are included, the Green's functions pick up a self energy according to the Dyson's equation:

$$G(\boldsymbol{k},\omega) = \frac{1}{\omega - \epsilon_{\boldsymbol{k}} - \Sigma(\boldsymbol{k},\omega)} \tag{1.3}$$

The self-energy will have a frequency and momentum dependence, and also a real and an imaginary part. We can expand the self-energy around a vector on the Fermi surface, at low frequencies

$$\Sigma(k,\omega) = \text{const} + k\frac{\partial\Sigma(k,0)}{\partial k}\bigg|_{k=k_F} + \omega\frac{\partial\Sigma(k_F,\omega)}{\partial\omega}\bigg|_{\omega=0} + \cdots. \tag{1.4}$$

We can use this to rewrite the Green's function in the form

$$\begin{aligned} G(k,\omega) &= \frac{1}{\omega\left(1 - \frac{\partial\Sigma}{\partial\omega}\right) - \left(\epsilon_{\boldsymbol{k}} + k\frac{\partial\Sigma}{\partial k}\right) + i\Gamma}, \\ &= \frac{Z}{\omega - \tilde{\epsilon_{\boldsymbol{k}}} + i\tilde{\Gamma}}, \end{aligned} \tag{1.5}$$

where the quasiparticle residue is given by

$$Z = \left(1 - \frac{\partial\Sigma(k_F,\omega)}{\partial\omega}\bigg|_{\omega=0}\right)^{-1}. \tag{1.6}$$

In this case, the spectral function which was a delta peak in the non-interacting case would just be shifted to the new position $\tilde{\epsilon_{\boldsymbol{k}}}$, and would be a relatively sharp Lorentzian of width $\tilde{\Gamma}$.

The success of Fermi liquid theory can be summarised succinctly by Eq. (1.5). The presence of weak interactions serves to simply broaden the fermion spectral functions by a small amount compared to the Fermi energy, and leads to long lived quasiparticles.

When the Taylor series expansion is valid, i.e. the self energy is analytic ($\Sigma \sim \alpha + \beta\omega + \gamma\omega^2 + \cdots$), the quasi-particle residue would be finite. With the discussion so far, we see that quasiparticles exist ubiquitously in the low energy description of weakly interacting systems of fermions for this simple reason.

However, this seems to not be the case in the normal state corresponding to a family of the cuprate high-Tc superconductors such as such as YBCO ($YBa_2Cu_3O_{7-x}$), LSCO

($La_{2-x}Sr_xCuO4$), and BSCCO($Bi_2Sr_2CaCu_2O_{8+x}$) among others. These compounds are of immense practical value as they are the among highest temperature superconductors, whose superconducting transition temperature T_c can be controlled by doping. The optimal doping where T_c is the highest, their normal states above T_c are characterized by an incoherent featureless spectral function at the antinodal directions indicating that there are no quasiparticles to be observed [6, 7]. Furthermore, this state, dubbed a strange metal, does not follow any of the phenomenological predictions of Fermi liquid theory. It is characterized a plethora of exotic features, the most prominent of which is a linear in temperature resistivity starting from the highest temperatures, all the way down to the superconducting transition temperature, and further down until the lowest measurable temperatures if superconductivity is suppressed by a magnetic field [8]. There are also measured anomalies in the frequency scaling of its optical conductivity [9, 10] and magnetotransport [11, 12] among others. We are thus interested in scenarios where the simple quasiparticle picture might not hold in order to better understand these "non-fermi liquids".

In order to break quasiparticles down, we need at least one of two things to happen: either their lifetime must be much shorter than their mean energy (so they would decay quite quickly by scattering), or the quasiparticle residue corresponding to the pole must vanish.

At this point, one can mention a proposal from the past [13–16]. The marginal or singular Fermi liquid, as the name suggests, is the most marginal way to create non-Fermi liquid behavior. Based on purely phenomenological terms, the linear term in the self energy is adjusted to include logarithmic corrections, which are weaker than the next leading (quadratic) term in the Taylor expansion.

The reason for doing this is as follows. If one supposes naively that the quasiparticle lifetime is the same as the scattering time that appears in the Drude model for electrical conductivity $\sigma = \frac{ne^2\tau}{m}$, with $\frac{1}{\tau} = \tilde{\Gamma}$ according to Eq. (1.5), and that if one attributes the temperature dependence of the dc resistivity of the normal states of the cuprate high Tc superconductors to a T-linear inverse quasiparticle lifetime $\tilde{\Gamma}$ at zero frequency, then based on dimensional analysis, one can expect the imaginary part of the electron self energy to be linear in frequency at low temperature, i.e. $\mathrm{Im}\,\Sigma = \pi\omega$. Correspondingly from the Kramers-Kronig relations which are needed for reasons of causality, the real part of the self energy can be calculated to be [17]

$$\mathrm{Re}\,\Sigma = \omega \log\left(\frac{\omega}{\omega_c}\right). \tag{1.7}$$

With this insight, we can understand the emergence of non-Fermi liquid behavior as a non-analytic behavior in the self energy, so that the quasiparticle residue vanishes, as seen from $\omega \to 0$ of Fig.1.1. This simple (albeit naive) consideration helps us

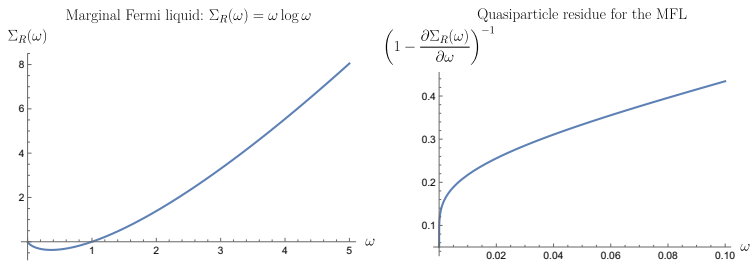

Figure 1.1: Absence of quasiparticles in the marginal Fermi liquid.

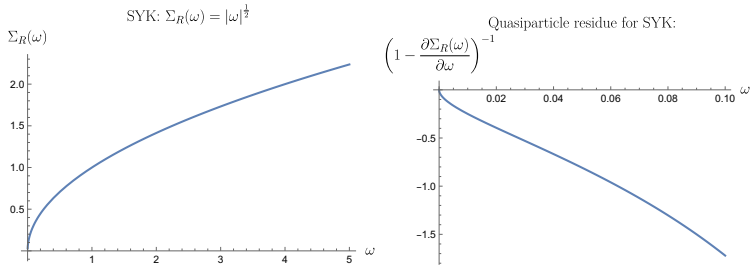

Figure 1.2: Absence of quasiparticles in the SYK model.

understand why the linear in T resistance of cuprates cannot come from any quasiparticle description of the underlying electrons. Even if we try to fit a pole with the imaginary part that is needed for the correct decay rate, causality itself would render its residue to vanish. The Green's function would now not have poles, but rather branch cuts on the ω axis.

The marginal Fermi liquid was constructed simply on phenomenological grounds, but it is of interest to construct some microscopic model which helps us understand the origin such a singular self energy. Such an example is the SYK model, whose self energy, as we shall see goes as $|\omega|^{1/2}$. It can be noted at this point that other examples of such power law self energies exist, such as near a quantum critical point in the Hertz-Millis theory of the ferromagnetic transition of itinerant electrons in a metal with $\Sigma \sim \omega^{2/3}$ [18].

For such a quantum critical scaling, the spectral function (which is the imaginary part of the retarded Green's function) diverges as a power law at low energy. The spectral function has an interpretation as the many body density of states. Specifically for the SYK model at zero temperature, the spectral function goes as $|\omega|^{-1/2}$. This can be contrasted with a phenomenon one can see even for dispersive free fermions in two dimensions, only interacting with a periodic lattice potential. Later in this thesis, we will see that if the band structure contains a higher order van Hove singularity, the density of states scales as $\rho(\omega) \sim \omega^{-1/4}$.

1

1.2. The SYK model

The SYK model describes the physics of interacting fermions living on a strongly disordered quantum dot. Its simplest version can be constructed using a Hamiltonian of N flavors of Majorana fermions interacting all-to-all with Gaussian random couplings.

$$H = \sum_{1\le i<j<k<l\le N} J_{ijkl}\,\psi_i\psi_j\psi_k\psi_l \tag{1.8}$$

The random couplings are normally distributed, i.e

$$\langle J_{ijkl}\rangle = 0 \tag{1.9}$$

$$\left\langle J^2_{ijkl}\right\rangle = \frac{6J^2}{N^3}. \tag{1.10}$$

Henceforth, we will switch to Euclidean time (and imaginary frequencies). The free part of the Green's function is (with the normalization $\{\psi_i,\psi_j\} = \delta_{ij}$)

$$\begin{aligned} G^0_{ij}(\tau) &= -\left\langle \mathscr{T}\psi_i(\tau)\psi_j(0)\right\rangle, \\ &= -\frac{1}{2}\,\mathrm{sgn}(\tau)\,\delta_{ij}. \end{aligned} \tag{1.11}$$

In Fourier space,

$$G^0(\omega) = \int \mathrm{d}\tau\, e^{i\omega\tau} G^0(\tau) = \frac{1}{i\omega}. \tag{1.12}$$

1.2.1. The SYK self consistent equations

We can now turn to look at the diagrams that dress the fermion Green's functions upon turning on interactions. The disorder average enforces that the flavors of the four Majoranas at both the connecting vertices are identical, and simultaneously brings out a contribution $\sim \frac{J^2}{N^3}$ for each vertex pair. This means that in order for this diagram to not be suppressed in the large N limit, only diagrams which have three free intermediate lines summed over for each pair of vertices can survive. All these constraints restrict the set of diagrams that survive at leading order in large N to be just the melon diagrams shown in Fig. 1.3, and the Green's function takes the form $G_{ij}(\tau) = G(\tau)\delta_{ij}$.

With these considerations, the Dyson's equations can be represented as

This gives us the SYK equations:

$$(G(\omega))^{-1} = i\omega - \Sigma(\omega)\,, \tag{1.13}$$

$$\Sigma(\tau) = J^2\,(G(\tau))^3\,. \tag{1.14}$$

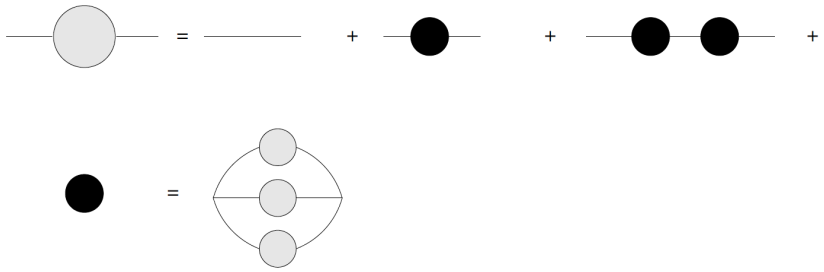

Figure 1.3: Summing the Dyson series. Figure used from Ref. [19]. The filled black dot represents the only self energy diagram that survives in the large N limit.

These are a set of equations that must be solved self-consistently: eq.(1.13) tells how the self-energy determines the Green's function, and eq.(1.14) says how the self-energy is set by the Green's function. They are not the most trivial to solve, since one is in real space, and the other in Fourier space.

The key to doing so is to assume that the self-energy dominates the free propagator's contribution at strong coupling in the IR ($\omega \to 0$). Then, eq.(1.13) can be written as

$$\int d\tau' G(\tau,\tau')\Sigma(\tau',\tau'') = -\delta(\tau-\tau''). \tag{1.15}$$

This is solved by the ansatz

$$G_c(\tau) = \frac{b\,\mathrm{sgn}(\tau)}{|\tau|^{2\Delta}}. \tag{1.16}$$

Eq. (1.16) is the form of the Green's function of a conformal field theory (CFT), and commutes with all the generators of the conformal transformations in $0+1$ dimensions [20]. The scaling dimension Δ can be easily determined by a consistency condition that $\tau \to b\tau$ should satisfy simultaneously Eq. (1.14), (which would indicate that the self energy would need to scale as $\tau^{-6\Delta}$) and Eq. (1.15).

$$\begin{aligned} b^{1-2\Delta-6\Delta} &= b^{-1}, \\ \implies \Delta &= \frac{1}{4}. \end{aligned} \tag{1.17}$$

We can see again from simple dimensional analysis how the Green's function Eq. (1.16) scales as a function of frequency. The Fourier transformation

$$\int_{-\infty}^{\infty} d\tau e^{i\omega\tau} \frac{\mathrm{sgn}(\tau)}{|\tau|^{2\Delta}} \sim |\omega|^{2\Delta-1}, \tag{1.18}$$

yields the branch-cut propagator result of $\Sigma(\omega) \sim |\omega|^{1/2}$, as promised, and we have with us a microscopic model for the breakdown of quasiparticles.

1

1.3. Other versions of the SYK used in this thesis

It would be quite a fallacy to limit one's understanding of the physics of the SYK model to simply an artificial description of Majorana fermions in quantum dots - in fact, the original UV-completion of the SYK model was described by a random heisenberg coupled spin system [21].

Rather, its physical content describes the emergence and the weak breaking of a new conformal symmetry in the infrared. In this section, we will describe some generalizations of the SYK model to include different kinds of degrees of freedom, which will be an emphasis of the fact that this class of models should be thought of as a description of a new IR fixed point.

1.3.1. Complex SYK

The first generalization of the SYK fixed point that we will will consider is one that has a UV-completion that includes a conserved U(1) charge using complex fermions. This will be appropriately called the "complex-SYK" model [22, 23]. The hamiltonian will be written as

$$H = \frac{1}{(2N)^{3/2}} \sum_{ijkl=1}^{N} J_{ij;kl} c_i^\dagger c_j^\dagger c_k c_l - \mu \sum_{i=1}^{N} c_i^\dagger c_i \,. \tag{1.19}$$

In this UV hamiltonian, the total charge is simply given by

$$Q = \frac{1}{N} \sum_i \left\langle c_i^\dagger c_i \right\rangle . \tag{1.20}$$

At $\mu = 0$, the model is at half filling, and $Q = \frac{1}{2}$ in this notation.

Similar to the Majorana SYK, this model also permits a conformally invariant IR, with exactly the same scaling dimension $\delta = \frac{1}{4}$. The infrared for the $\mu = 0$ case of the complex SYK model is indistinguishable from the Majorana SYK model in terms of the effective $G - \Sigma$ theory, in that the Green's functions are identical in the two cases.

At finite μ, the effect of having a finite amount of charge is also indirectly felt by the infrared Green's functions, in the form of $G(\tau = 0^-) = Q$. This is shown in Fig. 1.4 by the asymmetry between $|G(\tau = 0^-)|$ and $\left|G(\tau = 0^+)\right|$. The Schwinger-Dyson equations in this case become [22]

$$G(i\omega_n) = \frac{1}{i\omega_n + \mu - \Sigma(\omega_n)} \tag{1.21a}$$

$$\Sigma(\tau) = -J^2 G^2(\tau) G(-\tau) \tag{1.21b}$$

For a solution of these equations to exist, one needs that $\Sigma(\omega_n \to 0) = \mu$, and at low energy and low temperatures it is solved by the same power law form. Then in that

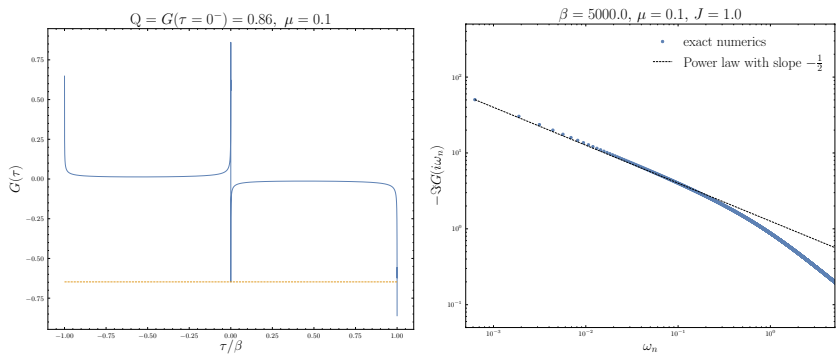

Figure 1.4: Imaginary time solutions to the Schwinger-Dyson equations for the complex SYK model Eq. (1.24d). Left: Asymmetry at $\tau = 0$ in the case of a non-zero chemical potential, which measures the total charge. Right: Power law solution for $G(\omega_n)$ at low temperatures and low frequencies with the same scaling dimension as the Majorana SYK case, even with a finite chemical potential.

case, indeed one finds that there is a scaling solution to Eqs. (1.21b) with the exponent $2\Delta - 1$, with $\Delta = \frac{1}{4}$ as before.

1.3.2. Yukawa-SYK model

The SYK model can also be generalized to include bosonic degrees of freedom. The Yukawa SYK (YSYK) model can be thought of as a zero dimensional analogue of the electron-phonon coupling Hamiltonian. This has been the subject of intense theoretical study in recent years [24–32]. The model also allows for a generalization into higher dimension for a recently proposed universal theory of strange metals [33–38] by being able to have a controlled large-N limit overcoming previous challenges [39].

The Hamiltonian for the Yukawa SYK is very reminiscent of the Fröhlich or the Bardeen-Pines Hamiltonian for the electron-phonon interaction and can be written as

$$H_{Y-SYK} = -\mu \sum_{i=1}^{N} \sum_{\sigma} c^{\dagger}_{i,\sigma} c_{i,\sigma} + \sum_{k=1}^{M} \frac{1}{2} \left(\pi_k^2 + \omega_0^2 \phi_k^2\right) + \frac{\sqrt{2}}{N} \sum_{i,j,k} \sum_{\sigma} g_{ijk} c^{\dagger}_{i,\sigma} c_{j,\sigma} \phi_k. \quad (1.22)$$

The are N flavors of fermions, and M flavors of bosons, and we are interested in the regime when both $N \to \infty, M \to \infty, \kappa = \frac{M}{N}$ held constant.

In the absence of time reversal symmetry, for the Hamiltonian to be hermitian, the couplings $g_{ij,k}$ have to satisfy

$$g_{ji,k} = g^{*}_{ij,k}, \quad (1.23)$$

and are drawn from the Gaussian unitary ensemble (GUE). At zero temperature, the low energy theory in this case is completely akin to the conventional SYK non-Fermi

liquid, and develops an emergent conformal symmetry, with a scaling dimension set by κ. The Schwinger-Dyson equations in this case read

$$\Sigma(\tau) = \kappa\, g^2\, G(\tau) D(\tau) \tag{1.24a}$$

$$\Pi(\tau) = = -2g^2\, G(\tau) G(-\tau) \tag{1.24b}$$

$$G(i\omega_n) = \frac{1}{i\omega_n + \mu - \Sigma(i\omega_n)} \tag{1.24c}$$

$$D(i\nu_n) = \frac{1}{\nu_n^2 + \omega_0^2 - \Pi(i\nu_n)}. \tag{1.24d}$$

The model is self-tuning to criticality [24], i.e the bosons modes soften in the infrared. This is the condition that at zero temperature, $\Pi(\omega = 0) = \omega_0^2$. In the infrared, we can obtain a non-Fermi liquid solution by making use of the zero-temperature conformal ansatz

$$G(\tau) = b \frac{\mathrm{sgn}(\tau)}{|\tau|^{2\Delta_f}}, \tag{1.25}$$

$$D(\tau) = d \frac{1}{|\tau|^{2\Delta_b}}. \tag{1.26}$$

For $\kappa = 1$, we obtain the scaling dimensions $\Delta_f = 0.420374$, and $\Delta_b = 0.159252$.

At finite temperature, the model exhibits a rich phase diagram first outlined in Ref. [24]. For $g < 1$, the highest temperatures are characterized by a limit of free fermions, where $G(\omega_n) \to \frac{1}{i\omega_n}$, and the low temperature phase is the finite temperature version of the non-Fermi liquid described above. The $g > 1$ regime is characterized by a novel impurity like phase at intermediate and high temperature. This is shown pictorially in Fig. 1.5.

In the presence of time reversal symmetry(TRS), the couplings in Eq. (1.22) are further constrained to be completely real, and $g_{ij,k}$ have to be drawn from the Gaussian orthogonal ensemble (GOE). This changes the ground state quite starkly, and the system is now described by a superconducting state. The reason for the reappearance of superconductivity on restoration of TRS can be most easily understood in analogy with the BCS case with $s-$ wave pairing. There, the electrons choose to pair with zero center of mass momentum, i.e. the state on the Fermi surface with momentum $\boldsymbol{k}$ pairs with its time reversal partner: the state with momentum $-\boldsymbol{k}$. The statement of TRS is that $E(\boldsymbol{k}) = E(-\boldsymbol{k})$, so both states required for pairing lie on the Fermi surface. It is obvious then that the breaking of TRS will lead to a reduction of phase space for pairing, and hence diminishing superconductivity.

As an aside, another loose argument for this is that the broken time reversal symmetry can be thought of as introducing an artificial magnetic field, and the introduction of a magnetic field is the canonical way to suppress superconductivity.

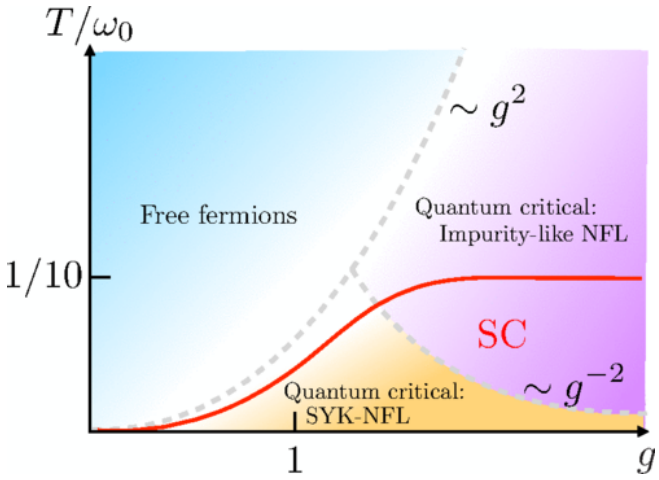

Figure 1.5: Phase diagram of the Yukawa SYK model. Figure used from Ref. [24].

Coming back to the Yukawa SYK model, the restoration of TRS introduces a form of strong coupling superconductivity at low temperatures, and the equations of motion become the quantum critical Eliashberg equations [40–43]. This is a model of superconductivity betrothed to a quantum critical point, and is expected to be of importance in the study of the cuprate superconductors. In this case, the non-Fermi liquid metallic phase becomes difficult to observe as it competes with the superconducting phase. The reason for this is that the temperature scale in which non-fermi liquid effects set in is parametrically the same as that at which superconductivity sets in, but however there might be a numerical prefactor which separates the two. However, one may interpolate between the TRS preserving and TRS breaking situations by linearly interpolating between the GOE and GUE ensembles, which has the effect of lowering T_c from its maximum value.

In Chapter 3 of this thesis, we will explore what happens when we couple two quantum critical superconductors through a weak link as is done conventionally [44] and calculate the resulting Josephson current. We will see that this very coupling will be responsible for a wormhole-like state on the dual gravitational side.

1.3.3. b-SYK

Given the importance of the SYK model, attempts have been made in order to realise it in an experimental situation. A comprehensive list of these attempts is provided in the recent review [45].

We will here first specifically mention Ref. [46] using graphene flakes (more will be said about graphene in Sec. 1.5 below). It is well known in graphene that the presence

of a strong magnetic field induces the formation of Landau levels, the lowest of which is pinned to zero energy. This completely flat band quenches the kinetic energy in Eq. 1.1. The wavefunctions have non-trivial quantum geometry still and instead of being localized, are extended throughout the surface of the graphene. There is a zero mode generated for every quantum of flux that penetrates the sample, as is well known from the theory of the quantum hall effect.

The effects of the coulomb interaction projected onto the degenerate states of the flat band, next nearest neighbor hoppings and random onsite disorder all contribute to make the effective interactions seem almost completely random.

To provide evidence that the Hamiltonian thus generated is SYK like, the authors of Ref. [46] took recourse to random matrix theory. They first calculated the coupling constants of the projected graphene Hamiltonian by explicit numerical diagonalization as a function of flux. They observed with increasing flux that as a new zero mode was added, the distribution of couplings changed random matrix universality class, in close analogy to the Altland-Zirnbauer classification for non-interacting Hamiltonians [47–49], and this matches perfectly with the random matrix classes as a function of the number of fermions in the SYK model [50–52].

A similar idea was used by Fremling and Fritz [53] to propose an experimental realization of a Majorana version of the SYK model. They consider the Kitaev honeycomb model of spins [54], which is believed to be realized in many spin liquid candidates including the iridates like Na_2IrO_3, $H_3LiIr_2O_6$ and more prominently in $\alpha - RuCl_3$ [55, 56]. The low energy theory of the Kitaev honey comb model exhibits deconfinement of the spins into Majorana fermions. Fremling and Fritz noted that an analogue of a strong magnetic field creating flat Landau levels could be simulated by application of triaxial strain, and the remnant interactions in these materials, for instance the heisenberg interaction, projected onto these Majorana zero modes resulted in an SYK-like interaction.

The catch, however, is that unlike the complex fermion case in the graphene flakes, these residual interactions are only non-vanishing for pairs of Majoranas on opposite sublattices of the bipartite honeycomb lattice(see Fig.1.6). This leads to the emergence of the so-called bipartite SYK model (b-SYK), whose Hamiltonian is given by

$$H_{b-SYK} = \frac{1}{4}\sum_{i,j=1}^{N_A}\sum_{\alpha,\beta=1}^{N_B} J_{ij\alpha\beta}\psi_i^A\psi_j^A\psi_\alpha^B\psi_\beta^B. \tag{1.27}$$

Again, the couplings have some sense of Gaussianity:

$$\left\langle J_{ij\alpha\beta}J_{i'j'\alpha'\beta'}\right\rangle = \frac{J^2}{2\sqrt{N_AN_B}^3}\delta_{i,i'}\delta_{j,j'}\delta_{\alpha,\alpha'}\delta_{\beta,\beta'} \tag{1.28}$$

Here, N_A and N_B are the number of sites in the $A-$ and $B-$ sublattice respectively, and need not be the same in a disordered system.

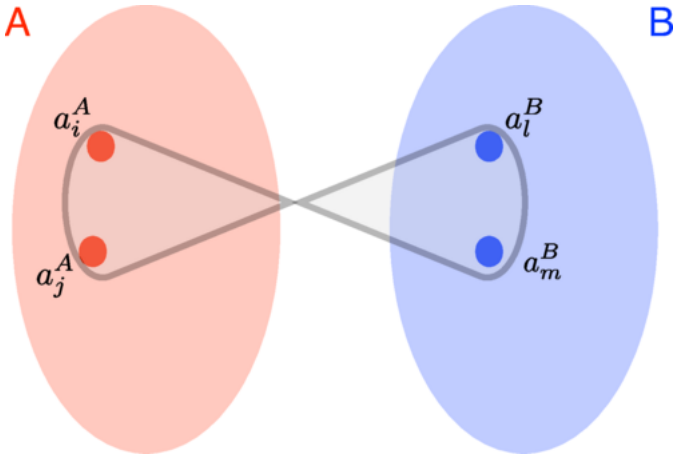

Figure 1.6: Schematic of the b-SYK model. There are 2 sets of Majorana fermions living on each of the two bipartite lattices of the honeycomb lattice. The interactions of the model are such that the Majoranas do not interact within a set, but every pair of Majorana degrees of freedom in each set interacts with a Gaussian random coupling with every pair of Majoranas on the other set. Figure from Ref. [57].

Although the new model in eq. 1.27 contains only 3/8 of the non-zero couplings as the full all-to-all SYK model, it still shows an emergent conformal symmetry at low energy, with a different tunable conformal dimension for the Majoranas in each set [57]. Such generalizations of the SYK model created by repeated pruning of the fully connected graph of couplings falls into the family of the so called "sparse SYK" models [58–61].

1.4. Holographic dual of the SYK model and $N-AdS_2$ spacetime

The correct path integral representation of the SYK effective action is given in terms of a two-time formalism, and the time-translation invariant solution Eq.(1.16) only represents the classical saddle. The disorder averaged path integral can be written as

$$S = -\log\det\left(\partial_\tau + \Sigma(\tau,\tau')\right) - \int d\tau d\tau' G(\tau,\tau')\Sigma(\tau,\tau') + \frac{J^2}{4}G(\tau,\tau')^4. \tag{1.29}$$

Without imposing time-translation symmetry, the saddle point equations would be Eq. (1.15) and the self energy equation Eq. (1.14) rewritten to be

$$\Sigma(\tau,\tau') = J^2\left[G(\tau,\tau')\right]^3. \tag{1.30}$$

It was observed that these set of equations in the fully conformal limit possessed an additional emergent symmetry of time reparametrizations [19, 22, 62]. This means

that for every solution $G(\tau,\tau'),\Sigma(\tau,\tau')$ that solves Eqs. (1.15) and (1.30), one can get yet another solution by picking an arbitrary function $f(\sigma)$ to obtain another function pair of functions $\tilde{G}(\sigma,\sigma'),\tilde{\Sigma}(\sigma,\sigma')$ such that

$$G(\tau,\tau') = \frac{1}{\left|f'(\sigma)f'(\sigma')\right|^{\Delta}}\tilde{G}(\sigma,\sigma') \tag{1.31}$$

$$\Sigma(\tau,\tau') = \frac{1}{\left|f'(\sigma)f'(\sigma')\right|^{1-\Delta}}\tilde{\Sigma}(\sigma,\sigma') \tag{1.32}$$

that also satisfies the same equations Eqs. (1.15) and (1.30).

It turns out that starting from the conformal solution Eq. (1.16)

$$G_c(\tau,\tau') = b\frac{\mathrm{sgn}(\tau-\tau')}{|\tau-\tau'|}^{2\Delta}, \tag{1.33}$$

and picking a function from the SL(2,R) group i.e. $\tau = f(\sigma) = \frac{a\sigma+b}{c\sigma+d}$ with $ad-bc=1$, leaves the saddle point solution invariant, i.e. $G_c(\tau,\tau') = \tilde{G}_c(\sigma,\sigma')$.

For any other choice of the function f, we get new solutions to the saddle point equations , in fact infinitely many of them. This is an artifact of the far infrared limit, and the physical solution is determined by the function that minimizes the UV $i\omega$ term that has been neglected in the full action. This turns out to be the zero temperature scaling solution that we have written down. This is a motivation for an effective field theory for fluctuations around the SYK far infrared conformal fixed point - we simply write down an action with the fewest number of derivatives that vanishes for $f(\tau)$ in the SL(2,R) group. This is termed the Schwarzian action [19, 62]

$$S = \alpha_s\int d\tau\,\{f(\tau),\tau\}, \quad \{f(\tau),\tau\} = \frac{f'''}{f'} - \frac{3}{2}\left(\frac{f''}{f'}\right)^2, \tag{1.34}$$

and is the correct low energy theory of the breaking of conformal symmetry in the SYK model. The constant α_s in front is non-universal and can be fixed from either thermodynamics or the numerical evaluation of the four point function in the full UV-complete theory.

We will consider one special choice of time reparametrization: $\tau = f(\sigma) = \tan\frac{\pi\sigma}{\beta}$. Written in this way, it is clear that the coordinate σ represents a circle from 0 to β in imaginary time. Hence the propagator that we must obtain on using this in Eq. (1.32) should represent the Green's function of the IR limit of the SYK model when it is put at a finite temperature β. Doing the algebra, we see that

$$\begin{aligned}\tilde{G}(\sigma,\sigma') &= \left(\frac{\pi}{\beta}\right)^2\left(\sec\left(\frac{\pi\sigma}{\beta}\right)\sec\left(\frac{\pi\sigma'}{\beta}\right)\right)^{2\Delta} b\frac{\mathrm{sgn}(\sigma-\sigma')}{\left|\tan\left(\frac{\pi\sigma}{\beta}\right)-\tan\left(\frac{\pi\sigma'}{\beta}\right)\right|^{2\Delta}} \\ &= b\frac{\mathrm{sgn}(\sigma-\sigma')}{\left|\frac{\pi}{\beta}\sin\left(\frac{\pi}{\beta}(\sigma-\sigma')\right)\right|^{2\Delta}},\end{aligned} \tag{1.35}$$

where we used in the last step that $\cos x \cos y(\tan x - \tan y) = \sin x \cos y - \cos x \sin y = \sin(x-y)$. This particular choice of the function f is not in the SL(2,R) group, and will contribute non-trivially to the action in eq. (1.34). The Schwarzian derivative itself for this case can be calculated to be $\frac{2\pi^2}{\beta^2}$, and that is equal to the finite temperature correction to the free energy. This directly implies that the low temperature entropy will be of the linear Sommerfeld form.

There is a remarkable connection between SYK systems and black holes in general relativity though a holographic duality. In some aspects, the behavior of the two parallel each other. The rest of this section is dedicated to explaining how this can be.

The Schwarzian action is also the minimal action that describes the propagation of a boundary graviton in a 2 dimensional nearly Anti de Sitter spacetime (N-AdS_2) [45, 63]. The reasoning is the following. In Euclidean signature, this is just a hyperbolic space with the metric

$$ds^2 = \frac{dt^2 + dz^2}{z^2}. \tag{1.36}$$

When one wants to study a finite part of the space, we want to cut it off along a boundary curve specified by $t(u), z(u)$, where the affine parameter u is a local time coordinate on this curve. Staying ϵ away from the boundary at $z = 0$ of and studying only curves of a fixed length, leaves still a choice of $t(u)$ being arbitrary, and different choices should correspond to different boundary curves. However, AdS_2 being a maximally symmetric space has SL(2,R) as an isometry, and different curves generated by

$$\tilde{t}(u) = \frac{at(u)+b}{ct(u)+d}, \quad ad - bc = 1. \tag{1.37}$$

all map on to each other, and other choices of reparametrizations of $t(u)$ correspond to fluctuations of the boundary spacetime, hence describing a boundary graviton.

It turns out that just simple AdS_2 spacetime is non-dynamical, in that the Einstein-Hilbert action is identically zero for all metric configurations since gravity in two dimensions is topological. To have a meaningful gravity theory, one needs to look at nearly AdS_2 or $N-AdS_2$ spaces, which are described by dilatonic theories of gravity, called the Jackiw-Teitelboim (JT) gravity [64, 65] with the action

$$S = -\frac{1}{16\pi G}\left[\int d^2x\phi\sqrt{g}(R+2) + 2\int_{\partial M}\phi_b K\right] \tag{1.38}$$

with a dynamical dilaton field ϕ that acts as an effective Newton's constant.

From similar arguments made for the SYK case, with the reparametrization symmetry acting in this case as eq. (1.37), the low energy effective action describing the propagation of the boundary graviton of this nearly AdS_2 space will once again be exactly the Schwarzian action.

1

We will take a moment to show how an N-AdS_2 space can come from a reduction from a higher dimensional space. In the process, we will uncover intuition for the role played by black holes in AdS_2 in regards to their dual field theories being at finite temperature.

According to the holographic duality [66–69], there is a dictionary that maps conformal field theories to spacetime geometries. The precise statement of this duality is that the partition functions of the boundary CFT and the bulk geometry are equal to each other. When we want to describe the boundary theory at a finite temperature, it has to it an associated entropy, simply from the fundamental laws of thermodynamics. The empty AdS metric described in Eq. (1.36) does not have any entropy at all. Its is known from the work of Bekenstein [70], that the only what that spacetime geometry can have either an entropy or a temperature is if it had a black hole in it. The entropy then is proportional to the area of the black hole's event horizon, and the temperature is given by the Hawking temperature.

We shall briefly sketch how this works in practice by considering an explicit example [22, 71, 72]. Let us consider the Reissner-Nordstrom(RN) metric for planar black holes in asymptotic AdS_{d+2}. The metric from the solutions of Einstein's equations is given by

$$ds^2 = \frac{r^2}{R^2}\left(-f\,dt^2 + d\boldsymbol{x}^2\right) + \frac{R^2}{r^2}\frac{dr^2}{f}, \tag{1.39}$$

where R is the radius of AdS_{d+2}, and with the emblackening factor

$$f = 1 + \frac{\Theta^2}{r^{2d}} - \left(r_0^{d+1} + \frac{\Theta^2}{r_0^{d-1}}\right)\frac{1}{r^{d+1}}. \tag{1.40}$$

The quantity Θ is proportional to the charge in the boundary theory, but we will not write it explicitly here for simplicity, for our current purposes we can just treat it as a constant. The black hole horizon is where the metric component g_{tt} vanishes, and hence $f = 0$ implies that the horizon is at $r = r_0$ in these coordinates.

The Hawking temperature is determined by the surface gravity, which is the amount of acceleration a body needs to be at rest just near the horizon. For this Reissner Nordstrom metric in Eq. 1.39, it is given by [22, 71]

$$T = \frac{(d+1)r_0}{4\pi R^2}\left(1 - \frac{(d-1)\Theta^2}{(d+1)r_0^{2d}}\right). \tag{1.41}$$

We can observe that the Hawking temperature is zero when the horizon is at a position $r_0 = r_*$, such that

$$\Theta^2 = \frac{d+1}{d-1}r_\star^{2d}. \tag{1.42}$$

At exactly this location of the horizon, we can look at the near horizon limit of Eq. (1.40), buy expanding

$$r = r_* + \frac{1}{\zeta} \tag{1.43}$$

for leading order in ζ. The metric that we arrive at then is

$$ds^2 = \underbrace{R_2^2 \frac{-dt^2 + d\zeta^2}{\zeta^2}}_{AdS_2} + \underbrace{\frac{r_*^2 d\boldsymbol{x}^2}{R^2}}_{\mathbb{R}^d}, \tag{1.44}$$

and we see that the metric has factorized into $AdS_2 \times R^d$. We have also expressed an effective AdS_2 radius in terms of the radius of the full AdS_{d+2} space as $R_2^2 = \frac{R^2}{d(d+1)}$. This can be compared with Eq. 1.36, only here we have the Minkowski signature.

When the position of the horizon moves slightly away from $r_0 = r_*$,, the boundary field theory would be at a finite temperature. We can repeat the procedure sketched above to see what would happen to the near horizon geometry in that case.

We parameterize the small shifts in the following way, First we move the Reissner Nordstrom horizon (which is always at $r = r_0$) a small distance away from where it was :

$$r_0 - r_* = \frac{1}{\zeta_0}, \tag{1.45}$$

and then we restrict r to be near the horizon

$$r - r_* = \frac{1}{\zeta}. \tag{1.46}$$

In practical terms, this is convenient to do by starting with Eq. (1.39), expanding r and r_0 about r_* using the parameterizations in Eqs.(1.46) and (1.45) up to second order each, and then taking the limit $r_* \to \infty$. We arrive then with the following elegant result

$$ds^2 = \frac{R_2^2}{\zeta^2}\left[-\left(1 - \frac{\zeta^2}{\zeta_0^2}\right)dt^2 + \frac{d\zeta^2}{\left(1 - \frac{\zeta^2}{\zeta_0^2}\right)}\right] + \frac{r_*^2}{R^2} d\boldsymbol{x}^2. \tag{1.47}$$

This represents a black hole in AdS_2 with an emblackening factor such that the horizon is at $\zeta = \zeta_0$. Furthermore, this metric has a Hawking temperature of $T = \frac{1}{2\pi\zeta_0}$. We can see that in order to have finite temperature in the boundary, we need to have a black hole in the bulk AdS_2.

Black holes have yet another property. They are the fastest scramblers of quantum information. [73–78]. The notion of quantum chaos is connected to the growth of a

out of time ordered correlators. This is a measure of the failure of two operators to commute with each other.

In classical mechanics, the amount of chaos in a system is quantified by the Lyapunov exponent. It is a measure of how quickly two trajectories that are close together at the start can diverge as the system evolves under its chaotic dynamics.

$$\begin{aligned}\{x(t), p(0)\} &= \frac{\delta x(t)}{\delta x(0)}, \\ &= e^{\lambda_L t}.\end{aligned} \tag{1.48}$$

In quantum mechanics, we have a quantity that grows as the squared commutator. Given a system, we can define it using two general operators $\hat{W}$ and $\hat{V}$ that are constructed using its degrees of freedom. It can be written as [76]

$$C(t) = \left\langle \left[\hat{W}(t), \hat{V}(0)\right] [W(t), V(0)]^{\dagger} \right\rangle_{\beta}. \tag{1.49}$$

Initially at time $t = 0$, the operators are far away, in the sense that they have no overlap. They only have support on different states in the Hilbert space. The squared commutator measures the failure of these to commute at a later time t.

Expanding the squared commutator results in four terms, two of which are normal time ordered, and two of which are out of time ordered. The part of the squared commutator that grows over time are really the out of time ordered ones, appropriately regularized [79] is called the OTOC, and is the quantity that grows exponentially in a chaotic system. For the SYK model, this property can be used to define the quantum Lyapunov exponent as [19].

$$\begin{aligned}\text{OTOC}(t) &= \frac{1}{N^2} \left\langle \psi_i(t)\psi_j(0)\psi_i(t)\psi_j(0) \right\rangle \\ &\sim \frac{1}{N} e^{\lambda_L t}.\end{aligned} \tag{1.50}$$

It was found that the OTOC defined in this way placed a bound on the Lyapunov exponent [73]. The bound can be stated as follows - at a finite temperature T,

$$\lambda_L \leq 2\pi T. \tag{1.51}$$

Black holes are known to saturate this bound, and this property is known as fast scrambling. They do so in the following way [74, 75]. In a spacetime with two boundaries [80] where general relativity applies, dropping particles into the space from one boundary causes a shockwave to propagate in the bulk, the proper energy of which grows exponentially with time, at a rate given by the maximal Lyapunov exponent.

The Lyapunov exponent can be calculated for the SYK model by evaluating the four point function in Eq. (1.50), and in the deep infrared, it can also be shown to saturate the chaos bound Eq. 1.51. This can be traced back to both systems having a

Schwarzian mode [19]. The fact that the chaos bound is saturated by both the SYK model and the black hole geometry adds to the evidence that the two models possess a duality of some kind. We will study what happens to the Lyapunov exponent in the b-SYK model of Sec. 1.3.3 in chapter 2.

We complete the circle by returning to the cuprates. The superconducting transition temperature in these materials by a semi-empirical law to inverse the relaxation time of their normal state just above T_c. Ref. [81] argues that the propensity of these materials to dissipate energy at a rate which exactly turns out to be λ_L^{-1} in appropriate units after adding in the missing $\hbar$ and k_B is what renders them with their high T_c.

Having understood the components of the SYK model in sufficient detail, we will now move to yet another scenario where we have an instance of strongly interacting quantum matter, but with its physics instead being engendered by a completely different kind of hidden hyperbolic geometry.

1.5. Graphene and its bilayers

Graphene is a single sheet of carbon atoms arranged in a hexagonal lattice [82]. Its electronic properties can be described by a simple tight binding model which accounts for electrons hopping between nearest neighbors in its two sublattices, with its Hamiltonian given by

$$H = -t \sum_{\langle i,j \rangle} a_i^\dagger b_j + h.c, \tag{1.52}$$

and can be diagonalized in terms of two component wavefunctions

$$\Psi_i = \begin{pmatrix} a_i \\ b_i \end{pmatrix}. \tag{1.53}$$

to obtain a spectrum given by

$$E(\boldsymbol{k}) = \pm \sqrt{1 + 4\cos\left(\frac{3k_x a}{2}\right)\cos\left(\frac{\sqrt{3}k_y a}{2}\right) + 4\cos^2\left(\frac{\sqrt{3}k_y a}{2}\right)} \tag{1.54}$$

The dispersion in Eq. (1.54) shows interesting features at the K, K' and the M points of the Brillouin zone(see Fig. 1.7).

The K point and its time reversed partner K' points are referred to as Dirac points. This is because the gap between the two bands closes at these points, and the dispersion is linear. Indeed, the low energy Hamiltonian close to for momenta $\boldsymbol{p}$ close to the K point can be represented as

$$H = v_F \, \boldsymbol{p} \cdot \boldsymbol{\sigma}. \tag{1.55}$$

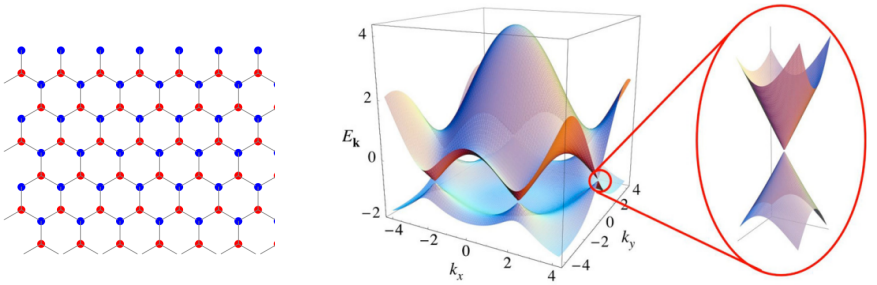

Figure 1.7: Left: Schematic hexagonal lattice of graphene showing carbon atoms in the A(red) and B(blue) sublattices. Right: Dispersion with zoom near the band-touching Dirac point (this panel taken from Ref. [82]).

The Dirac matrices in two dimensions are simply the $2x2$ Pauli matrices given by $\boldsymbol{\sigma}$. The corresponding dispersion $E(\boldsymbol{p}) = v_F|\boldsymbol{p}|$ is dubbed a Dirac cone, because it looks like a causal light cone from special relativity, just with an effective speed of light v_F.

Graphene also has an interesting saddle-like dispersion near its M point. This can be seen in Figs.1.8 and 1.7. Since first derivatives vanish at a saddle point by definition, the dispersion is most faithfully captured by a Taylor expansion up to second order, with the expansion coefficients in the two principal directions having opposite sign:

$$E = E_v + \alpha p_x^2 - \beta p_y^2 \qquad \alpha, \beta > 0, \tag{1.56}$$

where E_v is the energy at the saddle point, also known as the van Hove energy. Then, we can find the density of states:

$$\rho(E) = \int \frac{\mathrm{d}p_y}{2\pi} \frac{\mathrm{d}p_x}{2\pi} \delta(E - E_{\boldsymbol{p}}) \tag{1.57}$$

where we use the formula

$$\delta(g(x)) = \sum_i \frac{\delta(x - x_i)}{|g'(x_i)|} \tag{1.58}$$

where x_i are the roots of the function $g(x)$. Here we have $g(p_x) = E - E_v + \beta p_y^2 - \alpha p_x^2$, and $g'(p_x) = -2\alpha p_x$. We obtain the roots of $g(p_x)$ as

$$p_x^{\pm} = \pm\sqrt{\frac{(E - E_v) + \beta p_y^2}{\alpha}} \tag{1.59}$$

which gives, defining $\tilde{E} = E - E_v$

$$\rho(E) = \int \frac{\mathrm{d}p_y}{2\pi} \int_{-\infty}^{\infty} \frac{\mathrm{d}p_x}{2\pi} \frac{\delta(p_x - p_x^+) + \delta(p_x - p_x^-)}{2\sqrt{\alpha\beta}\sqrt{\frac{\tilde{E}}{\beta} + p_y^2}} \tag{1.60}$$

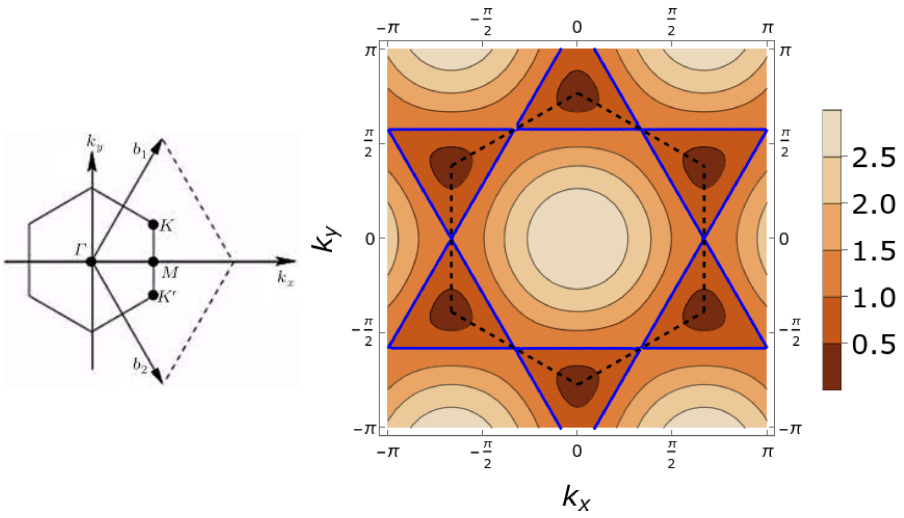

Figure 1.8: Right: Energy contours of graphene showing the brilluoin zone in black dashed lines. The highlighted contour in blue is at the van Hove energy. Left: The corresponding Brillouin zone marking the positions of the high symmetry points. (The left panel has been taken from Ref [82]).

A note has to be made here about the range of p_y, which comes from the condition when p_x has a solution, which is when $E - E_v + \beta p_y^2 > 0$.

$$\text{range of } p_y = \begin{cases} \texttt{all}, & E > E_v \\ p_y^2 > \left|\frac{E-E_v}{\beta}\right|, & E < E_v \end{cases} \tag{1.61}$$

Introducing a cutoff for p_y as Λ, for $E > E_v$,

$$\begin{aligned} \rho(E) &= \frac{2}{\sqrt{\alpha\beta}} \int_0^\infty \frac{\mathrm{d}p_y}{(2\pi)^2} \frac{1}{\sqrt{\frac{\tilde{E}}{\beta} + p_y^2}} \\ &= \frac{1}{2\pi^2\sqrt{\alpha\beta}} \log\left|\frac{2\Lambda\sqrt{\beta}}{\sqrt{E-E_v}}\right| \\ &= \frac{1}{4\pi^2\sqrt{\alpha\beta}} \log\left|\frac{\tilde{\Lambda}}{E-E_v}\right| \end{aligned} \tag{1.62}$$

with $\tilde{\Lambda} = 4\Lambda^2\beta$. The density of states is symmetric about the van Hove energy, and we obtain exactly the same expression for $E < E_v$.

1

1.6. The concept of a higher order van Hove singularity

The hyperbolic geometry of the Fermi surface near the van hove energy and its enhanced density of states can be understood quite intuitively by means of Fig. 1.9a. Much like the SYK model, the enhanced DoS is not from a degeneracy, but the ability to pack energy levels densely close together at low energy. More and more states can be fit into the corner created by the touching Fermi surfaces at the van hove energy, leading to the diverging density of states.

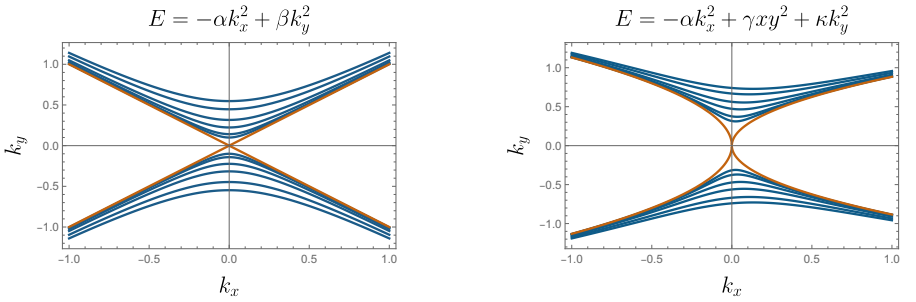

(a) conventional van Hove singularity, Eq. (1.56)

(b) higher order van hove singularity

Figure 1.9: Hyperbolic geometry of the energy contours near a van Hove singularity. In each case, the limiting curve for $E = 0$, which is here the van Hove energy, is shown by an orange line.

Near a conventional logarithmic van hove singularity, the contours of equal energy form hyperbolae in momentum space. This is easily visible in the topology change of the Fermi surface, as it crosses the van hove energy. At exactly the van hove energy, the Fermi surface is made of the asymptotes of the hyperbola, which are two lines meeting at a point. This can be generalized in many ways, the most obvious of which is to have a Fermi surface composed of the intersection of two parabolae with a quartic dispersion(see Fig. 1.9b). This also has a direct effect in the type of singularity in the density of states: in this case being a power law $\rho(E) \sim |E|^{-1/4}$ [83, 84]. These can be neatly classified by a recently developed catastrophe theory formalism [85–87].

The higher order van hove singularity appears in many physical systems, such as the cuprates [88–90], in twisted bilayer graphene and other transition metal dichalcogenide bilayers. The difference however between the cuprates and monolayer graphene as compared to the moire materials is that, while in monolayer graphene and the cuprates the van hove singularity (higher order or otherwise) is far away from the Fermi energy (eV scale) meaning that they are relatively difficult to reach in experiments, whereas they are close to the Fermi energy (meV scale) in the moire materials. Accordingly, they will also have strong effects on measurable properties, as we shall see in the next section.

1.7. Enhanced interactions near van hove points - towards Twisted Bilayer graphene

Graphene is known to not be superconducting at charge neutrality owing to it being a bad metal [91], i.e having a low density of states at the Dirac point. This can be understood in the following cartoon like picture. Assuming, BCS theory of superconductivity holds, the superconducting transition temperature is obtained by solving the linearized gap equation to be

$$T_c = \omega_0 \exp\left\{-\frac{1}{g\rho(E_F)}\right\}, \tag{1.63}$$

where g is a parameter characterizing electron-electron attraction, ω_0 is a UV cutoff (usually taken to be the Debye frequency) and $\rho(E_F)$ is the density of states at the Fermi energy. The vanishing density of states of the Dirac cone implies an negative infinity in the exponential in Eq. (1.63), meaning no superconductivity at any finite temperature.

Thus it came as a surprise when twisted bilayer graphene was observed to be superconducting in some recent landmark experiments [92–95]. But we will argue here that with the considerations of the enhanced DoS coming from the van hove singularity, now quite close to the Fermi level, that it should not be so surprising at all.

This is a part of a general phenomenon in which interactions get enhanced by the hyperbolic geometry in the Fermi surface. A rigorous argument for breakdown of Fermi liquid theory has been addressed in the seminal works of Shankar and Polchinksi in Refs. [96–98] by considering the renormalization effects of interactions upon scaling momenta in the low energy effective theory towards the Fermi surface, but we shall sketch a caricature of it below that captures the essence of the argument without all of its sophisticated machinery.

Consider the particle-hole bubble shown in Fig. 1.10. This diagram - the polarization bubble - arises in many different contexts. In linear response theory, this is the leading diagram corresponding to the charge susceptibility $\chi(q, i\omega_n)$, and is related to the dielectric constant [99]. Another context where it can appear is as a sub-diagram in the leading contribution to decay of quasiparticles in the self energy of an interacting Fermi gas [18], where the full self energy is

$$\Sigma(k,\epsilon_n) = g^2 \int d\boldsymbol{q}\, T \sum_{\omega_n} \Pi(\boldsymbol{q},\omega_n) G_0(\boldsymbol{k}+\boldsymbol{q}, i\epsilon_n + i\omega_n), \tag{1.64}$$

and g is the simplified contact interaction coefficient in Eq. (1.1).

The evaluation of the bubble diagram gives us:

$$\chi_0(q, i\omega_n) = T \sum_{\epsilon_n} \int d\boldsymbol{k}\, G^0(k+q, \epsilon_n + \omega_n) G^0(k, \epsilon_n) \tag{1.65}$$

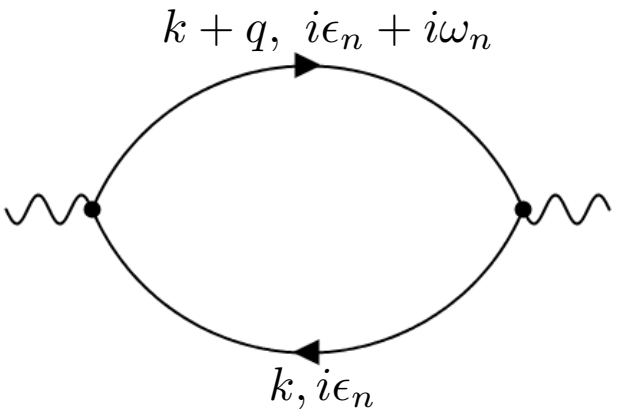

Figure 1.10: Polarization bubble diagram $\Pi(q, i\omega_n)$: This shows up in charge susceptibility, self energy due to fermion-fermion interactions, phonon self energy among others

We can first study the long wavelength static limit $q \to 0, \omega_n = 0$. Then,

$$\begin{aligned}\chi_0(q \to 0, \omega_n = 0) &= T\sum_{\epsilon_n}\int d\boldsymbol{k}\, G^0(k,\epsilon_n)G^0(k,\epsilon_n) \\ &= \int d\boldsymbol{k}\left[T\sum_{\epsilon_n}\left(\frac{1}{i\epsilon_n - E_{\boldsymbol{k}}}\right)^2\right]. \end{aligned} \tag{1.66}$$

This contour integral is trivial to do if one remembers that

$$T\sum_{\epsilon_n}\frac{1}{i\epsilon_n - E_k} = n_F(E_k)\,, \tag{1.67}$$

with $n_F(E)$ being the Fermi-Dirac function. Then we see that

$$\chi_0(q \to 0, \omega_n = 0) = \int d\boldsymbol{k}\frac{\mathrm{d}}{\mathrm{d}E_k}(n_F(E_k)) \tag{1.68}$$

$$= -\int d\boldsymbol{k}\,\delta(E_k - E_F) = -\rho(E_F)\,. \tag{1.69}$$

We have used also that at zero temperature,

$$\frac{\mathrm{d}}{\mathrm{d}E_k}(n_F(E_k)) = -\delta(E_k - E_F)\,. \tag{1.70}$$

It's straightforward to generalize to the case of finite q as well using the partial frac-

tions trick:

$$\begin{aligned}\chi_0(q,\omega_n=0) &= T\sum_{\epsilon_n}\int d\boldsymbol{k}\, G^0(k+q,\epsilon_n)G^0(k,\epsilon_n)\,,\\ &= \int d\boldsymbol{k}\, T\sum_{\epsilon_n}\frac{1}{i\epsilon_n-\epsilon_{k+q}}\cdot\frac{1}{i\epsilon_n-\epsilon_k}\,,\\ &= \int d\boldsymbol{k}\,\frac{1}{\epsilon_{k+q}-\epsilon_k}\,T\sum_{\epsilon_n}\left(\frac{1}{i\epsilon_n-\epsilon_{k+q}}-\frac{1}{i\epsilon_n-\epsilon_k}\right),\\ &= \int\frac{d^dk}{(2\pi)^d}\,\frac{n_F(\epsilon_{k+q})-n_F(\epsilon_k)}{\epsilon_{k+q}-\epsilon_k}\,. \end{aligned} \tag{1.71}$$

For the k^2 dispersions in 1,2 and 3 dimensions, it is also possible to evaluate these integrals exactly in the static response limit (i.e. at $\omega = 0$) [100], and we present just the result below:

1. The susceptibility is a constant in the limit of vanishing wave-vector: i.e. a very slowly spatially varying external field.

$$\chi_0(q\to 0,\omega=0) = -\rho(\epsilon_F)\,. \tag{1.72}$$

2. For finite q, there is a log-singularity at $q = 2k_F$ in the susceptibility, which is a branch cut in the complex plane.

$$\chi_0(q,\omega=0) = -\rho(\epsilon_F)F(\frac{q}{2k_F})\,, \tag{1.73}$$

$$F(x) = \frac{1}{2}+\frac{1-x^2}{4x}\log\left|\frac{1+x}{1-x}\right| \tag{1.74}$$

Thus one can clearly see the vital effect the density of states has on the interaction corrections to the Fermi gas. In a high carrier density metal in three dimensions like bulk copper, $\rho(E_F)$ can be taken to be more or less a constant, and weak interactions can be treated perturbatively to just give small corrections to the non-interacting theory. However, when the Fermi energy is close to a van-Hove singularity, the divergence in the density of states makes the effective interaction strength large, leading to instabilities and the breakdown of quasiparticles and Fermi liquid theory.

We have spelled out the calculation of the charge susceptibility which arises from the particle-hole bubble in Fig. 1.10, but the exact same enhancement effect from the density of states at the Fermi level also shows up in other physical effects, such as in spin-spin correlation functions, or in the particle-particle bubble for the susceptibility towards pairing in the theory of superconductivity [101].

Having understood the crucial role that van Hove points can play in enhancing correlations between electrons, we will argue that both conventional and more exotic

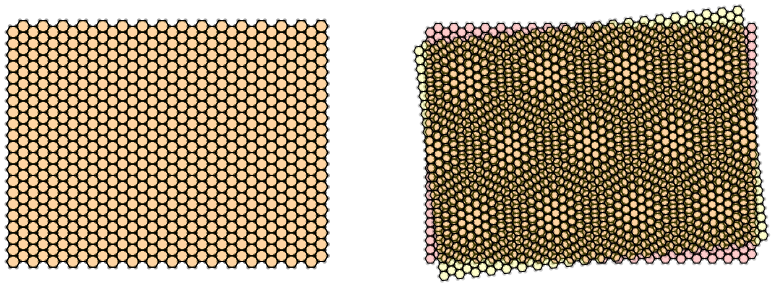

(a) Untwisted AA stacked graphene bilayer

(b) Relative twist of 6.40° with 2892 atoms in the unit cell.

Figure 1.11: Moire pattern in twisted bilayer graphene. Large twist angle shown for ease of illustration. In realistic samples, much smaller twists under 2° are seen, with up to ~ 10000 carbon atoms in the unit cell at the magic angle. (Image generated using the Wolfram demonstrations project [102]).

higher order van Hove singularities play an important role in the twisted bilayer graphene (TBG).

As the name suggests, twisted bilayer graphene is made of two layers of mono layer graphene, at a relative angle to each other. The relative misalignment between the layers originating from the twist leads to the formation of a Moire pattern.

The Moire pattern forms a larger superlattice as is easily visible in Fig. 1.11a. From simple geometric arguments, the lattice constant for the Moire superlattice can be expressed in terms of the lattice constant of graphene for a twist angle θ as [103]

$$\begin{aligned} L_\theta &= \frac{\sqrt{3}a}{2\sin\left(\frac{\theta}{2}\right)} \\ &\approx \frac{\sqrt{3}a}{\theta} \qquad \text{, for small twist angles.} \end{aligned} \tag{1.75}$$

Consequently, the gigantic real space superlattice implies a tiny reciprocal lattice, dubbed the Moire (or mini) Brillouin zone (MBZ). This fact has a far reaching consequence for the low energy band structure of TBG, shown in pictorially in Fig. 1.13.

Since the moire lattice is also hexagonal, it must also have an effective Dirac cone in its spectrum. If we restrict our attention only to the low energy bands, we can look simply at what happens to the Dirac cone at the K and K′ points of each individual monolayer. These form the corners of the MBZ. The smallness of the MBZ

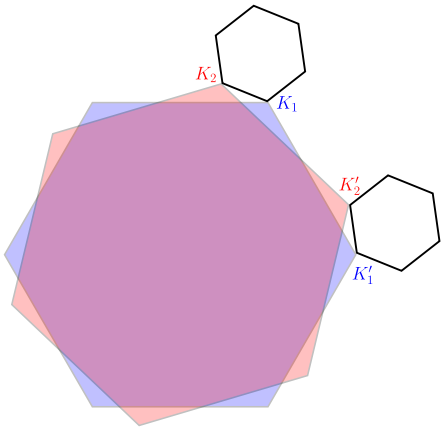

Figure 1.12: Illustration of the formation of the Moire Brillouin zone. Starting from AA stacking, one layer is rotated relative to the other layer by a small angle. It is easy to see from this figure that if $\boldsymbol{k}$ was the wavevector of the K point of the Brillouin zone of monolayer graphene, then the size of the mini Brillouin zone is $k\theta$.

means that there will be significant overlap in the two lowest energy bands, and the hybridization caused by the interlayer hopping will lead to a level repulsion, similar to the formation of the bonding and antibonding orbitals in molecular orbital theory description of the hydrogen molecule. This is shown pictorially in Fig. 1.13.

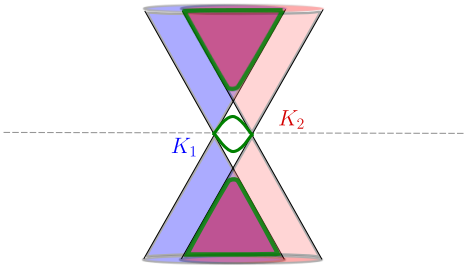

Figure 1.13: Illustration of the formation of the flat bands: When the two Dirac cones from each layer are close together, there's a significant overlap in their wavefunction, and hybridization effects can be large enough to render the bottom band almost completely flat.

This simple effective continuum model was first described by Bistritzer and Macdonald in their seminal work in Ref. [103]. Their key finding was that at some "magic" angle, the bonding orbital thus formed experiences such a degree of energy lowering that the lowest band becomes almost completely flat. For twisted bilayer graphene, this angle is roughly 1.05°. In other words, this is the angle at which the effective Dirac velocity of the cone corresponding to hexagonal lattice of the bilayer system vanishes.

Furthermore, the flat band thus formed for small twist angles is not completely flat, but has features at the scale of meV, including van Hove singularities. Unlike the case of the square lattice or mono layer graphene, which have vHS at high energies in the eV scale, these low energy vHs in TBG are very close to the Fermi level, and will play an important role in the low energy physics of the material. At exactly the magic angle, we even observe a higher order vHS, and the role it plays in the ability of the system to screen the spin of magnetic impurities will be the subject of Chapter 4.

1.8. This thesis

In the introduction, we have explored two very different electronic systems, and uncovered clandestine hyperbolic geometries in each of them.

1.8.1. Chapter 2 - Chaos in the bipartite Sachdev-Ye-Kitaev model

This chapter studies the scrambling dynamics of the b-SYK model by calculation of its Lyapunov exponent, both in the fully conformal limit and at intermediate and weak coupling as the population ratios of the A and B Majoranas are changed. The population imbalance endows the A and B Majoranas with separate conformal dimensions, but the analysis presented determines the model as a whole to have one unique exponent. This is understood in terms of scattering pathways of the A and the B Majoranas mixing with each other and the model always picking the scattering pathway with the fastest rate. Furthermore, although the model saturates the chaos bound presented in the seminal work of Ref. [73] in the conformal limit, it was observed that even the corrections to the Lyapunov exponent at intermediate coupling in the b-SYK model is uninfluenced by perturbations to the conformal dimension of the A and B fermions, which is a surprising result. This chapter has been published in Ref. [104].

1.8.2. Chapter 3 - Wormholes in the Yukawa-Sachdev-Ye-Kitaev model

In this chapter, we study a model of two YSYK dots coupled with a tunneling interaction λ. In the weak tunneling limit, the quantum state of the system is well approximated by the thermo-field double (TFD) state. This makes the system dual to an eternal traversable wormhole, along the lines of Ref. [80, 105]. In the TRS broken non-superconducting state, we indeed find a first order transition of the system from the two black holes phase to a wormhole phase, with a clear signature in the scaling of the boson and fermion Green's functions. Furthermore, we find that the worm-

hole phase survives the competition from superconducting order, which arises upon the restoration of TRS. On the gravitational side, superconductivity is described by scalar hair. Our key finding is that the system in the superconducting state remains a traversable wormhole for the fermionic excitations, but not for the scalar hair. Additionally, since the system on the field theory side represents two coupled superconductors, we investigate the Josephson effect that arises from twisting the phase of the two sides relative to one another. This chapter is still a manuscript under preparation.

1.8.3. Chapter 4 - The Kondo effect in Twisted bilayer graphene

This chapter concerns the fate of dilute magnetic impurities embedded in twisted bilayer graphene. The density of states profile of twisted bilayer graphene has both a dirac cone and a van Hove singularity in it, the location of which moves closer towards the Fermi energy upon changing the twist angle between the layers closer and closer to 1.05°. In a metal with a constant density of states and a large carrier density, the magnetic moment of the impurity gets strongly screened by the conduction electrons in a phenomenon called the Kondo effect for temperatures below a characteristic scale called the Kondo temperature. This is not seen in monolayer graphene owing to the low density of states of the Dirac cone in similar spirit to Eq. 1.63. The chapter first addresses the modeling of the low energy band structure of twisted graphene using the continuum Bistritzer-MacDonald model [103], presents a method to accurately determine the positions and nature of the van Hove singularities close to the Fermi level, and then presents numerical renormalization group results for the impurity entropy and spectral function at finite temperature for this version of the Kondo problem. The key prediction is a revival of the Kondo effect at the lowest energy scales at exactly the magic angle of twisted bilayer graphene. The results of this chapter have been published in Ref. [106] and further studies confirming the prediction using more sophisticated models have appeared from other groups since in Ref. [107].

2

Lyapunov Exponents in the bipartite SYK model

Attribution

This paper has been previously published in Physical review D under the title ***Lyapunov exponents in a Sachdev-Ye-Kitaev-type model with population imbalance in the conformal limit and beyond***, together with Mikael Fremling, Stephan Plugge and Lars Fritz [104].

Abstract

The Sachdev-Ye-Kitaev (SYK) model shows chaotic behavior with a maximal Lyapunov exponent. In this paper, we investigate the four-point function of a SYK-type model numerically, which gives us access to its Lyapunov exponent. The model consists of two sets of Majorana fermions, called A and B, and the interactions are restricted to being exclusively pairwise between the two sets, not within the sets. We find that the Lyapunov exponent is still maximal at strong coupling. Furthermore, we show that even though the conformal dimensions of the A and B fermions change with the population ratio, the Lyapunov exponent remains constant, not just in the conformal limit where it is maximal, but also in the intermediate and weak coupling regimes.

2.1. Introduction

Over the last decade, the Sachdev-Ye-Kitaev (SYK) model has been established as a paradigmatic model accounting for a variety of phenomena ranging from aspects of the physics of black holes to non-Fermi liquids [108–112]. There exist two main variants of this model in the literature: one that is formulated in terms of N 'complex' Dirac fermions, and another one written in terms of N 'real' Majorana fermions. In both cases, the fermions interact via random four-body terms. Irrespective of the formulation, one of the main features of the model is that it exhibits emergent conformal symmetry in the infrared in the strong-coupling and large-N limit. The scaling dimension of the fermion correlation function is given by $\Delta = \frac{1}{4}$ [19, 113], indicative of strong interactions (for comparison, a free fermion has scaling dimension 1/2).

There has been a variety of proposals for the creation of SYK-like models in laboratory setups. They range from mesoscopic systems hosting Majorana modes [114, 115], or Dirac fermions in graphene flakes [46, 116], to ultracold atomic systems [117, 118]. A comprehensive review of such possible setups can be found in Refs. [108, 110] and references therein.

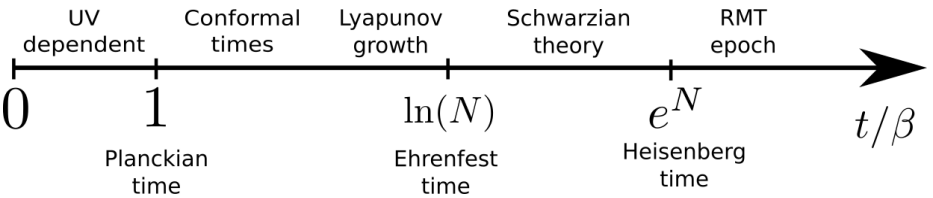

Figure 2.1: The SYK model exhibits multiple characteristic timescales, and with that associated regimes of dynamics. Crucial quantities in distinguishing the different limits are the number of fermions N and coupling strength βJ. This paper studies the region characterized by Lyapunov growth.

The SYK model involves three important time scales, as shown in Fig. 2.1 (henceforth, we measure time t in units of β and set $\hbar = k_b = 1$). They are called the Planckian time [8, 119–121], t_P, the Ehrenfest time [122–126], t_E, and the Heisenberg time t_H. The shortest time scale, t_P, is set by the condition $t_P/\beta \approx 1$. For times shorter than t_P, we expect non-universal physics determined by processes at the cutoff scale. For $t_P < t < t_E$, the dynamics is governed by the conformal mean-field theory. The chaotic behavior associated with Lyapunov growth [73, 76] in this regime is due to leading irrelevant operators of order $1/N$ beyond mean-field. The Ehrenfest time is given as $t_E/\beta \approx \ln N$, where N is the number of fermions. The dynamical behavior for $t_E < t < t_H$ ceases to be described by mean-field theory plus corrections and the associated description is in terms of the Schwarzian theory of black holes. Eventually, there is the Heisenberg time, $t_H/\beta \approx e^N$. For times longer than t_H, the dynamics is described by random matrix theory.

In this paper we study a related model, introduced in Ref. [53, 57], which emerges as

a Majorana variant of the SYK model. It is called the bipartite SYK (or b-SYK) model and, as explained in Sec. 2.2, can be seen as a restricted version of the standard SYK model. Incidentally, Majorana or complex fermion versions of similar models also appear as a natural way to incorporate internal symmetries in SYK models [127–129], or to couple two or more SYK models [130]. We are interested in times shorter than the Ehrenfest time t_E, and mostly focus on the chaotic behavior. Furthermore, we are interested in studying the growth of the four-point function not just in the full conformal limit at strong coupling, but also at intermediate and weak couplings, as these might be relevant for experimentally achievable values of coupling and temperature, as the b-SYK model has been shown to be realizable in a laboratory by straining a real material in Ref.[53].

We show that the Lyapunov exponent is maximal in the conformal limit, just as for the SYK model [19, 73, 76]. The behavior of the chaos exponent for a general number of majorana fermions in the A and B subsets of the b-SYK at finite coupling is unanswered in the existing literature and is the subject of the present study. We use numerical methods to solve the Schwinger-Dyson and Bethe-Salpeter equations that are needed to extract the Green functions and Lyapunov exponents, respectively. We find that the b-SYK model ratio of A and B majoranas does not influence the Lyapunov exponent for all values of coupling.

The present paper is organized as follows: In Sec. 2.2, we introduce the b-SYK model and comment on how it is related to more common variants of SYK models. In Sec. 2.2.2 we discuss the two-point functions in and away from the conformal limit. In Sec. 2.3, we compute the four-point function and introduce the equations that allow us to extract the Lyapunov exponents. In Sec. 2.4, we numerically find the Lyapunov exponents and show how they depend on the population balance between A and B Majorana fermions.

2.2. Model and methods

2.2.1. The bipartite SYK model

The bipartite SYK (b-SYK) model consists of two sets of Majorana fermions, labelled A and B, with random interactions between pairs of A and pairs of B fermions. Interactions between only A or only B fermions are absent, and the fermion parity in both the A and B subsets is conserved. The Hamiltonian reads

$$H = \frac{1}{4} \sum_{ij,\alpha\beta} J_{ij\alpha\beta} \gamma_i^A \gamma_j^A \gamma_\alpha^B \gamma_\beta^B \,. \tag{2.1}$$

To distinguish the two sets of fermions we use latin indices i, j for the A-flavor Majorana fermions (γ_i^A), and greek indices α, β for B-flavor Majorana fermions (γ_α^B).

We allow for N_A Majorana fermions of the A-type and N_B of the B-type. The ratio $\kappa = N_A/N_B$ accounts for the relative size of the two sets. The couplings $J_{ij\alpha\beta}$ are random and only act between sets, not within each set. Concerning the normalization of the interaction strength, we follow the convention of Gross and Rosenhaus [131] and choose the variance of the coupling constant to be [1]

$$\langle J_{ij\alpha\beta} J_{i'j'\alpha'\beta'} \rangle = \frac{J^2(N_A+N_B)}{N_A^2 N_B^2} \delta_{i,i'}\delta_{j,j'}\delta_{\alpha,\alpha'}\delta_{\beta,\beta'}.$$

In this work, we will define N as the geometric mean of N_A and N_B, $N = \sqrt{N_A N_B}$. We can then rewrite $\frac{N_A+N_B}{N_A^2 N_B^2} = (\sqrt{\kappa} + \frac{1}{\sqrt{\kappa}})/N^3$, which makes the symmetry between κ and $1/\kappa$ apparent. For clarity, this convention differs from the one used in Refs. [53, 57], where $\langle J_{ij\alpha\beta} J_{i'j'\alpha'\beta'} \rangle = \frac{J^2}{2\sqrt{N_A N_B}^3} \delta_{i,i'}\delta_{i,i'}\delta_{j,j'}\delta_{\alpha,\alpha'}\delta_{\beta,\beta'}$.

The model has a well-defined large-N conformal limit upon taking $N_A, N_B \to \infty$, keeping the ratio $\kappa = \frac{N_A}{N_B}$ fixed. Rather than a single scaling dimension as in the standard SYK model, the two sets of Majorana fermions, A and B, have distinct scaling dimensions, Δ_A and Δ_B. These depend on the parameter κ, cf. Ref. [57], as

$$\kappa = \frac{2\Delta_A}{1-2\Delta_A}\left(\frac{1}{\tan(\pi\Delta_A)}\right)^2. \tag{2.2}$$

For $\kappa = 1$ we find $\Delta_A = \Delta_B = 1/4$, just like in the standard SYK model, although the model is still different since not all Majorana fermions interact with each other. For other values of κ, both scaling dimensions interpolate between 0 and 1/2 while always fulfilling $\Delta_A + \Delta_B = 1/2$. Tunable scaling dimensions have also been found in other variants of the SYK model e.g Ref. [58, 59, 128, 132].

2.2.2. Schwinger-Dyson equations

For the later numerical analysis to follow, one main input is required, the Green functions. Hence we recapitulate the crucial steps in solving the model in the large-N limit via the associated Schwinger-Dyson equations. For more details on the procedure in the present context see e.g. Ref. [57]. In this part of the paper, the focus is more on finding a reliable numerical implementation of the Green function that allows to access the conformal limit. The crucial step is to consider the mean-field or large-N limit. Compared to the conventional SYK model, we have to modify the limit slightly. We take $N_A, N_B \to \infty$ while keeping $\kappa = N_a/N_B$ fixed. As in the conventional case, there is one order $O(1)$ diagram per species of fermions, the so-called 'melon' diagrams. These are shown in Fig. 2.2. The diagrams contain the coupling J^2 to all orders and exhibit an emergent conformal symmetry in the infrared, as explained below.

[1] note that this is the $q = 2, f = 2$ limit of Ref. [131]

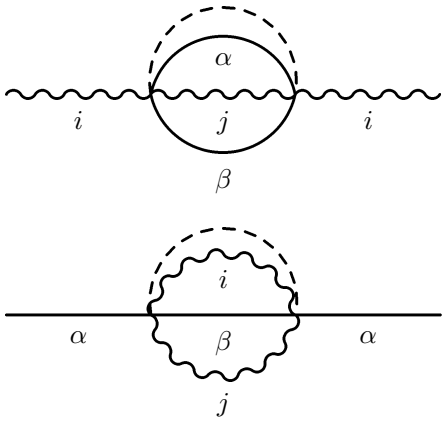

Figure 2.2: The diagrams that contribute to the self energies of A (top) and B (bottom) Majoranas in the large-N limit. Wiggly (solid) lines denote A (B) Majorana propagators, and the dotted line indicates a quenched disorder average $\sim J^2$.

Imaginary time formalism

The discussion of equilibrium properties of the Schwinger-Dyson (SD) equations is easiest carried out in the finite-temperature imaginary time formalism. The inverse temperature is denoted as $\beta = 1/T$ ($\hbar = k_B = 1$). For the two species, the SD equations read

$$G^{A/B}(i\omega_n) = \frac{1}{-i\omega_n - \Sigma^{A/B}(i\omega_n)}, \tag{2.3}$$

where the respective self energies are given by

$$\Sigma_A(\tau) = \frac{J^2}{2}(1+\frac{1}{\kappa})\, G^A(\tau)\left(G^B(\tau)\right)^2, \tag{2.4a}$$

$$\Sigma_B(\tau) = \frac{J^2}{2}(1+\kappa)\, G^B(\tau)\left(G^A(\tau)\right)^2 . \tag{2.4b}$$

Here $\omega_n = (2n+1)\pi T$ for integer n are the fermionic Matsubara frequencies, whereas τ denotes imaginary time. The Fourier transform between Matsubara frequencies and imaginary time is defined according to

$$G(i\omega_n) = \int_0^\beta e^{i\omega_n\tau} G(\tau)\, d\tau\,, \tag{2.5a}$$

$$G(\tau) = \frac{1}{\beta}\sum_{\omega_n} e^{-i\omega_n\tau} G(i\omega_n)\,. \tag{2.5b}$$

One can show analytically that the finite temperature imaginary time Green functions are given by [57]

$$\begin{aligned} G^A(\tau) &= a\,\mathrm{sgn}(\tau)\left(\frac{\pi}{\beta\sin\left(\frac{\pi\tau}{\beta}\right)}\right)^{2\Delta_A}, \\ G^B(\tau) &= b\,\mathrm{sgn}(\tau)\left(\frac{\pi}{\beta\sin\left(\frac{\pi\tau}{\beta}\right)}\right)^{2\Delta_B}, \end{aligned} \tag{2.6}$$

where for a given κ, the scaling dimensions Δ_A and Δ_B are related according to Eq. (2.2).

As far as the overall constants a and b are concerned, it is found that only the product ab is uniquely determined, and not the numbers a and b themselves. When we assume that the self energy dominates over the free propagator, we can use the conformal ansatz in equations Eq. (2.4) and (2.3) for each of the A and B flavors respectively. Naively, we would expect that the two equations are sufficient to constrain the two unknowns a and b respectively, but it turns out the two equations are identical, and only the product is constrained. The result is

$$\frac{1}{a^2b^2} = \frac{J^2}{2}\left(1+\frac{1}{\kappa}\right)2\pi\frac{\cot(\pi\Delta_A)}{1-2\Delta_A} \tag{2.7}$$

$$= \frac{J^2}{2}(1+\kappa)\,2\pi\frac{\cot(\pi\Delta_B)}{1-2\Delta_B}. \tag{2.8}$$

However, in the real system, at short times, the conformal ansatz is no longer valid, and the free propagator wins over, and $G^{A/B}(\tau)$ should go as $\frac{1}{2}\mathrm{sgn}(\tau)$. This is sufficient to uniquely constrain the short time dynamics of the model.

Numerically, we solve the Schwinger-Dyson equations in a self-consistent manner by repeated evaluation of the Green functions and self-energies paired with an iteration on an imaginary time grid running from 0 to β. Eqs. (2.5a), (2.5b) and similarly for the self-energies here are recast in the form of discrete Fourier transforms, for which there are efficient numerical algorithms such as Fast Fourier transform. To achieve convergence, we use a weighted update of the Green functions according to $G^{new} = \frac{x}{-i\omega_n-\Sigma} + (1-x)G^{old}$ with a small mixing parameter x; here $\Sigma(i\omega_n)$ denotes the associated self-energy calculated from G^{old} of the previous iteration.

In Fig. 2.3 we show the Majorana Green functions $G^{A/B}(\tau)$ for $\beta J = 10$ and for a variety of values of κ. By fitting the numerically obtained $G^{A/B}$ to Eq. (2.6) one can see that the scaling dimensions indeed match the conformal results. Overall, we find excellent agreement in the region $0 \ll \tau \ll \beta$.

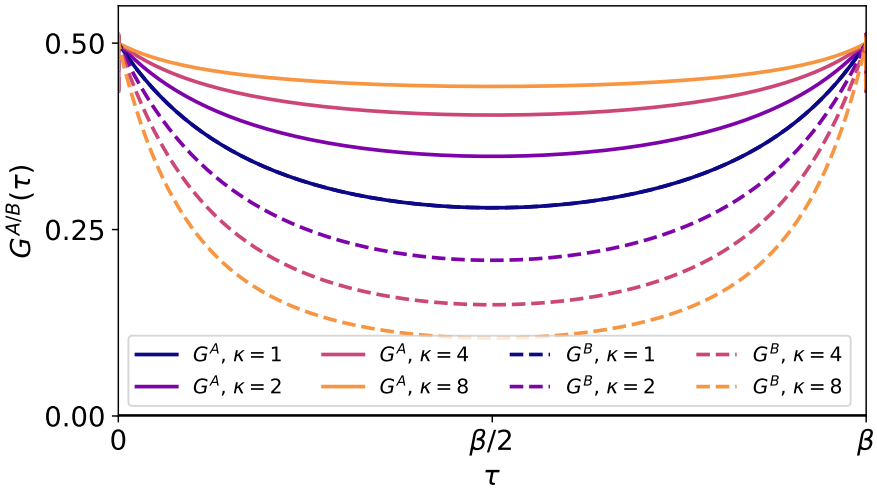

Figure 2.3: Finite temperature Majorana Green functions $G^{A/B}(\tau)$ for $\beta J = 10$ and several values of κ. Taking $\kappa \to 1/\kappa$ exchanges the A and B species, hence we plot only $\kappa \geq 1$.

2.2.3. Real time formalism

The main goal of this paper is to numerically study the out-of-time-ordered correlator (OTOC) in the b-SYK model. To compute it, we need the real time retarded Green function as input. We first note the Dyson equation for the retarded propagator [23, 127, 129, 133]

$$\left(G^R(\omega + i\delta)\right)^{-1} = \omega + i\delta - \Sigma^R(\omega + i\delta). \tag{2.9}$$

We drop the A/B labels, unless explicitly required. The spectral decomposition for the Green functions reads:

$$G(z) = \int_{-\infty}^{\infty} \frac{d\Omega}{\pi} \frac{\rho(\Omega)}{z - \Omega}, \tag{2.10a}$$

$$\rho(\omega) = -\operatorname{Im}\left\{G^R(\omega + i\delta)\right\}. \tag{2.10b}$$

Since the self energies are well defined in imaginary time according to Eq. (2.4), we can use Eqs. (2.5a), (2.5b) and (2.10) to express $\Sigma(i\omega_n)$ in terms of the spectral function. The analytical continuation is then done by replacing $i\omega_n \to \omega + i\delta$, resulting in

$$\Sigma_B^R(\omega + i\delta) = \frac{J^2}{2}(1+\kappa) \int\int\int \frac{\mathrm{d}\omega_1}{\pi} \frac{\mathrm{d}\omega_2}{\pi} \frac{\mathrm{d}\omega_3}{\pi} \rho_A(\omega_1)\rho_A(\omega_2)\rho_B(\omega_3) \frac{[n(\omega_1)n(\omega_2)n(\omega_3) + n(-\omega_1)n(-\omega_2)n(-\omega_3)]}{\omega + i\delta - \omega_1 - \omega_2 - \omega_3}, \tag{2.11}$$

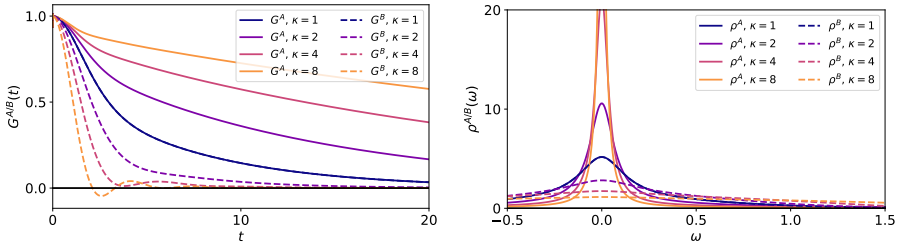

Figure 2.4: *Left panel*: the retarded Green functions $G_R^{A/B}(t)$ for $\beta J = 10$. The characteristic decay timescale is set by the conformal dimension $\Delta_{A,B}$.
Right panel: the corresponding spectral functions, showing a strong dependence on κ.

where $n(\omega)$ is the Fermi-Dirac distribution function. The expression for Σ_A is obtained by changing $A \leftrightarrow B$, and $\kappa \leftrightarrow 1/\kappa$. In principle, the Schwinger-Dyson equations can be solved iteratively for $G^R_{A/B}(\omega)$ and $\rho^{A/B}(\omega)$. However, nested numerical integration is both highly inefficient in its usage of resources and numerically unstable. Instead, it is beneficial to rewrite it using the following decomposition which allows an implementation using only the discrete Fourier transform, cf. Refs. [129, 134]. We can express the self energies as

$$\Sigma^R_A(\omega + i\delta) = -i\frac{J^2}{2}(1+\frac{1}{\kappa})\int_0^\infty dt\, e^{i(\omega+i\delta)t}\left[n^+_A(t)n^+_B(t)n^+_B(t) + n^-_A(t)n^-_B(t)n^-_B(t)\right] \tag{2.12}$$

$$\Sigma^R_B(\omega + i\delta) = -i\frac{J^2}{2}(1+\kappa)\int_0^\infty dt\, e^{i(\omega+i\delta)t}\left[n^+_B(t)n^+_A(t)n^+_A(t) + n^-_B(t)n^-_A(t)n^-_A(t)\right], \tag{2.13}$$

where the function $n^\pm_{A/B}(t)$ is defined through

$$n^\pm_{A/B}(t) = \int_{-\infty}^\infty \frac{d\omega_1}{\pi} e^{-i\omega_1 t}\rho_{A/B}(\omega_1)n(\pm\omega_1)\,. \tag{2.14}$$

The retarded Green function and the corresponding spectral functions obtained from the real-time/frequency iteration of the above SD equations are shown in Figure 2.4.

2.3. The four-point function

We now turn our attention to the four-point correlators of the b-SYK model, and in particular to the out-of-time-ordered correlators (OTOCs). Before we have a look into OTOCs themselves, we first discuss conventional four-point functions. In imaginary

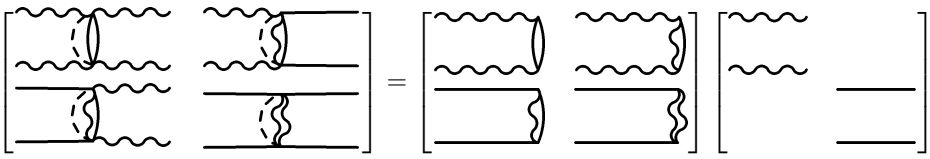

Figure 2.5: Diagrammatic representation of the matrix-kernel equation (2.16) at first order. Repeated application of the kernel K generates all terms in $\mathscr{F}$

time, a general four-point function of Majoranas has the form [131]

$$\mathscr{F}(\tau_1,\tau_2,\tau_3,\tau_4) = \frac{1}{N^2}\sum_{ijkl}\left\langle \gamma_i^{f_1}(\tau_1)\gamma_j^{f_2}(\tau_2),\gamma_k^{f_3}(\tau_3)\gamma_l^{f_4}(\tau_4)\right\rangle. \tag{2.15}$$

The disorder averaging and the large-N limit taken together restrict the contributions to the four-point functions to stem from what are known as ladder diagrams. These can be categorized into four channels, depending on the flavors of the incoming and outgoing pairs of fermion propagators: AA-AA, AA-BB, BB-AA, and BB-BB. A diagram with $n+1$ rungs can be obtained from a diagram with n rungs by convolution with a kernel [76]. In the vicinity of the Ehrenfest time t_E, this can be cast as a self-consistent Bethe-Salpeter equation according to

$$\mathscr{F}_{\alpha\beta}(\tau_1,\tau_2,\tau_3,\tau_4) = \int \mathrm{d}\tau\mathrm{d}\tau' K_{\alpha\gamma}(\tau_1,\tau_2,\tau,\tau')\mathscr{F}_{\gamma\beta}(\tau,\tau',\tau_3,\tau_4) \tag{2.16}$$

where γ is summed over, and the Kernel matrix is given as (in imaginary time and a regularized version in real time respectively)

$$K_{\alpha\gamma}(\tau_1\cdots\tau_4) = -J^2\begin{pmatrix} \frac{1}{2}(1+\frac{1}{\kappa})\,G^A(\tau_{13})G^A(\tau_{24})\left(G^B(\tau_{34})\right)^2 & (1+\frac{1}{\kappa})\,G^A(\tau_{13})G^A(\tau_{24})\left(G^A(\tau_{34})G^B(\tau_{34})\right) \\ (1+\kappa)\,G^B(\tau_{13})G^B(\tau_{24})\left(G^A(\tau_{34})G^B(\tau_{34})\right) & \frac{1}{2}(1+\kappa)\,G^B(\tau_{13})G^B(\tau_{24})\left(G^A(\tau_{34})\right)^2 \end{pmatrix} \tag{2.17}$$

$$K^R_{\alpha\gamma}(t_1\cdots t_4) = J^2\begin{pmatrix} \frac{1}{2}(1+\frac{1}{\kappa})\,G^A_R(t_{13})G^A_R(t_{24})\left(G^B_W(t_{34})\right)^2 & (1+\frac{1}{\kappa})\,G^A_R(t_{13})G^A_R(t_{24})\left(G^A_W(t_{34})G^B_W(t_{34})\right) \\ (1+\kappa)\,G^B_R(t_{13})G^B_R(t_{24})\left(G^A_W(\tau_{34})G^B_W(t_{34})\right) & \frac{1}{2}(1+\kappa)\,G^B_R(t_{13})G^B_R(t_{24})\left(G^A_W(t_{34})\right)^2 \end{pmatrix} \tag{2.18}$$

The indices α,β,γ refer to the flavors of the Majorana propagators on the external legs. For example, F_{00} refers to the AA-AA scattering and F_{10} refers to BB-AA scattering. A diagrammatic representation of the matrix-kernel equation (2.16) is shown in Fig. 2.5.

Quantum chaos is characterized by the Lyapunov exponent. Instead of looking at the real time version of Eq. (2.15), we consider a regularized version according to

$$F_{ab}(t_1,t_2) = \frac{1}{N^2}\sum_{a,b}\overline{\mathrm{Tr}\left\{\sqrt{\rho}\left[\gamma_a(t_1),\gamma_b(0)\right]\sqrt{\rho}\left[\gamma_a(t_2),\gamma_b(0)\right]\right\}}. \tag{2.19}$$

This regularized OTOC has the thermal density matrix ρ of the thermal average split evenly between pairs of Majorana operators, and brackets $[\cdot,\cdot]$ denote commutators.

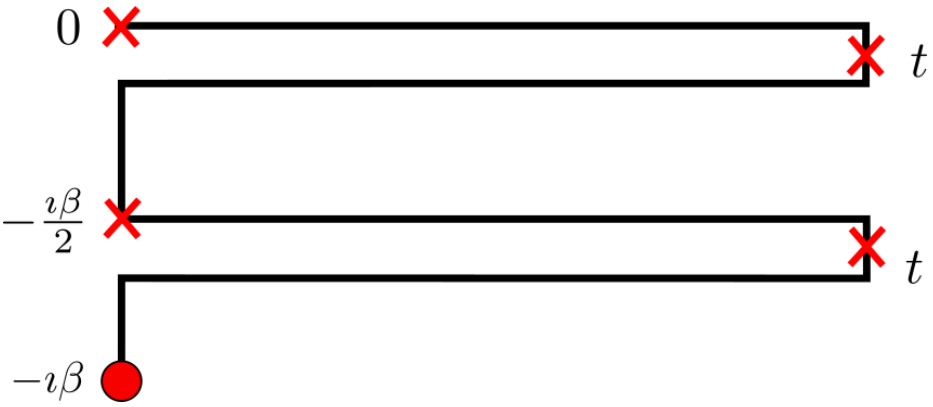

Figure 2.6: Schwinger-Keldysh contour with two temporal folds (excursions to time t) and Majorana operator insertions (red crosses) that represents the regularized OTOC in Eq. (2.19).

In diagrammatic language this means that the four point function is evaluated on a double-fold Schwinger-Keldysh contour with insertions of the Majorana operators as shown in Fig. 2.6.

This is a regularization not of the UV, but of the IR. Details on which of the many possible choices of regularization and Schwinger-Keldysh contour one might pick can be found in Ref. [79]. The key point is that for massless theories, which the SYK universality class belongs to, all different regularizations give the same exponential growth, even though the values of the actual OTOCs may differ. For the choice in Eq. (2.19), the four point function in question will be generated by ladder diagrams with retarded or advanced Green functions on the rails, and so-called Wightman functions $G^W(t) = G(\frac{\beta}{2} + it)$ on the rungs. Formally, the latter are obtained by an analytic continuation of the imaginary time Green function noted in Sec. 2.2.2. This analytic continuation can be be performed with the use of the spectral decomposition, also known as a Hilbert transform. In total, one obtains the result

$$G^W(\omega) = \frac{\rho(\omega)}{2\cosh\frac{\beta\omega}{2}}. \tag{2.20}$$

The late time exponential growth of the OTOC [73] can then be fit to the Lyapunov ansatz

$$\mathscr{F}_{\alpha\beta}(t_1, t_2) = e^{\lambda_{\alpha\beta}\frac{(t_1+t_2)}{2}} f_{\alpha\beta}(t_{12})\,. \tag{2.21}$$

As opposed to the standard SYK model, each of the four different scattering channels might ostensibly have its own Lyapunov exponent. It turns out that this is not the case. A detailed technical explanation involving the consistency of the Lyapunov ansatz with a single exponent λ is presented in Appendix 2.5.1.

A simple qualitative argument for a single Lyapunov exponent is that the scattering

channels all feed back into each other. The AA-AA scattering amplitude also passes through the AA-BB channel and then back into the BB-AA channel. This imposes a sense of self-consistency between the scattering channels, which in turn forces them to have the same late time Lyapunov growth.

2.3.1. Conformal limit

Taking the ansatz that all four Lyapunov exponents $\lambda_{\alpha\beta}$ are the same, *i.e.* $\lambda_{\alpha\beta} = \lambda$ allows us to make an ansatz for the growth equation. First, we will notice that the equations for f_{00} and f_{10} decouple, and we get the same equations for the other pair f_{01} and f_{11}. In the conformal limit, following [19] we can use the conformal mapping to obtain the retarded and Wightman Green functions from Eqs. (2.6) to get

$$G_R^A(t) = 2a\cos(\pi\Delta_A)\left(\frac{\pi}{\beta\sinh\frac{\pi t}{\beta}}\right)^{2\Delta_A} \tag{2.22a}$$

$$G_W^A(t) = a\left(\frac{\pi}{\beta\cosh\frac{\pi t}{\beta}}\right)^{2\Delta_A}, \tag{2.22b}$$

and likewise for the $B-$ fermions. The growth ansatz can also be made in analogy with the regular SYK case:

$$\begin{pmatrix} f_{00}(t_{12}) \\ f_{10}(t_{12}) \end{pmatrix} = \begin{pmatrix} a\mathscr{C}_a\left(\frac{\pi}{\beta\cosh(t_{12}\frac{\pi}{\beta})}\right)^{2\Delta_a+h} \\ b\mathscr{C}_b\left(\frac{\pi}{\beta\cosh\left(t_{12}\frac{\pi}{\beta}\right)}\right)^{2\Delta_b+h} \end{pmatrix} e^{h(t_1+t_2)\frac{\pi}{\beta}} \tag{2.23}$$

It can be noted that Eq. (2.23) is a way of rewriting Eq. (2.21) in a way that is convenient for the conformal limit calculation. $\mathscr{C}_a$ and $\mathscr{C}_b$ are hitherto undetermined constants. The equations one needs to solve are then (the factors of $\frac{\pi}{\beta}$ have been chosen appropriately so that they scale away)

$$e^{h(t_1+t_2)}f_{00}(t_{12}) = \frac{J^2}{2}(1+\frac{1}{\kappa})\int dt_3 dt_4\Big[G_R^A(t_{13})G_R^A(t_{24})G_W^B(t_{34})^2 f_{00}(t_{34}) + 2G_R^A(t_{13})G_R^A(t_{24})G_W^B(t_{34})G_W^A(t_{34})f_{10}(t_{34})\Big]e^{h(t_3+t_4)} \tag{2.24a}$$

$$e^{h(t_1+t_2)}f_{10}(t_{12}) = \frac{J^2}{2}(1+\kappa)\int dt_3 dt_4\Big[G_R^B(t_{13})G_R^B(t_{24})G_W^A(t_{34})G_W^B(t_{34})f_{00}(t_{34}) + 2G_R^B(t_{13})G_R^B(t_{24})G_W^A(t_{34})^2 f_{10}(t_{34})\Big]e^{h(t_3+t_4)} \tag{2.24b}$$

The way to solve these equations is to first represent the t_{34} part as an inverse fourier transform, which factorizes the integral into a function that depends only on t_3 and

another function that depends only on t_4, which can be separately integrated. One can express the fourier transforms for powers of hyperbolic sines and cosines as analytic continuations of the Euler Beta function

$$\int_{-\infty}^{\infty} dt\, e^{i\omega t} \frac{1}{(\cosh t)^{\alpha}} = 2^{\alpha-1}\mathrm{B}\left(\frac{\alpha - i\omega}{2}, \frac{\alpha + i\omega}{2}\right), \tag{2.25a}$$

$$\int_{-\infty}^{\infty} dt\, e^{i\omega t} \frac{\theta(t)}{(\sinh t)^{\alpha}} = 2^{\alpha-1}\mathrm{B}\left(\frac{\alpha - i\omega}{2}, 1-\alpha\right). \tag{2.25b}$$

The result then is that

$$\mathscr{C}_a = \mathscr{M}\,(\mathscr{C}_a + 2\mathscr{C}_b) \tag{2.26a}$$

$$\mathscr{C}_b = \mathscr{M}'\,(2\mathscr{C}_a + \mathscr{C}_b)\,, \tag{2.26b}$$

where

$$\mathscr{M} = \frac{(1-2\Delta_A)\sin(2\pi\Delta_A)}{\pi} \frac{(\Gamma(1-2\Delta_A))^2\Gamma(2\Delta_A+h)}{\Gamma(2-2\Delta_A+h)} \tag{2.27}$$

$$\mathscr{M}' = \frac{(1-2\Delta_B)\sin(2\pi\Delta_B)}{\pi} \frac{(\Gamma(1-2\Delta_B))^2\Gamma(2\Delta_B+h)}{\Gamma(2-2\Delta_B+h)} \tag{2.28}$$

The equations Eqs. (2.26) only have a trivial solution $\mathscr{C}_A = \mathscr{C}_B = 0$ if either of the scaling dimensions are 0 or $\frac{1}{2}$, i.e, the $\kappa = 0$ and $\kappa \to \infty$ models are not chaotic in the strictly conformal limit.

For any other intermediate κ, even infinitesimally small, Eqs. (2.26) permit a solution if

$$\det\begin{bmatrix} \mathscr{M}-1 & 2\mathscr{M} \\ 2\mathscr{M}' & \mathscr{M}'-1 \end{bmatrix} = 0. \tag{2.29}$$

We have solved this equation for h and the solution found is always $h = 1$ for any value of κ. This means that for the b-SYK model, it is always possible to increase the coupling and lower the temperature sufficiently that the system always has a maximal Lyapunov exponent $\lambda = \frac{2\pi}{\beta}$.

For realistic couplings and not too low temperatures, one needs to observe the behavior of the Lyapunov exponent including non-conformal corrections to the Green function by perturbatively including the $i\omega$ term in the Dyson equation. If the correction to the Kernel is δK_R, and if we compute all the eigenvalues in the conformal limit and call them $k(h)$, the we can Taylor-expand $k(h)$ about $h = 1$. The point is now that $h = 1$ gives eigenvalue $k(h) = 1$, so we say that

$$k(1+\delta h) = 1 + k'(1)\,\delta h \tag{2.30}$$

Thus in order to keep the kernel having eigenvalue 1, the correction

$$\begin{aligned} \langle \delta K_R \rangle &= \delta h k'(1) \\ \implies \delta h &= \frac{\langle \delta K_R \rangle}{k'(1)} \end{aligned} \tag{2.31}$$

is the first non-conformal correction to the lyapunov exponent.

2.3.2. Numerical analysis for weak and intermediate coupling

Rather than take this complicated approach, the weak and intermediate coupling limits can be analysed numerically. We can bring the kernel equation into the concise form

$$f_{\alpha\beta}(\omega) = \left| G_R^{\alpha}(\omega + i\frac{\lambda}{2}) \right|^2 \left(\tilde{K}_{\alpha 0} * f_{0\beta} + \tilde{K}_{\alpha 1} * f_{1\beta} \right) , \tag{2.32}$$

where additionally a Fourier transform was performed. The ansatz function $f_{\alpha\beta}(\omega')$ is analyzed in frequency space, see below. We also denote the shifted frequency $\tilde{\omega} = \omega + i\frac{\lambda}{2}$ that enters in the retarded Green function. The latter is obtained from the regular retarded Green function $G_R(\omega + i\delta)$ that is calculated in Sec. 2.2.3 by use of the Fourier shift theorem. The symbol $\star$ in Eq. (2.32) indicates a convolution with the ansatz function $f_{\gamma\beta}(\omega)$. The part of the kernel elements $\tilde{K}_{\alpha\gamma}(\omega)$ that contains the Wightman Green functions is given by

$$\tilde{K}_{\alpha\beta}(\omega) = J^2 \begin{pmatrix} \frac{1}{2}(1+\frac{1}{\kappa})\,\mathfrak{F}\left[(G_W^B(t))^2\right] & (1+\frac{1}{\kappa})\,\mathfrak{F}\left[(G_W^B(t)\,G_W^A(t))\right] \\ (1+\kappa)\,\mathfrak{F}\left[(G_W^B(t)\,G_W^A(t))\right] & \frac{1}{2}(1+\kappa)\,\mathfrak{F}\left[(G_W^A(t))^2\right] \end{pmatrix} \tag{2.33}$$

where $\mathfrak{F}[\cdot]$ represents the Fourier transformation.

Finally, note that Eq. (2.32) can be thought of as an eigenvalue problem for the ansatz $f_{\alpha\beta}(\omega)$ in frequency space ω with a block structure α, β due to the different kernel matrix blocks according to

$$\begin{bmatrix} f_{00}(\omega) \\ f_{10}(\omega) \\ f_{01}(\omega) \\ f_{11}(\omega) \end{bmatrix} = \begin{bmatrix} |G_R^A(\tilde{\omega})|^2 \tilde{K}_{00}(\omega-\omega') & |G_R^A(\tilde{\omega})|^2 \tilde{K}_{01}(\omega-\omega') & 0 & 0 \\ |G_R^B(\tilde{\omega})|^2 \tilde{K}_{10}(\omega-\omega') & |G_R^B(\tilde{\omega})|^2 \tilde{K}_{11}(\omega-\omega') & 0 & 0 \\ 0 & 0 & |G_R^A(\tilde{\omega})|^2 \tilde{K}_{00}(\omega-\omega') & |G_R^A(\tilde{\omega})|^2 \tilde{K}_{01}(\omega-\omega') \\ 0 & 0 & |G_R^B(\tilde{\omega})|^2 \tilde{K}_{10}(\omega-\omega') & |G_R^B(\tilde{\omega})|^2 \tilde{K}_{11}(\omega-\omega') \end{bmatrix} \begin{bmatrix} f_{00}(\omega') \\ f_{10}(\omega') \\ f_{01}(\omega') \\ f_{11}(\omega') \end{bmatrix} . \tag{2.34}$$

On the finite frequency grid, the convolution operations naturally translate to matrix multiplications. For a solution of $f_{\alpha\beta}$ to exist, the matrix operator needs to have 1 as its largest eigenvalue [19, 76, 122]. This is equivalent to saying that Eq. (2.21) is the correct form for the late time behavior of the OTOC, and the Lyapunov exponent is thus fixed uniquely.

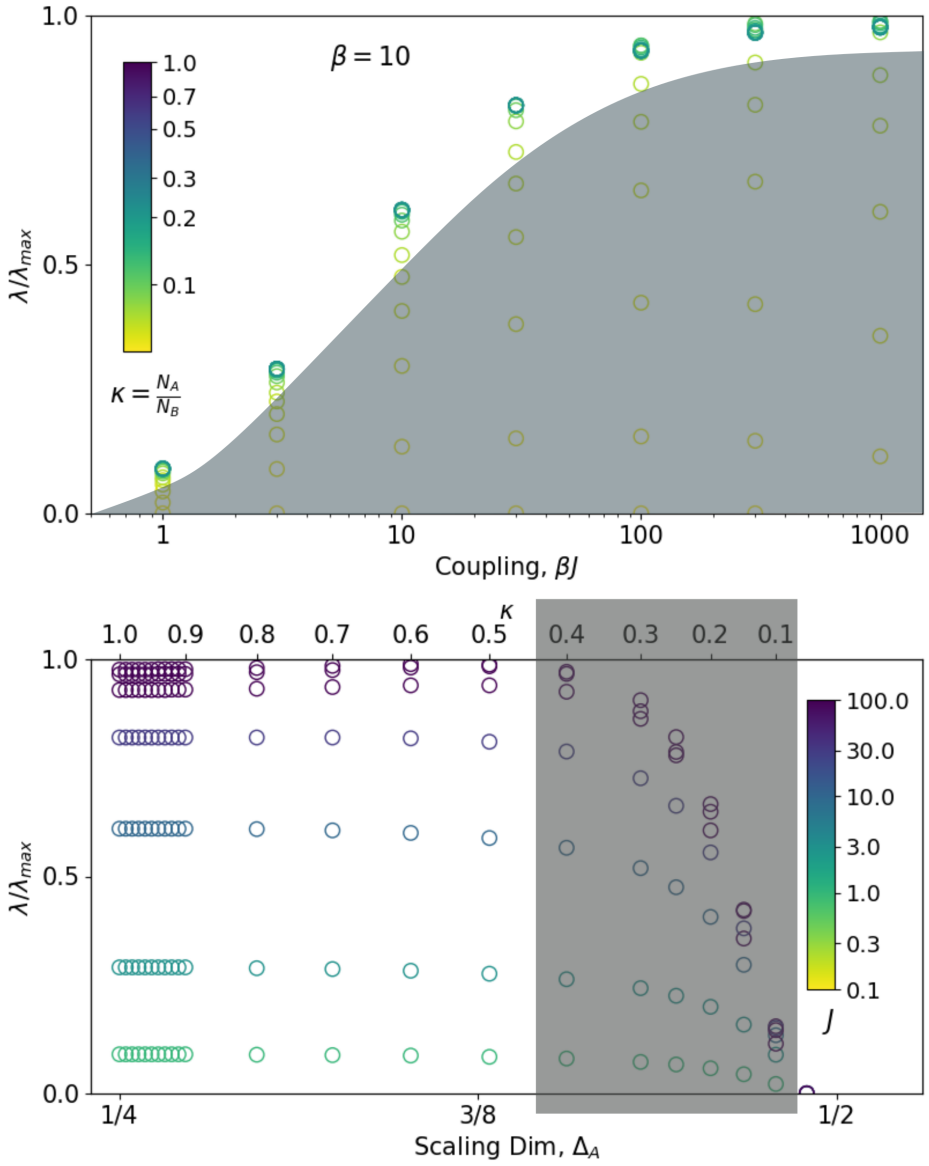

Figure 2.7: (Left) The Lyapunov exponent as a function of the coupling strength βJ and for various values $\kappa = N_A/N_B$. For $\kappa > 0.7$ and $\beta J \gtrsim 300$ the b-SYK model saturates the quantum chaos bound of $\lambda = 2\pi/\beta$. The special case $\kappa = 1$ has identical λ as in the SYK model. (Right) The Lyapunov exponent as a function κ for various values of βJ. We find that when $\kappa \gtrsim 0.5$ then λ is independent of κ. The apparent downturn of the Lyapunov exponent, as a function of κ, can be attributed to the inability of the numerics when the scaling dimensions for the two species are drastically different. In both figures, the grayed out region shows where the numerical results should not be trusted.

2.4. Results

2.4.1. Analytics and numerics

We now present and discuss the results of our numerical calculations and compare to analytically known limits. This will reveal some limitations of the numerical method rooted in numerous finite size effects. From the analysis in the preceding chapter, we know that the Lyapunov exponent λ is maximal in the conformal limit for all values of κ. Furthermore, we confirmed numerically that for $\kappa = 1$, then λ, as a function of J, has identical behavior as in the normal SYK model. This behavior has previously been studied in Ref. [19].

Numerically, we studied the behavior of λ as a function of βJ for various values of $\kappa = N_A/N_B$. Figure 2.7 (left) shows the Lyapunov exponent λ as a function of the coupling βJ for a variety of values of κ. The different values of κ are encoded in the color scale. We do not show values of $\kappa > 1$ because they are equivalent to those for $1/\kappa$ by symmetry upon exchange of the species. The figure suggests that λ for all curves with $\kappa \approx 1$ are approximately the same. Smaller values of κ seem to differ significantly in their value of λ (the gray shaded region is affected by strong finite size effects and the results should not be trusted, see discussion in Appendix 2.5.3). We find that the numerics allows to approach the fully conformal limit of the model, meaning $\lambda/\lambda_{\max}$ approaches 1 in the strong coupling limit for values $\kappa \approx 1$, in agreement with our analytical results.

For intermediate couplings βJ, which is beyond the reach of any analytical treatment, numerical calculations are more accurate [19]. Similar to Ref. [19], we find for this regime of J, that the Lyapunov exponent decreases following a $1/J$ behavior. In total, we find that for values of $0 \ll \kappa \leq 1$, the Lyapunov exponent is mostly agnostic to the population ratio κ.

It is instructive to analyze the κ dependence in more detail. In Figure 2.7 (right) we fix J and vary κ (or Δ_A). We observe that the value of λ is *independent* of κ up to some characteristic value of κ, after which it begins to decline (grey area). We argue that the downturn in λ is an artifact of the numerical method we are using. Essentially we are seeing a finite-size effect in that the time/frequency discretization in the numerics is not fine enough. We have checked for isolated points that the gray area can be pushed upon increasing the resolution.

An immediate question that follows is why the finite-size effects appear only for values of κ away from 1. This can be understood upon considering the scaling dimensions as a function of κ: decreasing κ increases the spread in scaling dimensions of the A and B Majorana fermions. This implies that one has to keep track of two time/and frequency scales that we need to accurately capture with our numerical

frequency-grid where the scaling limit of one of the two is pushed to larger times. Getting a good resolution of that requires a finer frequency grid at small frequencies. When κ deviates too much from 1 this becomes increasingly costly in terms of time/frequency steps. An extended discussion of the finite size effects in the two-fermion Green function is given in Appendix 2.5.3.

2.4.2. Discussion and Conclusion

Having established that the Lyapunov exponent is independent of κ, we can compare our results to a similar model presented in Ref. [135]. In that case, the authors find a Lyapunov exponent in the conformal limit which can be tuned by adjusting the relative populations of the different species of fermions. In our model, we find a stark contrast to this behavior. Instead, we find that our model's Lyapunov exponent is completely impervious to the relative number of fermion species. In the conformal limit, aside from showing this result in an explicit analytical calculation, we can motivate the result in a physical way, as a sort of "proof by contradiction". If for example, the $A-$ flavor Majorana had a smaller Lyapunov exponent, the diagrams contributing to its four point function proceed by a pathway in which they scatter into two $B-$ flavor Majoranas, which would then propagate with the greater Lyapunov exponent, before finally scattering back into two $A-$ flavor Majoranas. This forces both flavors to have exactly the same exponent, and a mathematical version of this argument is presented in Appendix 2.5.1.

The two-point function of the Majoranas are characterized by their scaling dimension, which is quite sensitive to the relative population ratio κ, so one would expect that the four-point function as characterized by the Lyapunov exponent would depend on κ as well, but we have shown conclusively that this is not the case for cases of strong, intermediate and weak coupling, which is quite surprising. An interesting future direction of study would be to consider what deformations should be introduced to the theory in order to have a different Lyapunov exponent for the two flavors of Majoranas.

The present work on the calculation of the Lyapunov exponent in the b-SYK model shows that the features of emergent conformal symmetry and maximal quantum chaos of the SYK model are quite robust to the couplings obeying additional internal symmetries. Besides the particular model considered here, there are many setups where parity, charge, spin, or general flavor symmetries of the underlying fermions carry over to the interaction matrix elements [58, 108, 110, 128, 129]. The methods used here readily carry over to those models and can be applied to the calculation of Lyapunov exponents and, in general, to the analysis of Bethe-Salpeter equations.

Acknowledgments

We acknowledge discussions with Y. Cheipesh, A. Kamenev, K. Schalm, M. Haque, and S. Sachdev. Extensive discussions with D. Stanford about the conformal limit of the OTOC are also acknowledged. SP thanks E. Lantagne-Hurtubise, O. Can, S. Sahoo, and M. Franz for many useful discussions related to SYK models and holography. This work is part of the D-ITP consortium, a program of the Netherlands Organisation for Scientific Research (NWO) that is funded by the Dutch Ministry of Education, Culture and Science (OCW). SP received funding through the European Research Council (ERC) under the European Union's Horizon 2020 research and innovation program.

Author Contributions

A.S.S and M.F contributed equally to this work.

2.5. Appendix

2.5.1. Mathematical consistency of the Lyapunov ansatz

The following short consideration for the diagram piece $\mathscr{F}_{00}$ shows why we expect only one 'global' Lyapunov exponent for all scattering channels. The other components of the four-point function can be treated with exactly the same argument. The starting point is

$$\mathscr{F}_{00}(t_1,t_2) = \int dt_3 dt_4\, K_{00}(t_1,t_2,t_3,t_4)\mathscr{F}_{00}(t_3,t_4) + K_{10}(t_1,t_2,t_3,t_4)\mathscr{F}_{10}(t_3,t_4) \quad (2.35)$$

where we use the definition

$$\begin{aligned} t_{1,2} &= t \pm \frac{1}{2}t_{12} \\ t_{3,4} &= \tilde{t} \pm \frac{1}{2}t_{34}\,. \end{aligned} \quad (2.36)$$

The factors of a half were included to keep the area element invariant under this transformation, $dt_3 dt_4 = d\tilde{t}\,dt_{34}$. After some algebra, for the ansatz f_{00} one finds

$$f_{00}(t_{12}) = J^2\frac{1}{2}\left(1+\frac{1}{\kappa}\right)\int d\tilde{t}\,dt_{34} G_A^R(t_{13})G_A^R(t_{24})\Big[\frac{1}{\kappa}\left(G_B^W(t_{34})\right)^2 e^{\lambda_{00}\tilde{t}-\lambda_{00}t} f_{00}(t_{34}) + \left(G_A^W(t_{34})G_B^W(t_{34})\right)e^{\lambda_{10}\tilde{t}-\lambda_{00}t} f_{10}(t_{34})\Big] \quad (2.37)$$

Now we Fourier transform according to

$$G_A^W(t_{34}) = \int \frac{\mathrm{d}\omega_a}{2\pi} e^{-i\omega_a t_{34}} G_A^W(\omega_a)\,. \quad (2.38)$$

If we calculate a sample term f_{00} to illustrate the point,

$$\begin{aligned} f_{00}(\omega) = J^2\frac{1}{2}\left(1+\frac{1}{\kappa}\right)\int \mathrm{d}t_{12} e^{i\omega t_{12}} \int \mathrm{d}\tilde{t} \int \mathrm{d}t_{34} \int \frac{\mathrm{d}\omega_a}{2\pi} e^{-i\omega_a(t-\tilde{t}+\frac{1}{2}(t_{12}-t_{34}))} \\ \int \frac{\mathrm{d}\omega_b}{2\pi} e^{-i\omega_b(t-\tilde{t}-\frac{1}{2}(t_{12}-t_{34}))} G_A^R(\omega_a)G_A^R(\omega_b) \\ \int \frac{\mathrm{d}\omega_c}{2\pi}\int \frac{\mathrm{d}\omega'}{2\pi} e^{-i(\omega_c+\omega')t_{34}}\left[\tilde{K}_{00}(\omega_c)f_{00}(\omega')e^{\lambda_{00}\tilde{t}-\lambda_{00}t} + \tilde{K}_{10}(\omega_c)f_{10}(\omega')e^{\lambda_{10}\tilde{t}-\lambda_{00}t}\right] \end{aligned} \quad (2.39)$$

we notice that there are three time integrations that result in delta functions, but 4 t-like variables. In the case of the first term in the square brackets, since it only appears in the combination $(\tilde{t}-t)$, this eliminates a variable, and there are sufficient constraints to make it only depend on ω variables. However, in the new term coming from flavor-mixing of the b-SYK, this is not true any more. This is a signal of a

breakdown of the ansatz Eq. (2.21). We thus see that for consistency we must impose that $\lambda_{00} = \lambda_{10}$. By repeating the argument for the other components of $\mathscr{F}$, it can be shown that all Lyapunov components should be the same, $\lambda_{ij} = \lambda$, and that there is only one Lyapunov exponent governing the behavior of the model.

2.5.2. Recovery of the maximal Lyapunov exponent of the regular SYK

At $\kappa = 1$, the numerics reflect that the Lyapunov exponent of the model is the same as the maximal value of regular SYK. This can be understood by looking at the kernel Eq. (2.17). At $\kappa = 1$, the scaling dimensions of both the A and B majoranas become $\frac{1}{4}$, and hence $G^A(\tau) = G^B(\tau) \equiv G(\tau)$, the 2 point function of regular SYK. The kernel then factorizes into the product of a function of the four imaginary times, and a constant matrix.

$$K(\tau_1 \cdots \tau_4) = -J^2 G(\tau_{13}) G(\tau_{24}) G(\tau_{34})^2 \begin{pmatrix} 1 & 2 \\ 2 & 1 \end{pmatrix} \tag{2.40}$$

The constant matrix in question has eigenvalues -1 and $+3$. The latter eigenvalue makes the kernel mathematically the same as the one for regular SYK, and hence the Lyapunov exponent should be the same. Furthermore, it is for this reason that the special case of $\kappa = 1$ allows the kernel to be diagonalized in the basis of the conformal blocks labeled by h. For $\kappa \neq 1$, the four components of the kernel transform differently under transformations of the conformal group.

2.5.3. Finite-size dependence of two-point functions and Lyapunov exponents

In this section, we briefly comment on the sensitivity of the two-point function to the finite-size cut-offs introduced when numerically solving the Schwinger-Dyson equations for the b-SYK model. To solve the coupled b-SYK equations (Eq. (2.9) and below), we discretize the semi-infinite positive timeline by introducing a long time cut-off T and a finite number of time steps N inbetween. This introduces a discretized time-step $\Delta t = T/N$ and frequency step $\Delta\omega = 2\pi/T$. To avoid the discontinuities at $\omega = 0$ and $t = 0$, we choose a time grid that is $t_n = \Delta t \cdot (n + 1/2)$, and similarly for the frequency grid.

We can study of the effects of varying T and N on $G^B(t)$.

In Figure 2.8 we show an example for $\kappa = 0.3$, $\beta = 10$, and $J = 10$. We fix the number of discretization points to $N = 2^{19}$ and plot $G^B(t)$ for several values of T. We have cut off the plot at the first negative value of G^B. In the plot, we observe two qualitative effects of changing T: First, upon increasing T, we find that the decay time (slope)

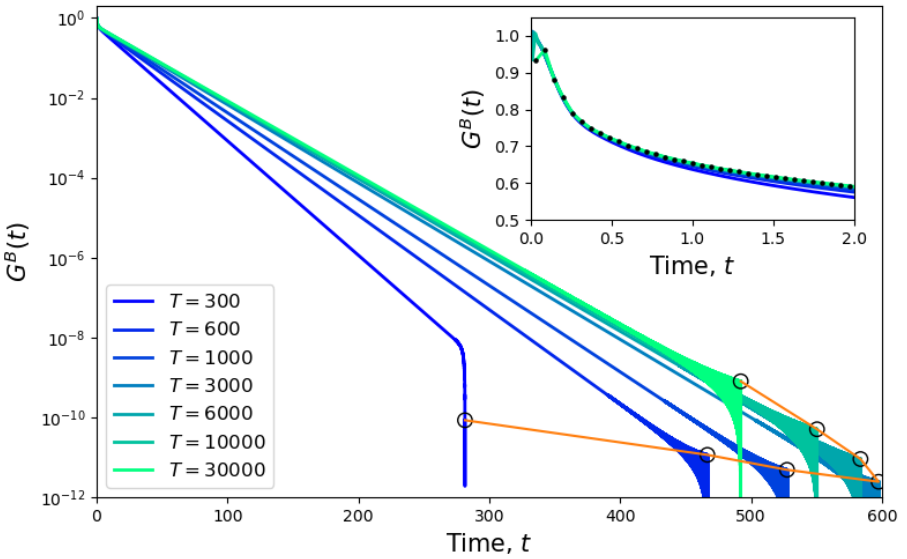

Figure 2.8: The Green function $G^B(t)$ for $\kappa = 0.3$, $\beta = 10$, $J = 10$. The number of discretization points is fixed to $N = 2^{19}$ and the length of the time-grid T is varied. The figure shows that increasing T gives a better estimate of the decay-time for the Green function, but if T is taken to be too high, numerical accuracy of the Green function is lost. The sweet-spot is here at $T = 3000$. Black circles marks the position of (the point before) the first negative G, and is an estimate of the size of the numerical noise.

of the Green function increases (decreases). Thus, increasing T, we allow $G^B(t)$ to behave as if the time axis was really semi-infinite. One can perform a $1/T$ analysis and finds that the lines have a well-defined slope in the $T \to \infty$ limit.

Secondly, which is more subtle, we see that making T too large decreases the quality of the approximation for $G^B(t)$, with the optimal number being around $T = 3000$. We arrive at this number by the following argument: In the plot, we only show $G^B(t)$ until the first non-negative value (at time t_C). The solid-looking wedge shape that appears just before the first negative number is the effect of numerical oscillations that (as G decreases) become relatively more important. From the height where the "wedges" disappear (black circles connected with an orange line), we can approximate the size of this numerical error. By inspection, we see that the smallest numerical errors (and also the largest t_C) happen for $T = 3000$. We can understand the loss by noting that as T grows, then (for fixed N) Δt also grows. In the inset of the figure, one can see that at $T = 30000$, Δt is so large that it even affects the continuity of the curve $G^B(t)$.

Choosing the appropriate T, is thus affected by the range of the Green function decay, which in turn is affected by κ, the ratio between the two species. In the numerics that we present in the main text, we worked with a fixed N and T, which are good when $\kappa \approx 1$ but not when κ is increasingly asymmetric. Errors in the two-point func-

tion will propagate and influence the calculations of the Lyapunov exponent and explain why we see the downturn of λ at a characteristic value of κ.

3

A BCS-Josephson Wormhole in coupled superconducting Yukawa-SYK metals

Attribution

The work in this chapter has been done jointly with Stephan Plugge and Koenraad Schalm, and is a manuscript under preparation.

Abstract

We show that two Yukawa-SYK models with a weak tunneling contact can have an exotic superconducting hybrid thermofield-double-like state holographically dual to a traversable wormhole connecting two black holes with charged scalar hair. The hybrid thermo-field-double/wormhole state is distinguishable by anomalous scaling of revival oscillations in the fermionic Green's function, while the BCS-like superconducting condensate is responseless. The existence of this TFD/wormhole state surprisingly shows that the some quantum critical effects can survive the phase transition to superconductivity. It also suggests a more strange metallic TFD/Josephson wormhole can exist correlated with superconductivity at strong coupling, where Cooper pairs persist above the critical temperature.

3.1. Introduction

The realization that the quantum critical strongly correlated groundstate of the Sachdev-Ye-Kitaev model is in the same universality class as the groundstate of holographic models of charged anti-de-Sitter black holes has opened up a wide avenue to study exotic gravitational questions with quantum-mechanical Hamiltonians. One such question is the existence of traversable wormholes. Maldacena and Qi [105], based on an earlier work of Gao, Jafferis and Wall [136] and more recently others [60, 137–145], showed that (marginally) relevant tunneling interactions between two such SYK Hamiltonians could induce a phase transition to a finite temperature "wormhole" state as the temperature is lowered. The quantum mechanical understanding of this transition is as follows. At high temperatures, where tunneling is minimal, the state of the coupled system is arbitrarily close to two independent decoupled thermal ensembles at high temperature — holographically dual to two black holes

$$\rho_{\text{2BH}} = \frac{1}{Z_\beta^2} \sum_{n_1,n_2} e^{-\beta(H_1+H_2)} |n_1, n_2\rangle\langle n_1, n_2| \,. \tag{3.1}$$

The density matrix can also be written as a state in a doubled system

$$|\text{2BH}\rangle_\beta = \frac{1}{Z_\beta^2} \sum_{n_1,n_2} e^{-\beta(E_{n_1}+E_{n_2})} |n_1, \bar{n}_2\rangle \,, \tag{3.2}$$

where $|\bar{n}\rangle = |\Theta n\rangle$ with Θ an anti-unitary symmetry of the SYK model (usually CPT). As one lowers the temperature and the tunneling becomes stronger the thermodynamically preferred state is a different one. This is the state close to the maximally entangled so-called Thermo-Field-Double state — holographically dual to a wormhole connecting the two black holes

$$|\text{WH}\rangle_\beta = |\text{TFD}\rangle_\beta = \frac{1}{\sqrt{Z_\beta}} \sum_n e^{-\frac{\beta}{2}E_n} |n, \bar{n}\rangle \tag{3.3}$$

Here $Z_\beta = \sum e^{-\beta E_n}$ is the partition function of a single SYK model.

Macroscopically it is a first order transition driven by the relevancy of the tunneling interaction, but the telltale sign of the wormhole is more subtle than a macroscopic order parameter. When the high temperature state is in the strongly correlated regime such that it is the finite temperature extension of the quantum critical SYK groundstate dual to a black hole, rather than a thermal gas of free quasiparticles, the low temperature "wormhole" state can remember this critical origin in that its spectrum can be better explained as a perturbation of its quantum critical spectrum rather than a perturbation around a free system. Specifically, the near-AdS_2 symmetry group (time-reparametrizations modulo $PSL(2)$) that defines the quantum critical state of a single SYK system, continues to determine the spectrum of the

coupled system even when the groundstate changes to the TFD/WH state [105]. This deformed N-AdS$_2$ spectrum has a uniquely characteristic fixed spacing between levels similar to that of a harmonic oscillator: $E_n = E_{\text{gap}}(1 + \frac{1}{\Delta} n)$, $n \in \mathbb{N}$, with the groundstate energy $E_{\text{gap}} \sim \lambda^{\frac{1}{2-2\Delta}}$ proportional to a non-perturbative non-analytic fractional power of the tunneling strength λ in terms of the IR critical scaling dimension Δ of a fermionic excitation. This fixed integer spacing in units of c is observable in characteristic revivals in a linear response probe, as convincingly shown in subsequent numerical simulations [134, 143, 146, 147]. From the dual holographic gravitational perspective this revival is a perturbation that has fallen into a black hole, traveled through the wormhole and back. One should be careful: Revival-signatures in linear response can have many origins and not all revivals are dual to a signal traversing a wormhole. The key aspect is the non-analytic dependence of the gap E_{gap} and the spacing $\Delta E = E_{\text{gap}}/\Delta$ on the relevant tunneling strength λ. Even within these SYK-models, if this relevant coupling becomes strong, the system still shows revivals. But as the system has now crossed over to a free-fermion state, the gap and the level spacing underlying the revivals are now an integer analytic power of tunneling strength. It is just a reflection of the regularity of the underlying standard free particle harmonic oscillator spectrum. Fig.3.1A summarizes this phase diagram of the 2BH/WH transition in quantum critical SYK models.

However theoretically appealing, in actual physical systems quantum critical states are rare. Moreover, experimentally they are fragile and extremely susceptible to decay to a conventional ordered state, usually a BCS superconductor. It is conjectured that in 2D systems this is in fact always the case [41, 42, 148]. The SYK-like quantum critical systems are essentially 0D quantum dots, but 2D extensions can preserve many of its features including the N-AdS$_2$ like structure of its groundstate [33]. Some of the fragility of this quantum critical grounstate is suppressed by a large N-limit, but some is also by construction. In particular the simplest SYK models do not preserve time-reversal symmetry and singlet Cooper pairs are not stable enough to form a long range coherent state. More realistic models must preserve (some) time reversal symmetry to allow pairing. One such model is the Yukawa-SYK model constructed in [24]. This is a quantum critical superconductor with a tunable pairing strength and T_c whose condensate is not controlled by the density of states at the Fermi surface [24, 149]. In particular, the charge neutral critical state with no Fermi surface is already unstable towards superconductivity. It is able to do so as the density of states is large even at charge neutrality, which allows a macroscopic condensate to form. For a large part of the phase diagram this superconductivity indeed prevents the emergence of quantum criticality, but this view has been challenged recently in Ref. [150].

The question we address in this article is whether the exotic revival physics dual to a wormhole state persists in tunneling contacts between such more realistic SYK mod-

els as Yukawa-SYK that do exhibit superconductivity. Naively one would think not, in accordance with the wisdom that superconductivity prevents quantum criticality. The onset of superconductivity gaps the low-energy spectrum and this ought to destroy to characteristic fixed level spacing responsible for the wormhole revival physics. The loophole is that in these models superconductivity is tunable and a window may exist that nevertheless allows for a sufficiently regular spectrum that a wormhole like state survives. The holographic gravitational dual of such a state would be a wormhole with a scalar condensate also known as scalar hair. An argument in favor that such state could result from this construction is the fact that the thermofield-double state is a formal purification of the straightforward thermal mixed state of a single YSYK model. It must therefore exist, and perhaps the better posed question is whether this protocol contructs the TFD-state as the groundstate of the coupled YSYK system.

In this article we report that this indeed turns out to be the case and the loophole is realized — in a particular way. There exists indeed a strongly entangled tunneling contact state between two superconducting YSYK systems that nevertheless has a low-energy spectrum controlled by the N-AdS_2 of the critical state. Pictorially this is represented in Fig. 3.1B. The particularity of this state is that the regime where this state is found is one where superconducivity manifests itself in the fermionic spectrum by the BCS-like opening of gap. Qualitatively, this means that Cooper pairs condensate immediately upon binding and there are no uncondensed bound-fermion states in the spectrum. The "wormhole" state is therefore the honest TFD of the fermionic excitations on top of the BCS-like groundstate. This is in contrast to a more BEC-like superconductivity where bound states form first, exist as independent asymptotic excitations in the spectrum, and only condense at a lower temperature. In the fermionic spectral function this manifests itself as a depletion of the gap/growth of a peak at finite energy, as is observed in real high T_c strange metals for instance [151–155]. The TFD/"wormhole" state of such a system would have the same formal form as Eq. (3.3), but now the energy states would contain both fermionic and bosonic excitations. In principle the YSYK model we study has a regime where such BEC-like superconductivity occurs [24]. However, generically this originates from an impurity-like normal state above T_c and not from the quantum critical state holographically dual to black holes. We have therefore not studied this here.

Tunneling contacts between superconducting systems — a Josephson junction — are of course an enormously well studied and useful arena of physics. As the Josephson current is the tunneling of Cooper pairs, an immediate question is whether the Josephson current can also show revivals characteristic of a "wormhole". Even if quantum in origin, the dominant Josephson effects are macroscopic thermodynamic manifestions: they are captured by the Landau-Ginzburg free energy. The universal-

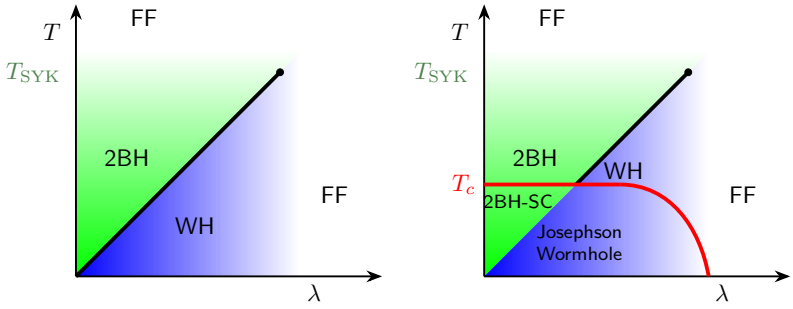

Figure 3.1: Schematic phase diagram of two coupled Yukawa-SYK systems without (left) and with superconductivity (right). When superconductivity is suppressed, there is a first order phase transition at fixed $\lambda < \lambda_{\rm SYK}$ for $T \sim \lambda$. There the system transitions from a intermediate temperature $T \lesssim T_{\rm SYK}$ state of essentially two decoupled thermal strongly correlated SYK systems holographically dual to two black holes (2BH), to a low temperature thermofield double state with specific cross-correlations holographically dual to wormhole (WH). At very high temperatures $T \gg T_{\rm SYK}$ or very high tunneling coupling $\lambda \gg \lambda_{\rm SYK}$ the coupled system is in a free fermion phases that are smoothly connected to each other. When superconductivity is included. The above is valid for an intermediate value of the averaged Yukawa-YK-coupling in terms of the bare boson mass $g_{\rm SYK}/\omega^{3/2} \sim 0.5$, the two-black-hole phase first becomes a two essentially independent superconductor phase, holographically dual to two hairy black holes (2BH-SC). This state crosses over around the value of the putative 2BH/WH phase-transition to a excitation spectrum on top of the superconducting groundstate that is characteristic of the thermo-field-double/wormhole state.

ity of the latter precludes any significant change in observational responses due to an underlying TFD/wormhole state. We confirm this by a computation of the DC Josephson current in the TFD/wormhole state. Similar to non-superconducting SYK models, the manifestation of the wormhole is more subtle. A more fine grained analysis of Josephson physics may reveal other effects in addition to the single fermion revivals. We leave this for further study. Nevertheless, as the superconductor-superconductor wormhole is supported by a tunneling interaction, to christen it the BCS-Josephson wormhole seems apt.

Section 3.2 describes the YSYK model, the tunneling interaction coupling two YSYK models and the effective Schwinger-Dyson equations controlling the large N-limit of the model after disorder averaging over random four-fermion interactions. Section 3.3 describes the TFD/wormhole state when superconductivity is artifially surpressed to connect with earlier coupled SYK wormhole results and set the stage for Section 3.4 where we exhibit the existence of the BCS-Josephson wormhole, i.e. a thermodynamic phase transition to a superconducting TFD-state. From the free energy of the total system we compute the DC Josephson current to show that it is not affected by the underlying state change as could have been surmised by the fact that the TFD-state is thermodynamically in the same phase as the ordinary BCS state. We conclude with a brief outlook in the conclusion Section 3.6.

3.2. Two Yukawa-SYK models with a tunneling contact with shared disorder.

The Yukawa-SYK model describes a quantum dots with N flavors of spin-$\frac{1}{2}$ fermions and M flavors of bosons with Hamiltonian [24]

$$H_{\text{Y-SYK}} = -\mu \sum_{i=1}^{N} \sum_{\sigma=\uparrow,\downarrow} c^{\dagger}_{i,\sigma} c_{i,\sigma} + \sum_{k=1}^{M} \frac{1}{2}\left(\pi_k^2 + \omega_0^2 \phi_k^2\right) + \frac{\sqrt{2}}{N} \sum_{i,j,k} \sum_{\sigma} g_{ijk} c^{\dagger}_{i,\sigma} c_{j,\sigma} \phi_k \,. \quad (3.4)$$

In a single instance of the model the complex couplings $g_{ijk} = g^{'}_{ijk} + i g^{''}_{ij,k}$ are randomly drawn from an ensemble with zero mean and variance

$$\begin{aligned} \langle g'_{ijk} g'_{lmn} \rangle &= (1 - \frac{\alpha}{2}) g^2 \delta_{kn} (\delta_{il}\delta_{jm} + \delta_{im}\delta_{jl}) \,, \\ \langle g''_{ijk} g''_{lmn} \rangle &= \frac{\alpha}{2} g^2 \delta_{kn} (\delta_{il}\delta_{jm} - \delta_{im}\delta_{jl}) \,, \\ \langle g'_{ijk} g''_{lmn} \rangle &= 0 \,. \end{aligned} \quad (3.5)$$

For $\alpha = 1$ the hermitian matrix $g_{ijk} = (g_k)_{ij}$ is in the Gaussian Unitary ensemble; for $\alpha = 0$ the matrix is real and in the Gaussian orthogonal ensemble. The model is solvable after averaging over the ensemble and taking the double limit $N \to \infty$, $M \to \infty$ with $\kappa = M/N$ fixed. For $\alpha = 1$ the system has a quantum critical SYK groundstate for any value of the chemical potential μ and boson mass ω_0 with scaling dimensions Δ_f and Δ_b for the fermions and bosons respectively that are fixed by

$$\begin{aligned} 2\Delta_f + \Delta_b &= 1 \,, \\ \kappa \frac{\Gamma(1-\Delta_f)\Gamma(1-(\Delta_f+\Delta_b))}{\Gamma(\frac{1}{2}+\Delta_f)\Gamma(\frac{1}{2}+\Delta_f+\Delta_b)} &= -2\frac{\Gamma(\frac{1}{2}-\Delta_b)\Gamma(\frac{1}{2}-2\Delta_f)}{\Gamma(\Delta_b)\Gamma(2\Delta_f)} . \end{aligned} \quad (3.6)$$

(see Appendix 3.7.1). For $\alpha < 1$ the theory has a time-reversal preserving sector and allows for pairing and a stable superconducting phase. In particular, at $\alpha = 0$ for a small range of $g \sim \omega_0^{3/2}$ the phase diagram (Fig. 3.2) has a small window where the onset of superconductivity occurs from the finite temperature extension of the quantum critical Yukawa-SYK N-AdS$_2$ state holographically dual to a black hole [24, 26–28]. We shall choose the model with $\alpha = 0$ at charge neutrality $\mu = 0$ with that value of $g/\omega_0^{3/2} = 0.5$ and hold these fixed throughout this study; we shall also choose $\kappa = 1$ throughout. What shall be important later in Section 3.4, is that for this value the onset of superconductivity manifests itself in the fermionic spectral function by the opening of a gap (Fig. 6 in [24]), i.e. bound fermion states immediately condense and the spectrum of excitations does not contain bound-fermion states.

The two coupled system configuration that allows for entangled TFD phase at low temperatures is constructed by coupling two identical Yukawa-SYK models, i.e. with

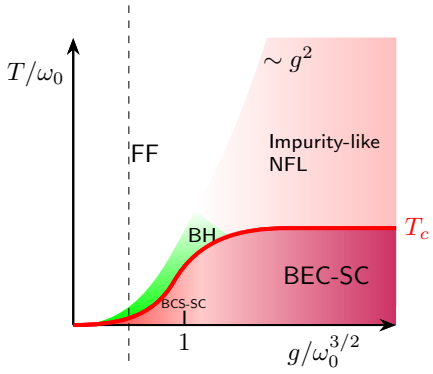

Figure 3.2: The phase diagram of a single Yukawa-SYK model with couplings drawn from the GOE from [24]. FF is a free-fermion phase; BH is the finite temperature version of the quantum critical N-AdS$_2$ SYK groundstate dual to a black hole. SC is the superconducting state which has a crossover from BCS-like SC to BEC-like SC as $g/\omega_0^{3/2}$ increases. At high temperatures for large g the model is controlled by an impurity fixed point. The dashed line denotes the value of the disorder-averaged coupling $g/\omega_0^{3/2} = 0.5$ we use in this in article such that the normal phase right above the superconducting transition is the quantum critical/BH phase.

the same random coupling constants *before disorder averaging*, together with a simple tunneling interaction. The joined model is then described by the following action

$$\begin{aligned} S &= S^{(1)}[g_{ijk}] + S^{(2)}[g_{ijk}] + S_c\,, \\ S^{(a)}[g_{ijk}] &= \int \mathrm{d}\tau \sum_{i,\sigma} c^{\dagger(a)}_{i\sigma}(\tau)\left(\partial_\tau - \mu\right) c^{(a)}_{i\sigma}(\tau) + \sum_k \phi^{(a)}_k(\tau)\frac{1}{2}\left(-\partial_\tau^2 + \omega_0^2\right)\phi^{(a)}_k(\tau) \\ &\quad + \frac{\sqrt{2}}{N}\int \mathrm{d}\tau \sum_{ijk,\sigma} g_{ijk} c^{\dagger(a)}_{i\sigma}(\tau) c^{(a)}_{j\sigma}(\tau)\phi^{(a)}_k(\tau)\,, \\ S_c &= \int \mathrm{d}\tau \sum_{i,\sigma} \lambda c^{\dagger(1)}_{i\sigma}(\tau) c^{(2)}_{i\sigma}(\tau) + \lambda^* c^{\dagger(2)}_{i\sigma}(\tau) c^{(1)}_{i\sigma}(\tau) \end{aligned} \tag{3.7}$$

Other tunneling couplings such as boson-boson tunneling $S = \int \mathrm{d}\tau J \phi^{(1)}_k \phi^{(2)}_k$ or correlated two-fermion tunneling $S = \int \mathrm{d}\tau g_{ijk} g_{lmk} c^{\dagger(1)}_{i\sigma}(\tau) c^{(2)}_{j\sigma}(\tau) c^{\dagger(1)}_{k\sigma'} c^{(2)}_{l\sigma'}$ + c.c. are possible. By dimensional analysis, such terms are less relevant in the IR. As a similar study for complex SYK models has shown [147], there is still a transition to a TFD/wormhole state, but is weaker, at lower temperature and harder to detect. Moreover, such boson-boson and correlated multi-fermion tunnelings are also dynamically generated at subleading order in λ. We will therefore not consider such couplings here.

The coupled system is solved by disorder averaging over the couplings g_{ijk} that are identical in subsystem (1) and (2) in each instance of the ensemble. Introducing bilo-

cal fields

$$G^{ab}(\tau,\tau') = -\frac{1}{N}\sum_i c_i^{(a)}(\tau)c^{\dagger}{}_i^{(b)}(\tau')$$
$$F^{ab}(\tau,\tau') = -\frac{1}{N}\sum_i c_i^{(a)}(\tau)c_i^{(b)}(\tau')$$
$$D^{ab}(\tau,\tau') = -\frac{1}{M}\sum_k \phi_k^{(a)}(\tau)\phi_k^{(b)}(\tau'). \tag{3.8}$$

through their respective self-energies $\Sigma_{ab}, \Phi_{ab}, \Pi_{ab}$ as Lagrange multipliers, one can perform the path-integral over the fermions. The resulting effective action in terms of these bilocal fields has a set of Schwinger-Dyson equations as saddle-point equations. Using the fact that the original action Eq.(3.7) has a $\mathbb{Z}_2$ mirror symmetry $c_1 \to c_2 e^{i\theta}$, $c_2 \to c_1 e^{-i\theta}$ where θ is the phase of the tunneling coupling $\lambda = |\lambda| e^{i\theta}$, the large N, M saddle-point Schwinger-Dyson equations can be expressed in terms of $G_d = G_{11} = G_{22}, G_{od} = G_{12} = e^{2i\theta} G_{21}$ etc only. Assuming time-translation invariance in addition, they are

$$\begin{aligned}
\Sigma_{ab}(\tau,\tau') &= \kappa g^2 D_{ab}(\tau,\tau') G_{ab}(\tau,\tau'), \\
\Phi_{ab}(\tau,\tau') &= -(1-\alpha)\kappa g^2 F_{ab}(\tau,\tau') D_{ab}(\tau,\tau'), \\
\Pi_{ab}(\tau,\tau') &= -2g^2 \left[G_{ab}(\tau,\tau') G_{ba}(\tau',\tau) - (1-\alpha) F_{ab}(\tau,\tau') \bar{F}_{ba}(\tau',\tau) \right],
\end{aligned}$$

$$\begin{pmatrix} G_{11} & F_{11} & G_{12} & F_{12} \\ \bar{F}_{11} & \tilde{G}_{11} & \bar{F}_{12} & \tilde{G}_{12} \\ G_{21} & F_{21} & G_{22} & F_{22} \\ \bar{F}_{21} & \tilde{G}_{21} & \bar{F}_{22} & \tilde{G}_{22} \end{pmatrix} = \begin{pmatrix} i\omega_n - \Sigma_{11} & -\Phi_{11} & -\lambda - \Sigma_{12} & -\Phi_{12} \\ -\bar{\Phi}_{11} & i\omega_n - \tilde{\Sigma}_{11} & -\bar{\Phi}_{12} & \lambda^* - \tilde{\Sigma}_{12} \\ -\lambda^* - \Sigma_{21} & -\Phi_{21} & i\omega_n - \Sigma_{22} & -\Phi_{22} \\ -\bar{\Phi}_{21} & \lambda - \tilde{\Sigma}_{21} & -\bar{\Phi}_{22} & i\omega_n - \tilde{\Sigma}_{22} \end{pmatrix}^{-\top},$$

$$\begin{pmatrix} D_{11}(i\nu_n) & D_{12}(i\nu_n) \\ D_{21}(i\nu_n) & D_{22}(i\nu_n) \end{pmatrix} = \begin{pmatrix} \nu_n^2 + \omega_0^2 - \Pi_{11}(i\nu_n) & \Pi_{12}(i\nu_n) \\ \Pi_{21}(i\nu_n) & \nu_n^2 + \omega_0^2 - \Pi_{22}(i\nu_n) \end{pmatrix}^{-\top}. \tag{3.9}$$

Here $\tilde{G}(i\omega_n) = -G^*(i\omega_n)$ is the Green's function for spin down fermions in the Nambu basis. In the fermionic matrix equation all self energies are evaluated at the Matsubara frequencies $\Sigma_{ab}(i\omega_n), \Phi_{ab}(i\omega_n)$. Details of the derivation are given in the appendix 3.7.1.

3.3. The YSYK-TFD/wormhole for the metallic normal state

To show that the N-AdS$_2$ quantum critical point of the time-reversal symmetry breaking non-superconducting version of the YSYK model has a TFD/wormhole state in the weak tunneling configuration of two coupled systems, we first study the coupled system with superconductivity suppressed. It is metallic for all temperatures. For this we set $\alpha = 1$ which breaks time-reversal symmetry completely. The Schwinger-

Dyson equations simplify to

$$\begin{aligned}
\det G &= (i\omega_n + \mu - \Sigma_d)^2 - (\lambda + \Sigma_{od})^2 \\
G_d(i\omega_n) &= \frac{i\omega_n + \mu - \Sigma_d}{\det G} \\
G_{od}(i\omega_n) &= \frac{(\lambda + \Sigma_{od})}{\det G} \\
\det D &= (\nu_m^2 + \omega_0^2 - \Pi_d)^2 - (\Pi_{od})^2 \\
D_d(i\nu_m) &= \frac{\nu_m^2 + \omega_0^2 - \Pi_d(i\nu_m)}{\det D} \\
D_{od}(i\nu_m) &= \frac{\Pi_{od}}{\det D} \\
\Sigma_{(o)d}(\tau) &= \kappa g^2 D_{(o)d}(\tau) G_{(o)d}(\tau) \\
\Pi_{(o)d}(\tau) &= -2g^2 G_{(o)d}(\tau) G_{(o)d}(-\tau)
\end{aligned} \tag{3.10}$$

Note from the last two equations that the interacting part of the Schwinger-Dyson equations for the off-diagonal components is just a copy of the interacting part of the Schwinger-Dyson equations for the diagonal part and that they do not mix. These equations can be solved numerically in imaginary time and Matsubara frequency.

We first delineate the phase diagram of the coupled metallic $\alpha = 0$ YSYK system as a function of T and the coupling strength λ already sketched in Fig. 3.1A. At high temperature, when $T \gg T_{SYK} \sim g^2/\omega_0^2$ for any λ the system is in a nearly free fermion phase, where the interactions g and tunneling λ only give small perturbative corrections to the free fermion Fermi-Dirac density matrix state. The diagonal Green's function is well approximated by $G_d(\tau) \sim -\frac{1}{2}\,\mathrm{sgn}(\tau)$ at small time scales. Correspondingly, $G_d(i\omega_n) \sim \frac{1}{i\omega_n}$. as seen in the high frequency tail of the inset in Fig. 3.8. This represents the situation in which the fermions are essentially separately free in each dot.

For very large λ this phase continues to extend to lower temperatures as well. For $\lambda \gtrsim g^2/\omega_0^2$ the tunneling coupling is more dominant and essentially acts as an "off-diagonal" mass term between the two systems. After diagonalization one expects a gapped state with $E_{\text{gap}} \sim \lambda$ and this gap prevents a flow to a quantum critical state. The diagonal Green's function shows this gap and has a long time behavior for $\frac{1}{E_{\text{gap}}} \lesssim \tau \lesssim \beta$ that, as behoves a nearly free fermion system, is well approximated by turning off the self-energies in Eq. (3.10)

$$\begin{aligned}
G_d^0(\tau) &= \int_{-\infty}^{\infty} \frac{d\omega}{2\pi} \frac{i\omega}{(i\omega)^2 - \lambda^2} \\
&= -\frac{1}{2}\,\mathrm{sgn}(\tau) e^{-\lambda|\tau|}.
\end{aligned} \tag{3.11}$$

See Fig. 3.3. This represents a situation when the fermions just occupy the ground state of the cross coupling part of the hamiltonian, but are otherwise free. When

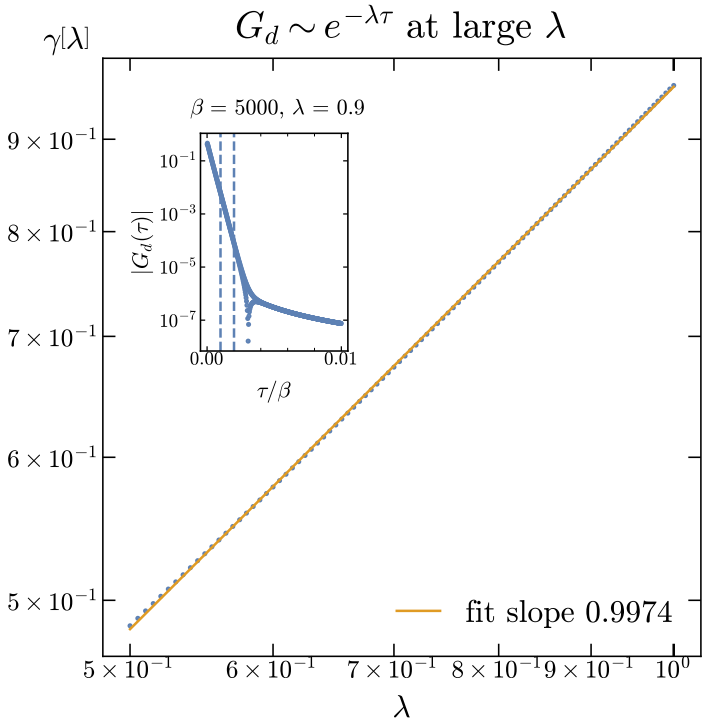

Figure 3.3: For large $\lambda \gtrsim g^2/\omega_0^2$, the diagonal fermion Green's function has a gap that scales linearly with λ, and is well approximated by Eq. 3.11.

analytically continued to the real axis, the spectral function would simply represent a quasiparticle pole at $\pm\lambda$. Formally this is the same phase as the high temperature phase as it simply the irrelevance of mass at high temperatures as is reflected in the smooth deformation of the one Green's function into the other.

At small $\lambda \lesssim g^2/\omega_0^2$ there are different phases. Now the YSYK coupling g is more important. From dimensional analysis, it can be expected to become important at an energy scale of $T_{SYK} \sim g^2/\omega_0^2$ Below this temperature a single YSYK system is in the finite temperature version of the quantum critical state, rather than a perturbatively interaction free Fermi gas. This is the state that is holographically dual to an AdS_2 black hole [156]. Including only a weak tunneling coupling λ the full state of the coupled system will still be very close to each of the two YSYK systems being in its own finite-T-QC/BH state Eq.(3.2) when the temperature is still on the high side $T \gtrsim \lambda$. This is what the numerics shows. In Fig. 3.4 the orange curve compares the full two YSYK numerics to a single YSYK model at $T > \lambda$. The diagonal Green's functions $G_d(\tau)$, $D_d(\tau)$ are indistinguishable from the single YSYK model one. The off-diagonal Green's functions are significantly smaller indicating some communication

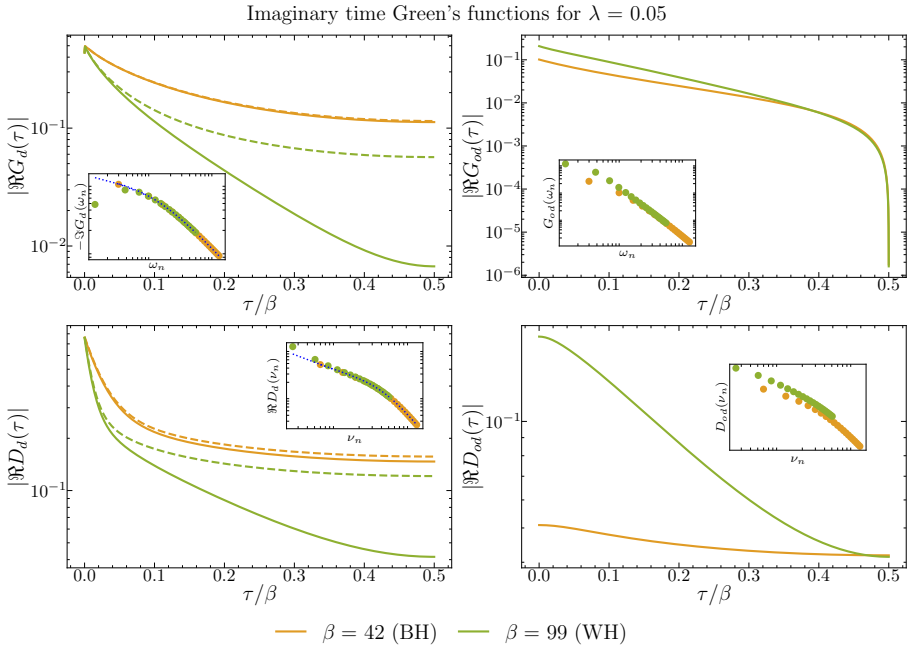

Figure 3.4: Imaginary time Green's functions at on lowering temperature at fixed λ in the metallic state. The dotted lines show the exact numerical solution to the one-sided model, i.e. when $\lambda = 0$, at the corresponding temperature. These figures indicate that in the wormhole phase, off-diagonal correlations are enhanced and diagonal correlations are suppressed. The insets show the frequency dependence of the respective Green's functions.

but suppressed by the smallness of the tunneling coupling.

The numerics can also confirm more precisely that it is the single YSYK QC state and its emergent conformal symmetry that is seen. At low frequencies, $T \ll \omega \ll g^2/\omega_0^2$ the diagonal Green's functions scale with a power law

$$G(\tau) \sim \frac{1}{|\tau|^{2\Delta_f}}, \tag{3.12}$$

$$D(\tau) \sim \frac{1}{|\tau|^{2\Delta_b}}. \tag{3.13}$$

In these equations, Δ_f and Δ_b are the scaling dimensions of the fermions and bosons in the single YSYK model respectively, given by the solutions to Eqs. (3.6). Fig. 3.4 inset shows this powerlaw behavior in the numerically exact solutions for this case.

On further lowering temperature to $T \lesssim \lambda$ at low $\lambda \ll g^2/\omega_0^2$ the state with power law correlations changes over into a state with exponentially decaying correlations in a first order phase transition. This is shown in the green curves in Fig. 3.4. This is a phase transition driven by the tunneling coupling as predicted and as can be seen

by comparison to the single sided YSYK Green's function for the same variables. The new state is the TFD/Wormhole state characterized by a gap and a linearly periodic spectrum $E = E_{\text{gap}}(1 + \frac{1}{\Delta}n)$. The gap is directly visible in the single fermion Green's functions in their exponential decay at large times

$$G_d(\tau) \sim e^{-\gamma\tau}. \tag{3.14}$$

The size of the gap γ is controlled by λ and its leading functional dependence can be understood from the scaling properties of the tunneling interaction as a perturbation of the quantum critical state [105]. In the bilocal formulation of the action this term is (see Appendix. 3.7.1 Eq.(3.43))

$$S_{\text{tunnel}} = \int \mathrm{d}\tau \mathrm{d}\tau' \lambda G_{12}(\tau, \tau') \,, \tag{3.15}$$

and hence at the quantum critical point $\lambda \sim \Lambda^{2-2\Delta_f}$ where Λ is the RG scale of the theory. Hence just below the transition we expect the gap to scale as

$$\gamma[\lambda] \sim \lambda^{\frac{1}{2-2\Delta_f}}. \tag{3.16}$$

This scaling is indeed seen by extracting the gap γ from the logarithmic derivative of the single fermion Green's function $G_d(\tau)$ in the long time regime for various λ at fixed $T \ll \lambda$ in the TFD/Wormhole phase: Fig. 3.5. The single boson Green's function exhibits the same gap $D \sim e^{-\gamma\tau}$ as there is only one energy scale that can be constructed using λ consistent with the dimensional analysis of Eq. (3.15). As can be seen from the insets in Fig. 3.5, although the scaling of the exponent γ with the coupling λ is according to Eq. (3.16) for both the bosons and the fermions, the numerical prefactor is different for the two cases.

This specific non-analytic scaling of the gap $\gamma \sim \lambda^{\frac{1}{2-2\Delta_f}}$ with the tunneling strength is the first indication that the gapped state obtained after the phase transition is indeed the TFD state holographically dual to an an eternal traversable wormhole(WH) geometry. The more detailed prediction is that the spectrum also has linearly spaced excited states. This would be very clearly visible as peaks in the frequency spectrum in numerical solution to the real time Schwinger-Dyson equations. Though in the real time numerics in Fig. 3.8 we can clearly see the gap development in the emergence of a single peak as temperature is lowered from $T \gg \lambda$ to $T \ll \lambda$, no other peaks are visible for the parameters and accuracy with which we are able to solve the system. This is in contrast to the results for Majorana and complex-SYK in [134, 147] where these excited states are clearly visible in the spectral density $\rho \sim -\text{Im}G$. However, we are able to see signatures of precisely these linearly spaced excited states in the numerical solution to the imaginary time Schwinger-Dyson equations. The imaginary times numerics are more stable and we are able to compute at much lower temperatures where thermal broadening plays less of a role. For a system with well

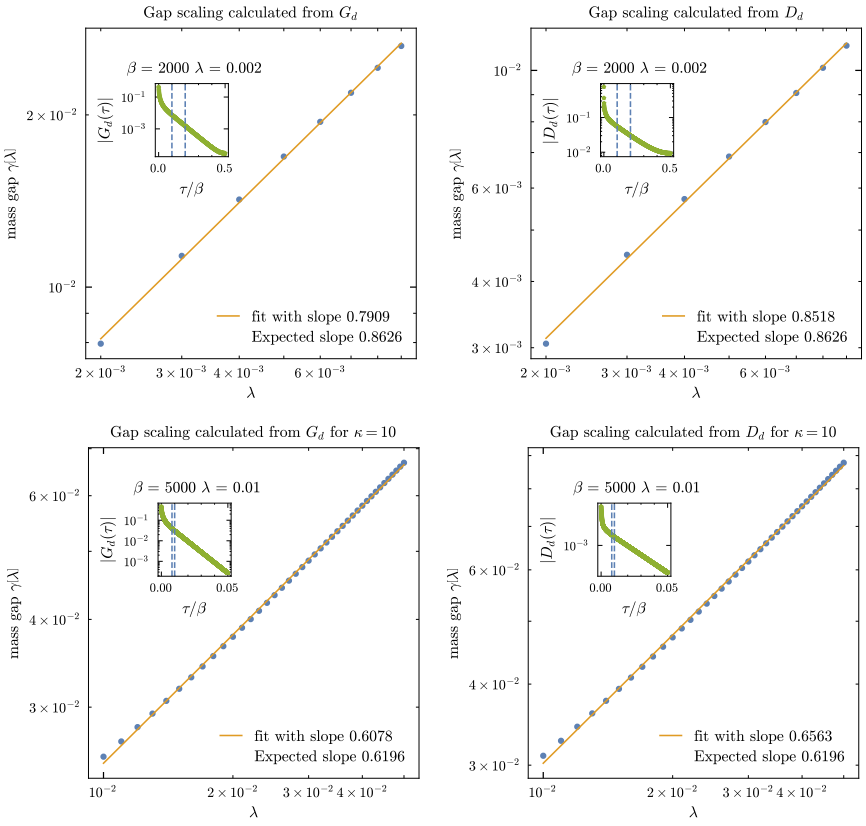

Figure 3.5: Scaling of the gap with the cross coupling λ. Panels(a) and (b) show the diagonal fermion and boson green's function respectively for $\kappa = 1$ and $\Delta = 0.42$ respectively. Panels (c) and (d) show the same scaling upon changing the effective slope by increasing κ to 10, and hence reducing Δ to 0.193. There is good agreement between the expected $\lambda^{\frac{1}{2-2\Delta}}$ scaling based on dimension analysis to the exact numerical solution. The insets show the exponential behavior of the respective Green's functions, and the window marked with the purple dotted lines indicate the region where the fit was performed for each data point of the main panels.

defined asymptotic states that only interact locally the asymptotic Greens function in imaginary time at very low temperature will take the form

$$G(\tau) \sim a_0 e^{-E_0\tau} + a_1 e^{-E_1\tau} + a_2 e^{-E_2\tau} + \dots \tag{3.17}$$

Here $E_0, E_1, E_2, \dots$ are the energies of the lowest excited states. Fig. 3.6 shows that subtracting out the dominant contribution of the gapped groundstate with $E_0 = c\Delta$ shows a clear remaining exponential decay whose exponent should be proportional to $E_1 = c(\Delta + 1)$. We know the analytic value of $\Delta = 0.42037\dots$ for these parameters, see Appendix 3.7.2. From this we can extract $c = E_{gap}/\Delta$ and predict $E_1 = c(\Delta + 1)$. The predicted slope is up to two digits accurate with the fitted slope; see Fig. 3.6.

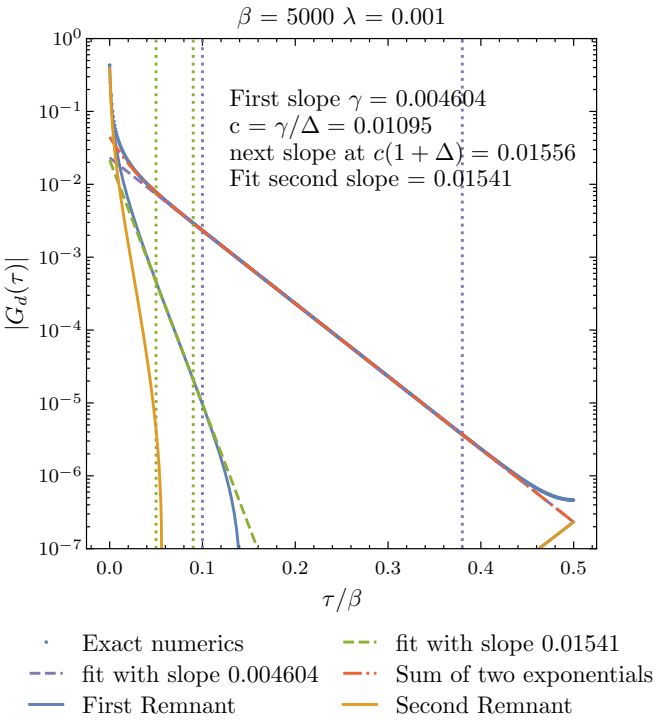

Figure 3.6: First subleading exponent in the imaginary time numerics. The vertical dotted lines of each color indicate the window at which the fit of the corresponding color was performed.

This is a strong second sign that the state at $T \lesssim \lambda$ for $\lambda \ll g^2/\omega_0^2$ is indeed the TFD/wormhole state of the YSYK model.[1]

In coupled Majorana [105, 134] and complex SYK models [147] the physics underlying the diagonal Green's functions jump from power law to exponential decay is a first order phase transition. In the gravitational dual this is a so-called Hawking-Page transition between a two black hole configuration and a wormhole. As the gravitational dual of quantum critical ground state of the non-superconducting Yukawa-SYK and Majorana and complex SYK models are essentially the same, we expect the same here. This is what we find and is illustrated in the free energy of the coupled YSYK system shown in Fig. 3.7. Though not perfectly discontinuous, the derivative of the free energy exhibits a clear jump. Furthermore, while for temperatures away from the critical point, the numerical solution is unique upon annealing both up-

[1] Fitting multiple exponentials is notoriously difficult and small fitting adjustments can result in large changes in the value of the exponent. A visible cue is the residuals after the leading exponential(s) is/are subtracted. The remainder needs to extend at least for a small window into the previously fit region with no kink at the edge of the fitting region, as a sign that the data was not overfit.

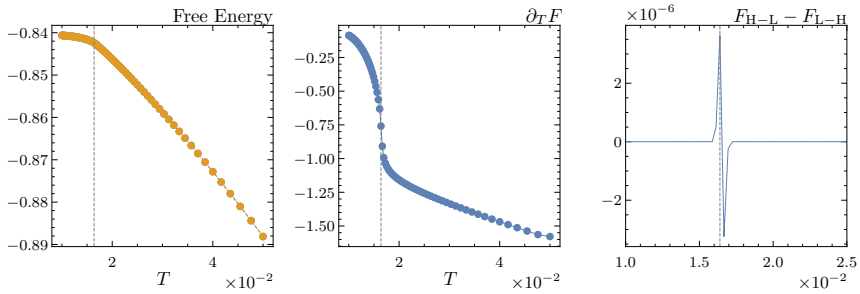

Figure 3.7: Free energy as a function of temperature for $\lambda = 0.05$. The dashed gray line represents an estimate of the wormhole transition temperature, when the Green's functions cross over from power law to exponential decay. For this value of λ, our numerical solution was unique at every chosen value of the temperature, save a couple of instances close to the transition, where it shows mild hysteresis. This is delineated in the right panel which shows the difference in free energy between the solutions obtained from annealing from high to low temperature (F_{H-L}), and low to high temperature (F_{L-H}), by using as an initial guess at each step the solution obtained at the previous step.

ward and downward in temperature, there is a hysteresis near the phase transition indicating that it is indeed first order. The hysteresis is small and not as sharp as in simpler models, but it is clearly there. It is supported by our observation that in our numerics the iterations take longer and longer to reach the convergence threshold for temperatures very close to the transition, as the system struggles to find the true ground state.[2]

We note that the YSYK TFD/wormhole solution can also be obtained alternatively in a smooth manner by starting from the nearly free fermion thermal state FF at large $\lambda \gg g^2/\omega_0^2$ but low $T \ll \lambda$ described above, and then reducing λ. No phase transition is seen. Instead the gap dependence on λ changes smoothly from $\gamma_{\lambda\gg} \sim \lambda + \ldots$ as in Fig.3.3 to $\gamma_{\lambda\ll} \sim \lambda^{\frac{1}{2-2\Delta_f}}$ exhibited in Fig. 3.5.

3.4. Inclusion of superconductivity: the BCS Josephson wormhole

We now probe whether this YSYK TFD/wormhole state survives the inclusion of superconductivity. To do so we turn on the possibility of a non-vanishing pair-condensate $\langle F \rangle \neq 0$ by setting $\alpha = 0$. For simplicity we shall first look at the specific model where the phase of $\lambda = |\lambda| e^{i\theta}$ is set to vanish: $\theta = 0$. In this case, both

[2] At very low temperatures and very small λ however, we find that the annealing in temperature is not sufficient as a numerical procedure to find the true ground state as the difference in free energy between the two distinct minima become smaller than the precision with which we can calculate our numerical solutions.

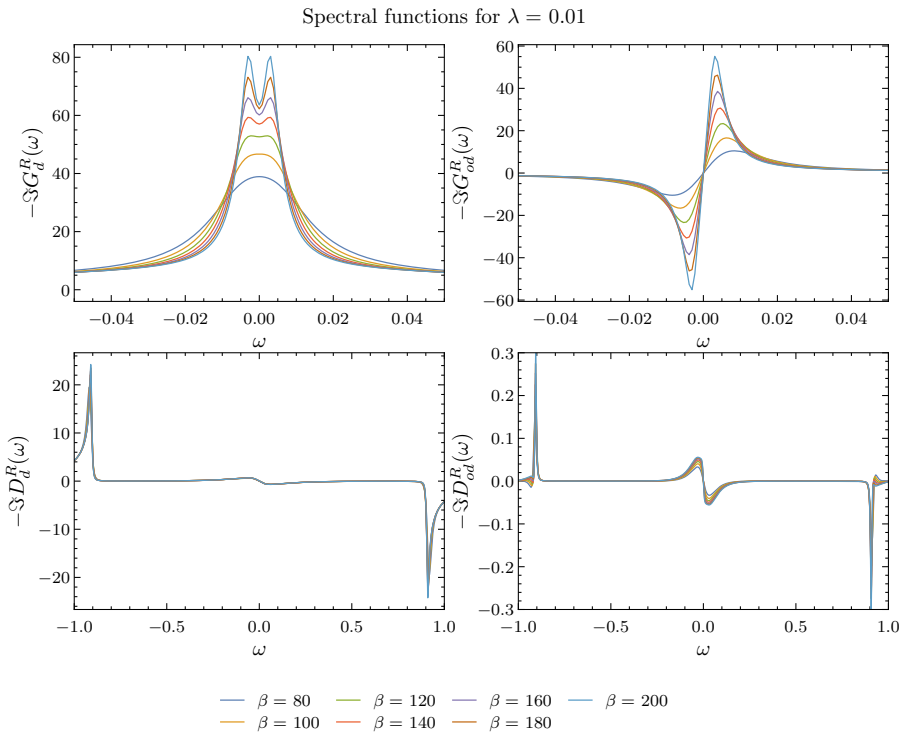

Figure 3.8: Temperature evolution various spectral functions in the model. The wormhole state is characterized by two symmetrically placed split peaks, but the black hole state is characterized by a smooth spectral function with the quantum critical form.

sides are identical to one another — there is an explicit mirror symmetry $c_1 \leftrightarrow c_2$ and the superconducting state will also be mirror symmetric under this symmetry. In a spatially extended system, this would correspond to the situation where the phases of the superconducting condensates in both of the subsystems are by construction aligned.

Fig. 3.9 shows the exact numerical solution to the saddle point equations now including the presence of the anomalous propagator terms F_d and F_{od}. For the parameters we studied we know based on the time-reversal symmetry breaking $\alpha = 1$ model roughly at which temperature to expect the transition to the TFD/wormhole state. We have *specifically* chosen parameters $g/\omega_0^{3/2} = 0.5$, such that this descent into superconductivity happens from the thermal quantum-critical state holographically dual to a BH (see Fig. 3.2). From the single sided YSYK model we also know that for these parameters this superconducting transition temperature is higher than the TFD/wormhole transition temperature: $T_c > T_{TFD}$. The question therefore is whether *after* the transition to superconductivity there is still a transition/crossover

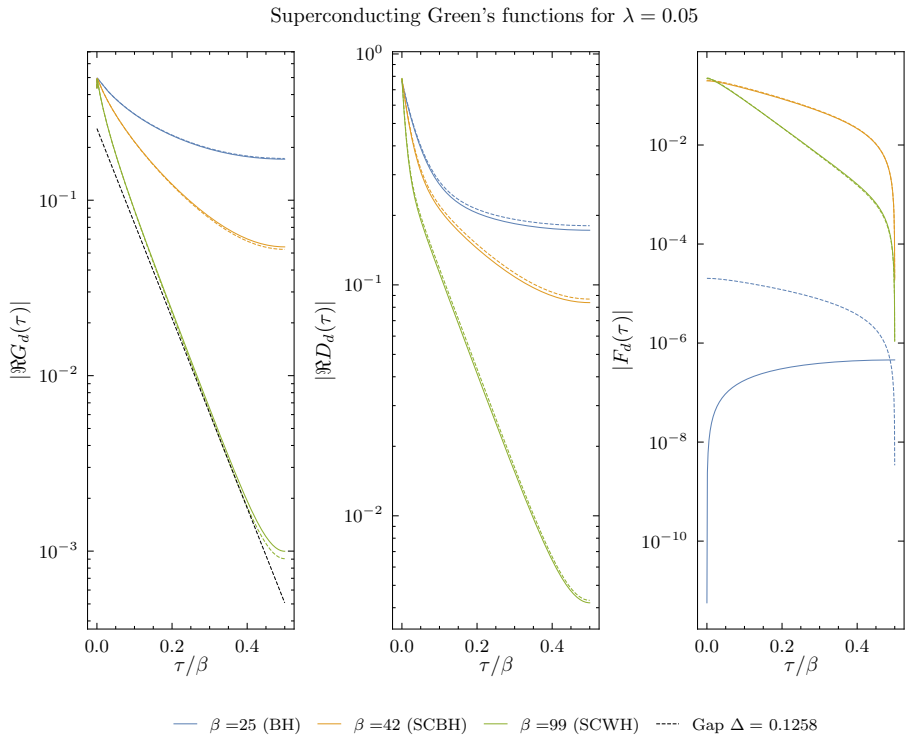

Figure 3.9: Superconducting solutions to the two sided model. The solid lines show the full solution to the two sided model, and the dashed line shows the numerical solution to the one sided model. The two are almost identical to one another.

to a TFD/wormhole like state as one lowers the temperature further.

The numerics indicate that this is so, but the identification is tenuous. The issue is that the superconducting state is also characterized by a gap in the single fermion spectral function G_d. So is the wormhole state, as we have shown. In neither case is this the single defining characteristic, but we can determine whether the robust spontaneous symmetry breaking gap, or the fragile remnant quantum criticality induced gap is the physics that the numerics shows. The full Green's functions in Fig. 3.9 show that the coupled YSYK system indeed first transitions to a superconducting state — the appearance of a non-vanishing order parameter $\Delta = \left|F_d(\tau = 0^+)\right|$ in the right column. At this time the asymptotic behavior is not yet recognizable as the exponential decay corresponding to a gap. This is so, because for the value $g/\omega_0^{3/2} = 0.5$ the gap develops BCS-like by opening up and is very weak for $T \lesssim T_c$ [24]. For $T \ll T_c$ one does clearly see a gap in the green curve in Fig. 3.9. This is also the regime where one would expect the TFD/wormhole gap to arise. The gap that is present is the ordinary BCS superconducting gap, however. This follows from

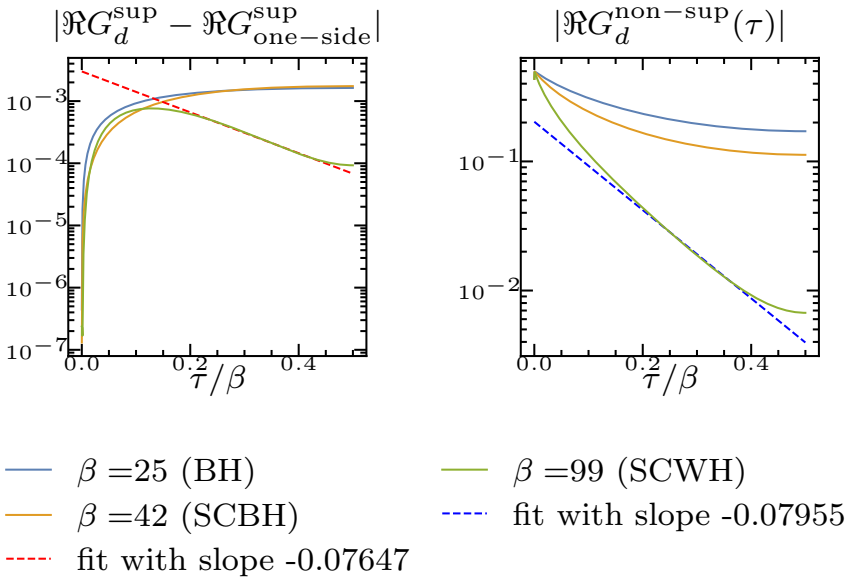

Figure 3.10: A remnant of the wormhole can be seen if one subtracts the one sided Green's functions from the diagonal Green's functions of the two sided tunneling coupled model.

a direct comparison with the result for a single sided YSYK model at the same parameters, but absent tunneling ($\lambda = 0$). Fig. 3.9 shows that the dominant exponential scaling is the same.

The indication that this is nevertheless also a TFD/wormhole state follows removing the contribution of the superconducting component. Taking the difference of the coupled YSYK model with the single-sided YSYK model with no tunneling shows that a distinct subleading exponential form remains in the single fermion response G_d of the coupled model; see Fig. 3.10. This residual exponential in the single fermion response can be compared with the leading exponential of the TFD/wormhole state in the absence of superconductivity. The exponent of the remnant exponential decay in the superconducting state is within 10% of that of the TFD/wormhole value. We can understand this through a simple Landau-Tisza two-fluid model. A fraction of fermions on the superconducting sector form pairs and enter the condensate. The other fermionic sector parallels the $\alpha = 1$ non superconducting TFD/wormhole state discussed in Sec. 3.3, and also holds some spectral weight, as is illustrated in Fig. 3.10.

Numerical accuracy prevents us from testing more firmly whether the superconducting state below $T < T_{\rm WH}$ is indeed a TFD/wormhole state built on a BCS-groundstate with higher excited states which should also follow the wormhole pat-

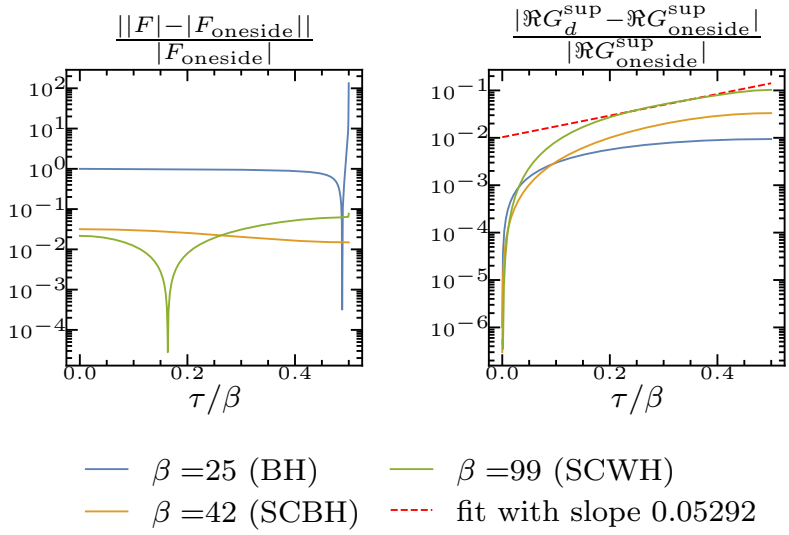

Figure 3.11: The anomalous propagators mostly just follow the one sided anomalous propagators, except for a small shift in magnitude. In the green curve, one sees a dip because the difference changes sign, and the absolute value is plotted on a log scale. The shift in magnitude is to be expected because in one case $\lambda \neq 0$, and this changes the magnitude of the solutions, but does not change the qualitative form.

tern. Our knowledge of ordinary BCS superconductors, however, supports that this only slightly changed first excited state can be taken as a convincing signature of the equivalent state of the TFD/wormhole state in the non-superconducting model.

The excitation spectrum above the BCS-groundstate does not contain any finite energy Cooper pair excitations. All low energy excitations are based on the (dressed, gapped) fermionic excitations in the theory. The TFD state of a BCS-like superconductor will therefore formally be very similar to the TFD state of a gapped fermion system without superconductivity.[3] This is indeed what our numerics shows, in that the single fermion Green's function of the coupled superconducting YSYK model are the made up of a weighted sum of the one-sided superconducting model and the two-sided non-superconducting YSYK model.

It is further supported by studying the anomalous Green's function $F_d(\tau)$. Here the subtraction of the single sided response leaves a remnant that simply follows $F(\tau)$ of the one sided model but with a much smaller magnitude - this just means that its

[3] Of course in a real superconductor this simplified picture does not hold completely. There are order parameter fluctuations supported by gradients. Such order parameter fluctuations can always be excited at finite temperature. Correspondingly a TFD state for these should exist. The SYK model is a quantum dot and there are no spatial gradients that can support a finite phase space of order parameter fluctuations. The simplified notion therefore does work here.

magnitude is shifted by a small constant, but with the function containing no additional structure. We also observe that the off-diagonal terms of the anomalous propagator $F_{od}(\tau)$ are numerically vanishingly small. The condensate sector is therefore completely equivalent between the single sided YSYK model and the tunneling coupled model, i.e. the condensing Cooper pairs are well formed separately on either side, and there is no cross-condensation or cross-excitation tunneling. In particular this means there are no (observable) excited states in the pairing channel, or any indication of pair-tunneling physics.

From the gravitational perspective it is perhaps surprising that certain excitations — single fermion — can traverse the wormhole and others — Cooper pairs — cannot. At this stage we have only shown the single fermion response function, and not the Cooper pair response function. This would correspond to a four-point function in terms of elementary fermionic excitations. In the large N limit in which we compute and which is the limit in which a dual gravitational description emerges, such a four-point function is suppressed at order $1/N$. Formally at the order we work there are no correlations whatsoever between Cooper pairs. This absence of correlations thus matches the microscopic YSYK perspective. At the same time it also indicates that a true answer whether the wormhole supports Cooper pair tunneling and revivals requires this four-point function computation. We leave this for future work.

From this microscopic viewpoint one would also expect Cooper pair tunneling and a Cooper pair TFD/wormhole state in a BEC like superconducting state where Cooper pairs can exist as uncondensed excitations. This regime exists in YSYK models for larger $g/\omega_0^{3/2} \sim 1$ identifiable by the fact that the superconducting gap fills as T increases, rather than closes [24]. The issue is that in this regime the metallic state is not the quantum critical groundstate gravitationally to a two-sided black hole. As revivals can arise for many different reasons and it is precisely the level spacing in the spectrum inherited from the quantum critical state that we use to identify the wormhole, it is not clear how we could identify a BEC-like superconducting TFD/wormhole.

At very large λ, we do not find any evidence of superconductivity, even down to the lowest temperatures that we can reach in our numerics. This can be understood because the metallic state in this case is a conventional gapped free fermion state at charge neutrality. There is no macroscopic density of states at zero energy; there is no density at all. There is no reservoir for Cooper pairs to form or condense.

3.5. A standard Josephson current

This observation that the TFD/wormhole state of the coupled model is built on a direct-product groundstate of two essentially independent condensates with no ob-

servable overlap suggests that its Josephson physics is standard. This is indeed the case. It is a well known trick in the conventional BCS Bogoliubov-deGennes formulation of Josephson physics that the external phase difference can be moved to the phase of the tunneling coupling λ (see e.g. [157]). This follows from the fact that a change of variables $c_2 \to c_2 e^{i\theta}$ can be compensated by a change in $\lambda \to \lambda e^{-i\theta}$. Thanks to the earlier mentioned mirror symmetry, this remains a solution to the saddle point equations, this change of variables will simply change the phase of the saddle-point solution of the second anomalous Green's function $F_{22} \to F_{22} e^{2i\theta}$ w.r.t. to the first anomalous Green's function. If the two superconductors are connected by a (metallic) ring-like configuration as well θ equals the magnetic flux through the loop in units of the superconducting flux quantum $\frac{h}{2e}$ (set to unity in our conventions). A sudden quench of $\lambda e^{i\theta} \to \lambda$ then sets up a configuration where the BCS condensate in the second system differs by a phase, but this is no longer the exact groundstate. The relaxation to the groundstate is the Josephson current.

The one difference between the YSYK model and the conventional BCS system is that the mean-field kinetic part of the action also has non-neglible contributions to the off-diagonal Green's functions. This is due to the strong coupling nature of the theory at low energies. These off-diagonal Green's functions must all be directly proportional to the tunneling coupling λ: They vanish when $\lambda = 0$. In the protocol to set up the Josephson configuration, these off-diagonal Green's functions must therefore instantaneously follow the quench that rotates the tunneling coupling. To clarify what we point out, recall that the Josephson Hamiltonian for two coupled conventional mean-field BCS system whose free energy gives the Josephson current is

$$H_{\text{BCS-BdG-Josephson}}(k) = \begin{pmatrix} c_{1\uparrow}^\dagger & c_{1\downarrow} & c_{2\uparrow}^\dagger & c_{2\downarrow} \end{pmatrix} \begin{pmatrix} \epsilon(k) & \Phi & \lambda & 0 \\ \Phi & -\epsilon(k) & 0 & -\lambda \\ \lambda^\dagger & 0 & \epsilon(k) & \Phi e^{-2i\theta} \\ 0 & -\lambda^\dagger & \Phi e^{2i\theta} & -\epsilon(k) \end{pmatrix} \begin{pmatrix} c_{1\uparrow} \\ c_{1\downarrow}^\dagger \\ c_{2\uparrow} \\ c_{2\downarrow}^\dagger \end{pmatrix}. \tag{3.18}$$

The Josephson configuration for the coupled YSYK system has for the kinetic part of the action following the insight that all off-diagonal Green's functions are slaved to the quench in $\lambda e^{i\theta} \to \lambda$.

$$S_f = -\ln\det \begin{pmatrix} i\omega_n - \Sigma_d & -\Phi_d & -\lambda - \Sigma_{\text{od}} & -\Phi_{\text{od}} \\ -\bar{\Phi}_{\text{d}} & i\omega_n - \tilde{\Sigma}_{\text{d}} & -\bar{\Phi}_{\text{od}} & \lambda - \tilde{\Sigma}_{\text{od}} \\ -\lambda - \Sigma_{\text{od}} & -\Phi_{\text{od}} & i\omega_n - \Sigma_d & -e^{2i\theta}\Phi_d \\ -\bar{\Phi}_{\text{od}} & \lambda - \tilde{\Sigma}_{\text{od}} & -e^{-2i\theta}\bar{\Phi}_{\text{d}} & i\omega_n - \tilde{\Sigma}_{\text{d}} \end{pmatrix} \tag{3.19}$$

The kinetic part of the action Eq.(3.19) is the only term in the full two sided action that depends on the Josephson phase. The other terms are explicitly gauge invariant, as is evident from inspecting Eq. (3.42). The phase dependence of the free energy can

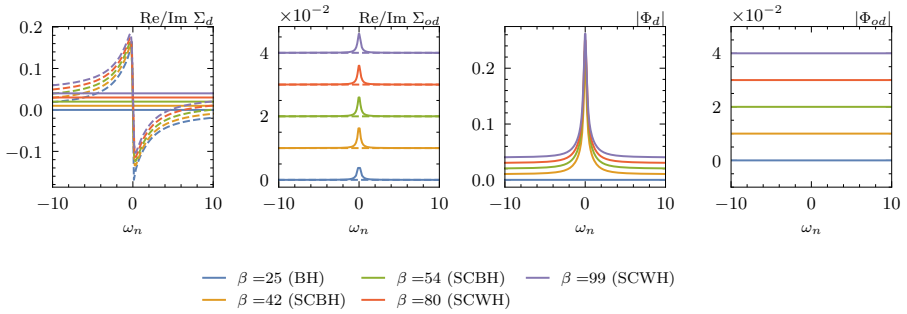

Figure 3.12: Magnitude of the various self energies in the superconducting state. In the first two panels, the solid lines indicate the real parts and the dotted lines indicate the imaginary parts. The different curves have been manually offset on the y-axis by 0.01 each, for ease of presentation.

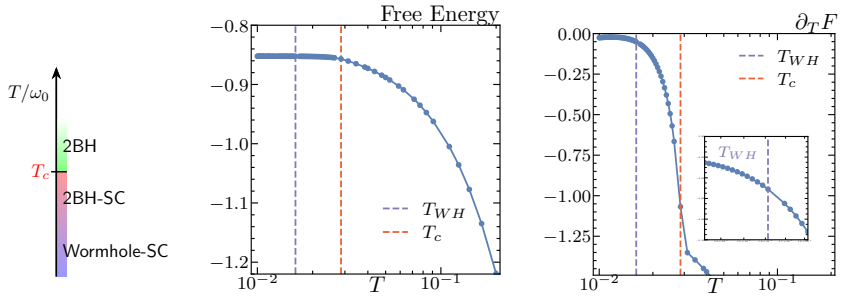

Figure 3.13: The schematic phase diagram of the coupled superconducting Yukawa-SYK system for $g/\omega_0^{3/2} = 0.5$ and $\alpha = 0$. The system first transitions to from the strongly coupled finite temperature critical state (2BH) to a superconducting state (2BH-SC) in a second order transition. While superconducting the system crosses over at an even lower T to a superconducting TFD/wormhole state. It is no longer a first order transition. The right shows that the free energy has a continuous derivative at the putative transition temperature $T_{\rm WH}$ - the inset is a zoom-in of the main panel near $T_{\rm WH}$.

therefore be written as

$$\mathscr{F} = -\frac{1}{\beta}\sum_{\omega_n} \ln\left(f_0(\Sigma,\lambda,\omega_n) + f_2(\Sigma,\lambda,\omega_n)\cos 2\theta + g_2(\Sigma,\lambda,\omega_n)\sin 2\theta\right), \tag{3.20}$$

with f_2 and g_2 just extracted from Eq.(3.19).

$$\begin{aligned} f_2 = \Phi_d^*\Big(&-\Sigma_{\rm od}\Phi_{\rm od}\Sigma_d^* + \Sigma_{\rm od}^*\left(2\Phi_d\Sigma_{\rm od} - \Sigma_d\Phi_{\rm od}\right) + 2\lambda^2\Phi_d - 2\lambda\Phi_{\rm od}\,{\rm Re}\left(\Sigma_d\right) + 4\lambda\Phi_d\,{\rm Re}\left(\Sigma_{\rm od}\right) \\ &+ 2i\omega\Phi_{\rm od}\,{\rm Re}\left(\Sigma_{\rm od}\right) - 2i\omega\Sigma_{\rm od}\Phi_{\rm od}\Big) \\ &- \Phi_d\Phi_{\rm od}^*\left(\Sigma_d\Sigma_{\rm od}^* + \Sigma_{\rm od}\left(\Sigma_d\right)^* + \Phi_d\Phi_{\rm od}^* * + 2\lambda\,{\rm Re}\left(\Sigma_d\right) + 2i\omega\left(\Sigma_{\rm od} - {\rm Re}\left(\Sigma_{\rm od}\right)\right)\right) - \Phi_{\rm od}^2\left(\Phi_d^*\right)^2, \end{aligned}$$

$$g_2 = i\left(\Phi_{\rm od}{\Phi_d}^* - \Phi_d\Phi_{\rm od}^*\right)\left(\Sigma_d\Sigma_{\rm od}^* + \Sigma_{\rm od}\Sigma_d^* + \Phi_d\Phi_{\rm od}^* + \Phi_{\rm od}\Phi_d^* + 2\lambda\,{\rm Re}\left(\Sigma_d\right) - 2\omega\,{\rm Im}(\Sigma_{\rm od})\right).$$

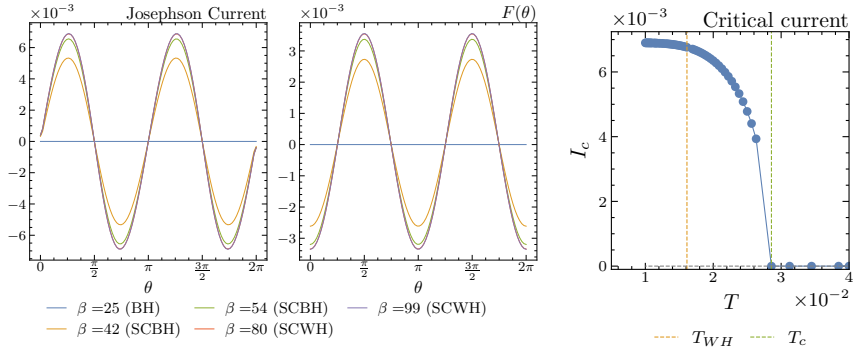

Figure 3.14: DC Josephson current as a function of the phase angle. It should be noted that in this figure, the angle on the x-axis is the phase that was introduced on the complex hopping parameter λ, and the physical phase difference between the left and the right superconducting order parameters is 2θ. In the right panel, we also show the temperature dependence of the critical current, which is a measurable physical quantity.

The term g_2 in the free energy is perhaps not familiar. However, it is generic if time-reversal symmetry is broken [158]. Our model preserves time-reversal, and explicit substitution shows that it vanishes as $\Phi_{od} = 0$ (Fig. 3.12. There is a tiny value of order 10^{-7} for $\Phi_{od}(0)$ which is numerical noise.)

We can further simplify f_2 by observing in Fig. 3.12 that the off diagonal self energy for the pairing Φ_{od} is vanishingly small (numerically several orders of magnitude smaller than the others). In that case, we can simply set $\Phi_{od} = 0$ in Eq. (3.20) to obtain

$$\mathscr{F} = -\frac{1}{\beta}\sum_{\omega_n} \ln\left(f_0(\Sigma,\lambda,\omega_n) + f_2(\Sigma,\lambda,\omega_n)\cos 2\theta\right), \tag{3.21}$$

with

$$f_2 = 2|\Phi_d|^2|\lambda + \Sigma_{od}|^2. \tag{3.22}$$

This formula does not assume weak coupling, and enables us to obtain a non-perturbative expression for the Josephson current, and we can see that Σ_{od} acts as a vertex correction to λ. Substituting in our previously calculated values for the various quantities, we can evaluate Eq. (3.20) and its derivative to calculate the Josephson current from the Josephson relation $I(\theta) = \partial_\theta \mathscr{F}$. The results are shown in Fig. 3.14.

3.6. Conclusion

It remains remarkable that the notion of holographic duality allows in principle the study of exotic (quantum)-gravitational phenomena through ordinary strongly coupled systems. The more difficult prerequisite is that such a system must also be

quantum critical. Those are not only rare, but often fragile and unstable. The most prominent instability is superconductivity. In this article, we have studied the coupled quantum critical Yukawa SYK model to understand how this instability might affect the exotic "wormhole" state that can exist in tunneling-coupled systems at low temperatures. This wormhole is the holographic gravitational description of a state that is very close to the thermo-field-double. The in-laboratory generation of the TFD-state is of its own interest to study entangled systems.

One clear qualitative way that the TFD/wormhole is visible is in the development of a gap in the single fermion spectrum. This is also one of the primary ways superconductivity manifests itself. The TFD gap inherits special properties from the quantum critical groundstate, whereas the superconducting gap is an ordinary robust BCS effect. With the notion that superconductivity usually wins from quantum criticality [148], the guess would be that there is no visible TFD/wormhole state in the coupled superconducting model. We have shown that this is only partly true. The superconducting groundstate of the coupled model is indeed indistinguishable from the uncoupled model. The Cooper pair condensate lives independently on either boundary, and there is no Cooper tunneling visible in "Wormhole" revival in the fermionic or bosonic Green's function. Direct Cooper pair tunneling could be expected in a four point function, but this is formally suppressed in the large N-limit in which the gravitational dual description is appropriate. Nevertheless, we find that the wormhole state still lives on as a subleading effect even in the superconducting state at temperatures when the metallic state would have transitioned to the TFD/wormhole state: We see a remnant exponential of the same decay constant as the metallic state at that temperature when the superconducting component corresponding to the single side model is subtracted out.

Since the coupling term in the action is identical to the electron tunneling in metals and superconductors, we use this model to non-perturbatively (in the cross coupling) calculate the Josephson current in the superconducting phase, and we find that it is quite ordinary. The temperature dependence of the critical current is completely smooth at the temperature in which the normal state transitions to the wormhole/TFD state. We conjecture that the superconductivity only lives separately on the two sides owing to the fact that for the configuration we study the Cooper pairs are composite particles which as in BCS theory immediately break apart on excitation in the weak coupling superconducting phase, and are hence unable to be put into a TFD state. At strong coupling, however, the one-sided Yukawa SYK model shows a BEC-like gap filling [24]. This means Cooper pairs exist in the spectrum as uncondensed bound states which should be partially occupied at finite temperature. It therefore has the required ingredients for forming a TFD state of Cooper pairs. The challenge there is that for these strong coupling parameters at finite temperature above T_c, the normal state is not described by a thermal quantum critical state dual to a black hole,

but by an impurity-like fixed point, which is not holographically dual to any known geometry. It is therefore not clear whether the TFD state which ought to exist fulfills the conditions to be also seen as a macroscopic semi-classical wormhole state. We leave this as an open question for future study.

Acknowledgements

We thank L. Barbera, C. Beenakker, V. Cheianov, N. Doerfler, I. Jang and J. Schmalian for discussions, and especially D. Valentinis and N. Chagnet both for discussions and help with the numerics. This research was supported in part by the Dutch Research Council (NWO) project 680-91-116 (*Planckian Dissipation and Quantum Thermalisation: From Black Hole Answers to Strange Metal Questions.*), and by the Dutch Research Council/Ministry of Education. The numerical computations were carried out in part on the ALICE-cluster of Leiden University. We are grateful for their help.

3.7. Appendix

3.7.1. Derivation of the effective action

Starting from the bare action, we will obtain the disorder averaged theory by performing the average over the couplings g_{ijk}. As discussed in the main text, we are interested in both the TRS broken (GUE) and TRS preserving (GOE) states to study the metallic and superconducting states respectively. We will thus interpolate between the two with the α parameter, which can be thought of as a pair breaking term in the superconducting state. To a certain extent, this parameter can also be used to tune the superconducting transition temperature, details of which are discussed at length in [27]. We will use the following lemma to do the disorder average in the α interpolating ensemble (for Hermitian $O_{ijk} = O^{\dagger}_{jik}$, as the case is here)

$$\overline{e^{-\sum_{ijk} g_{ijk} O_{ijk}}} = \exp\left\{ -\sum_{ijk} \left[-\frac{1}{4}(1-\frac{\alpha}{2})\bar{g}^2 \left(O_{ijk} + O^{\dagger}_{ijk} \right)^2 + \frac{1}{4}(\frac{\alpha}{2})\bar{g}^2 \left(O_{ijk} - O^{\dagger}_{ijk} \right)^2 \right] \right\}, \tag{3.23}$$

$\alpha = 0$ is the GOE and $\alpha = 1$ is the GUE. The required terms in Eq. (3.23) for our model are

$$\left(O_{ijk} \pm O^{\dagger}_{ijk} \right)^2 = \sum_{a,b} \sum_{\sigma\sigma'} \int d\tau \int d\tau' \phi^{(a)}_k(\tau) \phi^{(b)}_k(\tau') \left[c^{\dagger (a)}_{i\sigma}(\tau) c^{(a)}_{j\sigma}(\tau) \pm c^{\dagger (a)}_{j\sigma}(\tau) c^{(a)}_{i\sigma}(\tau) \right] \left[c^{\dagger (b)}_{i\sigma'}(\tau') c^{(b)}_{j\sigma'}(\tau') \pm c^{\dagger (b)}_{j\sigma'}(\tau') c^{(b)}_{i\sigma'}(\tau') \right]. \tag{3.24}$$

At this point, the following insertions of identity can be used to formally rewrite the action in terms of the collective $G-\Sigma$ variables [34, 159]

$$\mathbb{1} = \int \mathscr{D}G \mathscr{D}\Sigma \, e^{-\left[-N G^{ba}_{\sigma'\sigma}(\tau',\tau) + \sum_i c^{\dagger (a)}_{i\sigma}(\tau) c^{(b)}_{i\sigma'}(\tau') \right] \Sigma^{ab}_{\sigma\sigma'}(\tau,\tau')}, \tag{3.25a}$$

$$\mathbb{1} = \int \mathscr{D}F \mathscr{D}\bar{\Phi} \, e^{-\frac{1}{2}\left[-N F^{ba}_{\sigma'\sigma}(\tau',\tau) + \sum_i c^{(a)}_{i\sigma}(\tau) c^{(b)}_{i\sigma'}(\tau') \right] \bar{\Phi}^{ab}_{\sigma\sigma'}(\tau,\tau')}, \tag{3.25b}$$

$$\mathbb{1} = \int \mathscr{D}\bar{F} \mathscr{D}\Phi \, e^{-\frac{1}{2}\left[-N \bar{F}^{ba}_{\sigma'\sigma}(\tau',\tau) + \sum_i c^{\dagger (a)}_{i\sigma}(\tau) c^{\dagger (b)}_{i\sigma'}(\tau') \right] \Phi^{ab}_{\sigma\sigma'}(\tau,\tau')}, \tag{3.25c}$$

$$\mathbb{1} = \int \mathscr{D}D \mathscr{D}\Pi \, e^{-\frac{1}{2}\left[M D^{ba}(\tau',\tau) - \sum_k \phi^{(a)}_k(\tau) \phi^{(b)}_k(\tau') \right] \Pi^{ab}(\tau,\tau')}. \tag{3.25d}$$

We can write the interaction part of the action

$$\overline{S}_g = \frac{M g^2}{2} \sum_{ab} \sum_{\sigma,\sigma'} \int d\tau \int d\tau' D^{ab}(\tau,\tau') \left[G^{ab}_{\sigma\sigma'}(\tau,\tau') G^{ba}_{\sigma'\sigma}(\tau',\tau) + (1-\alpha) \bar{F}^{ab}_{\sigma\sigma'}(\tau,\tau') F^{ab}_{\sigma\sigma'}(\tau,\tau') \right] \tag{3.26}$$

This effective action is now quadratic in the boson and fermion terms, and they can now be integrated out to give

$$\begin{aligned}
S = \int d\tau d\tau' \sum_i \sum_{\sigma,\sigma'} \sum_{ab} c^{\dagger(a)}_{i\sigma}(\tau) \Big[(\partial_\tau - \mu)\delta_{ab}\delta_{\sigma\sigma'}\delta(\tau-\tau') + \Sigma^{ab}_{\sigma\sigma'}(\tau,\tau') \Big] c^{(b)}_{i\sigma'}(\tau') \\
+ \frac{1}{2} c^{(a)}_{i\sigma}(\tau) \bar{\Phi}^{ab}_{\sigma\sigma'}(\tau,\tau') c^{(b)}_{i\sigma'}(\tau') + \frac{1}{2} c^{\dagger(a)}_{i\sigma}(\tau) \Phi^{ab}_{\sigma\sigma'}(\tau,\tau') c^{\dagger(b)}_{i\sigma'}(\tau') \\
+ \frac{1}{2}\phi^{(a)}_k(\tau) \Big[(-\partial_\tau^2 + \omega_0^2)\delta_{ab}\delta(\tau-\tau') - \Pi^{ab}(\tau,\tau') \Big] \phi^{(b)}_k(\tau') - NG^{ba}_{\sigma'\sigma}(\tau',\tau)\Sigma^{ab}_{\sigma\sigma'}(\tau,\tau') \\
- \frac{N}{2} F^{ba}_{\sigma'\sigma}(\tau',\tau)\bar{\Phi}^{ab}_{\sigma\sigma'}(\tau,\tau') - \frac{N}{2}\bar{F}^{ba}_{\sigma'\sigma}(\tau',\tau)\Phi^{ab}_{\sigma\sigma'}(\tau,\tau') + \frac{M}{2} D^{ba}(\tau',\tau)\Pi^{ab}(\tau,\tau') \\
+ \frac{Mg^2}{2} D^{ab}(\tau,\tau') \Big[G^{ab}_{\sigma\sigma'}(\tau,\tau')G^{ba}_{\sigma'\sigma}(\tau',\tau) + (1-\alpha)\bar{F}^{ab}_{\sigma\sigma'}(\tau,\tau')F^{ab}_{\sigma\sigma'}(\tau,\tau') \Big] . \qquad (3.27)
\end{aligned}$$

At this point, we can perform the sum over the spin indices by imposing spin symmetry and simultaneously putting to zero all terms that do not appear in a form consistent with singlet pairing.

$$F^{ab}_{\uparrow\downarrow}(\tau,\tau') = F^{ab}(\tau,\tau') \qquad (3.28a)$$
$$F^{ab}_{\downarrow\uparrow}(\tau,\tau') = -F^{ba}(\tau',\tau) \qquad (3.28b)$$
$$\bar{F}^{ab}_{\downarrow\uparrow}(\tau,\tau') = \bar{F}^{ab}(\tau,\tau') \qquad (3.28c)$$
$$\bar{F}^{ab}_{\uparrow\downarrow}(\tau,\tau') = -\bar{F}^{ba}(\tau',\tau) \qquad (3.28d)$$

We illustrate this with the example of the Lagrange multiplier term (3.25b), and it follows similarly for the rest.

$$\begin{aligned}
S \supset \frac{1}{2}\int d\tau d\tau' \sum_{\sigma,\sigma'}\sum_{ab} \bar{\Phi}^{ab}_{\sigma\sigma'}(\tau,\tau') \left[-NF^{ba}_{\sigma'\sigma}(\tau',\tau) + \sum_i c^{(a)}_{i\sigma}(\tau) c^{(b)}_{i\sigma'}(\tau') \right] , \\
= \frac{1}{2}\int d\tau d\tau' \sum_{ab} \bar{\Phi}^{ab}_{\downarrow\uparrow}(\tau,\tau') \left[-NF^{ba}_{\uparrow\downarrow}(\tau',\tau) + \sum_i c^{(a)}_{i\downarrow}(\tau) c^{(b)}_{i\uparrow}(\tau') \right] + \\
\bar{\Phi}^{ba}_{\uparrow\downarrow}(\tau',\tau) \left[-NF^{ab}_{\downarrow\uparrow}(\tau,\tau') - \sum_i c^{(a)}_{i\downarrow}(\tau) c^{(b)}_{i\uparrow}(\tau') \right] \qquad (3.29)
\end{aligned}$$

We can use the definitions Eqs. (3.28) and also define a new function for a singlet form of the $\bar{\Phi}$ field

$$\bar{\Phi}^{ab}(\tau,\tau') = \frac{\bar{\Phi}^{ab}_{\downarrow\uparrow}(\tau,\tau') - \bar{\Phi}^{ba}_{\uparrow\downarrow}(\tau',\tau)}{2}, \qquad (3.30)$$

to obtain

$$S^{\bar{\Phi},F}_{LM} = \int d\tau d\tau' \sum_{ab} \bar{\Phi}^{ab}(\tau,\tau') \left[-NF^{ba}(\tau',\tau) + \sum_i c^{(a)}_{i\downarrow}(\tau) c^{(b)}_{i\uparrow}(\tau') \right] \qquad (3.31)$$

Likewise, we can also obtain for the $\Phi, \bar{F}$ terms using the definition

$$\Phi^{ab}(\tau,\tau') = \frac{\Phi^{ab}_{\uparrow\downarrow}(\tau,\tau') - \Phi^{ba}_{\downarrow\uparrow}(\tau',\tau)}{2} \tag{3.32}$$

to get

$$S^{\Phi,\bar{F}}_{LM} = \int d\tau d\tau' \sum_{ab} \Phi^{ab}(\tau,\tau') \left[-N\bar{F}^{ba}(\tau',\tau) + \sum_i c^{\dagger(a)}_{i\uparrow}(\tau) c^{\dagger(b)}_{i\downarrow}(\tau') \right] \tag{3.33}$$

The relationship between F and $\bar{F}$ is as follows. For Grassmann numbers, $(\theta_1\theta_2)^* = \theta_2^*\theta_1^*$, where * denotes complex conjugation. On the saddle point, one can take the complex conjugate of Eq. (3.31) and match it to the constraint given by Eq. (3.33) to get

$$\left(F^{ab}(\tau,\tau')\right)^* = \bar{F}^{ba}(\tau',\tau) \tag{3.34a}$$

$$\left(\Phi^{ab}(\tau,\tau')\right)^* = \bar{\Phi}^{ba}(\tau',\tau) \tag{3.34b}$$

One can also note that Eq. (3.34a) for matsubara frequencies implies

$$\left(F^{ab}(i\omega_n)\right)^* = \bar{F}^{ba}(i\omega_n) \tag{3.35}$$

For the Lagrange multiplier terms that contain the electron and hole propagators,

$$\begin{aligned} S^{G,\Sigma}_{LM} = \int d\tau d\tau' \sum_{ab} \Big[& \Sigma^{ab}_{\uparrow\uparrow}(\tau,\tau') \left(-NG^{ba}_{\uparrow\uparrow}(\tau',\tau) + \sum_i c^{\dagger(a)}_{i\uparrow}(\tau) c^{(b)}_{i\uparrow}(\tau') \right) \\ & + (-\Sigma^{ba}_{\downarrow\downarrow}(\tau',\tau)) \left(NG^{ab}_{\downarrow\downarrow}(\tau,\tau') + \sum_i c^{(a)}_{i\downarrow}(\tau) c^{\dagger(b)}_{i\downarrow}(\tau') \right) \Big], \end{aligned} \tag{3.36}$$

$$\begin{aligned} = \int d\tau d\tau' \sum_{ab} \Big[& \Sigma^{ab}(\tau,\tau') \left(-NG^{ba}(\tau',\tau) + \sum_i c^{\dagger(a)}_{i\uparrow}(\tau) c^{(b)}_{i\uparrow}(\tau') \right) \\ & + \tilde{\Sigma}^{ab}(\tau',\tau) \left(-N\tilde{G}^{ba}(\tau',\tau) + \sum_i c^{(a)}_{i\downarrow}(\tau) c^{\dagger(b)}_{i\downarrow}(\tau') \right) \Big]. \end{aligned} \tag{3.37}$$

Spin symmetry at the saddle point in this case is the requirement that $G^{ba}_{\uparrow\uparrow}(\tau',\tau) = G^{ba}_{\downarrow\downarrow}(\tau',\tau)$. This can be naturally imposed by the same Lagrange multiplier constraint in Eq. (3.37) if we pick on the saddle point

$$\tilde{G}^{ba}(\tau',\tau) = -G^{ab}(\tau,\tau') \tag{3.38}$$

$$\tilde{\Sigma}^{ab}(\tau,\tau') = -\Sigma^{ba}(\tau',\tau). \tag{3.39}$$

If we assume $G^{ab}(\tau)$ and $D^{ab}(\tau)$ to be real, then this implies that $\Sigma^{ab}(\tau)$ will also be real on the saddle point, and then we can write

$$\tilde{\Sigma}(i\omega_n) = -\Sigma^*(i\omega_n). \tag{3.40}$$

The sum over spins can also be performed in the disorder averaged interaction term above, and we get

$$\overline{S}_g = \frac{Mg^2}{2}\sum_{ab}\int d\tau d\tau' D^{ab}(\tau,\tau')\Big[G^{ab}(\tau,\tau')G^{ba}(\tau',\tau)+\tilde{G}^{ab}(\tau,\tau')\tilde{G}^{ba}(\tau',\tau) - 2(1-\alpha)\bar{F}^{ba}(\tau',\tau)F^{ab}(\tau,\tau')\Big]. \quad (3.41)$$

We are then left with the

$$\begin{aligned}\frac{S}{N} &= -\ln\det\left\{\hat{G_0}^{-1}-\hat{\lambda}-\hat{\Sigma}\right\}+\frac{\kappa}{2}\ln\det\left\{\hat{D_0}^{-1}-\hat{\Pi}\right\}\\ &+\frac{\kappa g^2}{2}\int d\tau d\tau'\sum_{ab}D^{ab}(\tau,\tau')\left[G^{ab}(\tau,\tau')G^{ba}(\tau',\tau)+\tilde{G}^{ab}(\tau,\tau')\tilde{G}^{ba}(\tau',\tau)-2(1-\alpha)\bar{F}^{ab}(\tau,\tau')F^{ba}(\tau',\tau)\right]\\ &-\int d\tau d\tau'\sum_{ab}\left[G^{ba}(\tau',\tau)\Sigma^{ab}(\tau,\tau')+\tilde{G}^{ba}(\tau',\tau)\tilde{\Sigma}^{ab}(\tau,\tau')+F^{ba}(\tau',\tau)\bar{\Phi}^{ab}(\tau,\tau')+\bar{F}^{ba}(\tau',\tau)\Phi^{ab}(\tau,\tau')\right]\\ &+\frac{\kappa}{2}\int d\tau d\tau'\sum_{ab}D^{ba}(\tau',\tau)\Pi^{ab}(\tau,\tau'). \quad (3.42)\end{aligned}$$

The trace-log term is just spelled out for completeness as

$$\begin{aligned}S^f &= \sum_{\omega_n}-\ln\det\hat{K},\\ \hat{K}(i\omega_n) &= \begin{pmatrix} i\omega_n-\Sigma_{11} & -\Phi_{11} & -\lambda-\Sigma_{12} & -\Phi_{12}\\ -\bar{\Phi}_{11} & i\omega_n-\bar{\Sigma}_{11} & -\bar{\Phi}_{12} & \lambda^*-\bar{\Sigma}_{12}\\ -\lambda^*-\Sigma_{21} & -\Phi_{21} & i\omega_n-\Sigma_{22} & -\Phi_{22}\\ -\bar{\Phi}_{21} & \lambda-\bar{\Sigma}_{21} & -\bar{\Phi}_{22} & i\omega_n-\bar{\Sigma}_{22}\end{pmatrix}. \quad (3.43)\end{aligned}$$

The Euler-Lagrange equations for varying the action with the self energy variables are calculated using the trace-log identity

$$\begin{aligned}\delta(\mathrm{tr}\ln M) &= \mathrm{tr}\left(M^{-1}\delta M\right)\\ &= M^{-1}_{\alpha\beta}\delta M_{\beta\alpha}\\ \implies \frac{\delta\,\mathrm{tr}\ln M}{\delta M_{\beta\alpha}} &= \left[M^{-1}\right]_{\alpha\beta}. \quad (3.44)\end{aligned}$$

to arrive at the Schwinger-Dyson equations in the main text.

3.7.2. Conformal limit of the one sided Schwinger-Dyson equations

The Schwinger-Dyson equations in this case are the limit of $\lambda = 0$, and are the replica diagonal solutions to the action in Eq. (3.42). They are simply written as

$$\Sigma(\tau) = \kappa\, g^2\, G(\tau) D(\tau) \tag{3.45a}$$

$$\Pi(\tau) = = -2g^2\, G(\tau) G(-\tau) \tag{3.45b}$$

$$G(i\omega_n) = \frac{1}{i\omega_n - \Sigma(i\omega_n)} \tag{3.45c}$$

$$D(i\nu_n) = \frac{1}{\nu_n^2 + \omega_0^2 - \Pi(i\nu_n)}. \tag{3.45d}$$

The model is self-tuning to criticality [24], i.e the boson modes soften in the infrared. This is the condition that at zero temperature, $\Pi(\omega = 0) = \omega_0^2$. The Dyson equation in the fully conformal limit, where the self energy wins over the free propagators are

$$-1 = G(\omega)\Sigma(\omega)\,, \tag{3.46a}$$

$$-1 = D(\omega)\Pi(\omega). \tag{3.46b}$$

In the infrared, they can be solved with the zero-temperature conformal ansatz

$$G(\tau) = b\frac{\mathrm{sgn}(\tau)}{|\tau|^{2\Delta_f}}, \tag{3.47}$$

$$D(\tau) = d\frac{1}{|\tau|^{2\Delta_b}}. \tag{3.48}$$

These can be Fourier transformed using the identities

$$\int_{-\infty}^{\infty} d\tau\, \frac{\mathrm{sgn}(\tau)}{|\tau|^{\alpha}} e^{i\omega\tau} = i2^{1-\alpha}\sqrt{\pi}\frac{\Gamma(1-\frac{\alpha}{2})}{\Gamma(\frac{1}{2}+\frac{\alpha}{2})}|\omega|^{\alpha-1}\,\mathrm{sgn}(\omega), \tag{3.49}$$

$$\int_{-\infty}^{\infty} d\tau\, \frac{1}{|\tau|^{\alpha}} e^{i\omega\tau} = 2^{1-\alpha}\sqrt{\pi}\frac{\Gamma(\frac{1}{2}-\frac{\alpha}{2})}{\Gamma(\frac{\alpha}{2})}|\omega|^{\alpha-1}. \tag{3.50}$$

We then get

$$\Sigma(\omega) = \kappa\, g^2 b d\, i2^{1-2(\Delta_f+\Delta_b)}\sqrt{\pi}\frac{\Gamma(1-(\Delta_f+\Delta_b))}{\Gamma(\frac{1}{2}+\Delta_f+\Delta_b)}|\omega|^{2(\Delta_f+\Delta_b)-1}\,\mathrm{sgn}(\omega) \tag{3.51a}$$

$$\Pi(\omega) = 2g^2 b^2\, 2^{1-4\Delta_f}\sqrt{\pi}\frac{\Gamma(\frac{1}{2}-2\Delta_f)}{\Gamma(2\Delta_f)}|\omega|^{4\Delta_f-1} \tag{3.51b}$$

$$G(\omega) = b\, i2^{1-2\Delta_f}\sqrt{\pi}\frac{\Gamma(1-\Delta_f)}{\Gamma(\frac{1}{2}+\Delta_f)}|\omega|^{2\Delta_f-1}\,\mathrm{sgn}(\omega) \tag{3.51c}$$

$$D(\omega) = d\, 2^{1-2\Delta_b}\sqrt{\pi}\frac{\Gamma(\frac{1}{2}-\Delta_b)}{\Gamma(\Delta_b)}|\omega|^{2\Delta_b-1} \tag{3.51d}$$

Eqs. (3.51) and (3.46) together imply that

$$2\Delta_f + \Delta_b = 1, \tag{3.52}$$

$$\kappa \frac{\Gamma(1-\Delta_f)\Gamma(1-(\Delta_f+\Delta_b))}{\Gamma(\frac{1}{2}+\Delta_f)\Gamma(\frac{1}{2}+\Delta_f+\Delta_b)} = -2\frac{\Gamma(\frac{1}{2}-\Delta_b)\Gamma(\frac{1}{2}-2\Delta_f)}{\Gamma(\Delta_b)\Gamma(2\Delta_f)}. \tag{3.53}$$

For $\kappa = 1$, these equations are solved by $\Delta_f = 0.420374$, and $\Delta_b = 0.159252$, and for $\kappa = 10$, these are solved by $\Delta_f = 0.193052$, and $\Delta_b = 0.613896$.

3.7.3. Numerical details

In order to obtain the wormhole solution at low temperatures, it was essential to pick a good starting ansatz for the iterative procedure. For this purpose, we started with the large λ free fermion solution, and implemented an annealing procedure by successively solving the Schwinger-Dyson equations for lower and lower values of λ by using the immediately previous solution as a seed. In order to stabilize the iteration procedure, it was also essential to mix in some of the Green's functions at each previous step as is standard in literature as

$$G_d^{i+1}(\omega) = x\,\hat{T}G_d^i(i\omega_n) + (1-x)G_d^i(\omega_n) \tag{3.54}$$

and similarly for the rest, where $\hat{T}$ represents the operator corresponding to one iteration step

$$\hat{T}G_d^i = \frac{i\omega_n - \Sigma_d^i}{(i\omega_n - \Sigma_d)^2 - (\lambda + \Sigma_{od}^i)^2}. \tag{3.55}$$

The Σ^i refer to the self energies calculated using the G^i. We keep repeating this iteration process until the two norm between the Green's functions calculated in successive iterations is smaller than an error threshold ϵ_{th}. We use a constant mixing parameter $x = 0.01$. Since the difference between successive steps itself depends on what x is chosen, the renormalized threshold $\frac{\epsilon_{th}}{x^2}$ must be chosen small in comparison to 1. This can be easily seen in the following way.

$$\begin{aligned}\left\| G^{i+1} - G^i \right\| &= \left\| x\,\hat{T}G^i + (1-x)G^i - G^i \right\| \\ &= x^2 \left\| \hat{T}G^i - G^i \right\|,\end{aligned} \tag{3.56}$$

and the criterion that we need for convergence to be achieved is that $\left\| \hat{T}G^i - G^i \right\| \ll 1$.

In the numerics unless otherwise specified, we always work in units where the boson mass ω_0^2 is set to 1. Additionally, in all calculations, the Yukawa SYK coupling g was set to 0.5.

4

Kondo effect in Twisted Bilayer graphene

Attribution

This paper has been previously published in Physical Review B, under the title ***Kondo effect in twisted bilayer graphene***, together with Dmytro O. Oriekhov, Andrew K. Mitchell and Lars Fritz [106].

Abstract

The emergence of flat bands in twisted bilayer graphene at the magic angle can be understood in terms of a vanishing Fermi velocity of the Dirac cone. This is associated with van Hove singularities approaching the Fermi energy and becoming higher-order. In the density of states this is reflected by flanking logarithmic van Hove divergences pinching off the central Dirac cone in energy space. The low-energy pseudogap of the Dirac cone away from the magic angle is replaced by a power-law divergence due to the higher-order van Hove singularity at the magic angle. This plays an important role in the exotic phenomena observed in this material, such as superconductivity and magnetism, by amplifying electronic correlation effects. Here we investigate one such correlation effect – the Kondo effect due to a magnetic impurity embedded in twisted bilayer graphene. We use the Bistritzer-MacDonald model to extract the low-energy density of states of the material as a function of twist angle, and study the resulting quantum impurity physics using per-

turbative and numerical renormalization group methods. Although at zero temperature the impurity is only Kondo screened precisely at the magic angle, we find highly nontrivial behavior at finite temperatures relevant to experiment, due to the complex interplay between Dirac, van Hove, and Kondo physics.

4.1. Introduction

The properties of two-dimensional monolayer systems are strongly modified by stacking two layers with a relative twist, the so-called moiré effect in twisted bilayer systems [160]. In particular, twisted bilayer graphene (TBG) exhibits peculiar properties at specific 'magic' twist angles [83, 92, 93, 103, 161–166]. One characteristic of the system at these magic angles is that the non-interacting band structure contains almost-flat bands. This leads to a dramatic enhancement of the density of states (DoS). Consequently, electronic interaction effects are boosted, favoring the appearance of magnetism and other correlated phases, for example superconductivity [92, 93, 166–176]. Away from the magic angle in TBG, the slightly modified Dirac cones of the single layers persist [160], giving a low-energy linear pseudogap DoS. However, pronounced van Hove singularities [177] (vHs's) dominate the band structure at higher energies, leading to logarithmic divergences in the DoS. Experimentally, it was recently shown [178] that as the magic angle is approached, the vHs divergences in the DoS move to lower energy, pinching off the Dirac cone from either side in energy space. At the magic angle, the vHs divergences in the DoS merge, and a single higher-order vHs [83] (HO-vHs) emerges, yielding a stronger, power-law divergent DoS. This is a characteristic feature of the emergent flat bands in this system. The enhanced effect of electron correlations due to the HO-vHs in the bulk TBG material has been studied theoretically [93, 101, 166, 168] and confirmed in scanning tunnelling spectroscopy (STS) experiments [179, 180].

Detailed information on the electronic structure of new materials can also be obtained by exploiting defects or impurities as *in-situ* probes [181]. The nature of the electronic scattering from impurities in a system is strongly dependent on the band structure and DoS of the clean host material, and can be probed either locally at the impurity site by STS [182, 183], or by collecting momentum-space information through quasiparticle interference (QPI) measurements [184]. For quantum impurities such as magnetic adatoms [185, 186] or single-molecule magnets [187], the impurity spin degree of freedom generates additional spin-flip scattering, which is boosted at low temperatures by the Kondo effect in standard metallic hosts [188]. The Kondo effect itself depends sensitively on the local spin-resolved DoS of the host material, and hence such 'Kondo probes' can provide additional electronic structure information [189, 190] or be utilized for quantum metrology [191]. Aside from the spectroscopic and QPI signatures of Kondo physics in metals [186], the Kondo effect

has been studied in a range of other unconventional materials, including monolayer graphene [192–195], topological insulators [196], Dirac and Weyl semimetals [197], ferromagnets [198, 199], superconductors [200, 201], and spin liquids [202–204] – each giving its own distinctive response. In particular, for Dirac systems with a low-energy pseudogap, the depleted conduction electron DoS is known to suppress the Kondo effect [194, 196, 197] (although it can be revived upon doping [205]).

By contrast, in the case of TBG, one might expect Kondo correlations to be strongly enhanced by the flat bands and diverging DoS close to the magic angle. The study of Kondo physics in TBG, and how it evolves with twist angle, is the topic of this article. We find that magnetic impurities are sensitive probes of the nontrivial band structure of the material, and we uncover rich thermodynamic and spectroscopic signatures that rapidly change on approaching the magic angle.

Specifically, we consider a single, interacting Anderson impurity embedded in the TBG host – see Fig. 4.1a. The clean TBG material is modelled using the Bistritzer-MacDonald (BM) model [103], which we discuss in Sec. 4.2. We focus on the role of the vHs's and their evolution with twist angle. The model shows an intricate interplay between different DoS elements: metallic, Dirac pseudogap, vHs log-divergence, and HO-vHs power-law divergence. In Sec. 4.3 we review the physics of the Kondo model, emphasizing the different limiting behaviors arising in the metallic, pseudogap, and log-diverging or power-law diverging DoS needed to understand the compound DoS structure in TBG. Finally, in Sec. 4.4 we present full numerical renormalization group (NRG) results for an Anderson impurity in TBG in the vicinity of, and at, the magic angle. We focus on thermodynamic quantities such as the impurity entropy as a clear means of identifying the different fixed points and emergent energy scales. We furthermore study the energy-dependence of the local impurity spectral function, which is relevant to STS experiments. We conclude in Sec. 4.5, commenting on the suitability of magnetic impurities as *in-situ* probes for the physics of TBG near the magic angle, and an outlook for experiments. Technical material is given for reference in the Appendices.

We note that the Kondo model we consider in this work is completely different from recent studies of TBG as a heavy fermion problem [206–209], where the quenched kinetic energy of the flat band lends itself to being treated as an immobile lattice of impurities. In those works, the correlated local moments are a part of the TBG lattice itself, whereas here we consider additional adatom impurities coupled to the TBG host. The effective impurity models and corresponding electronic hybridization functions are rather different in these two cases.

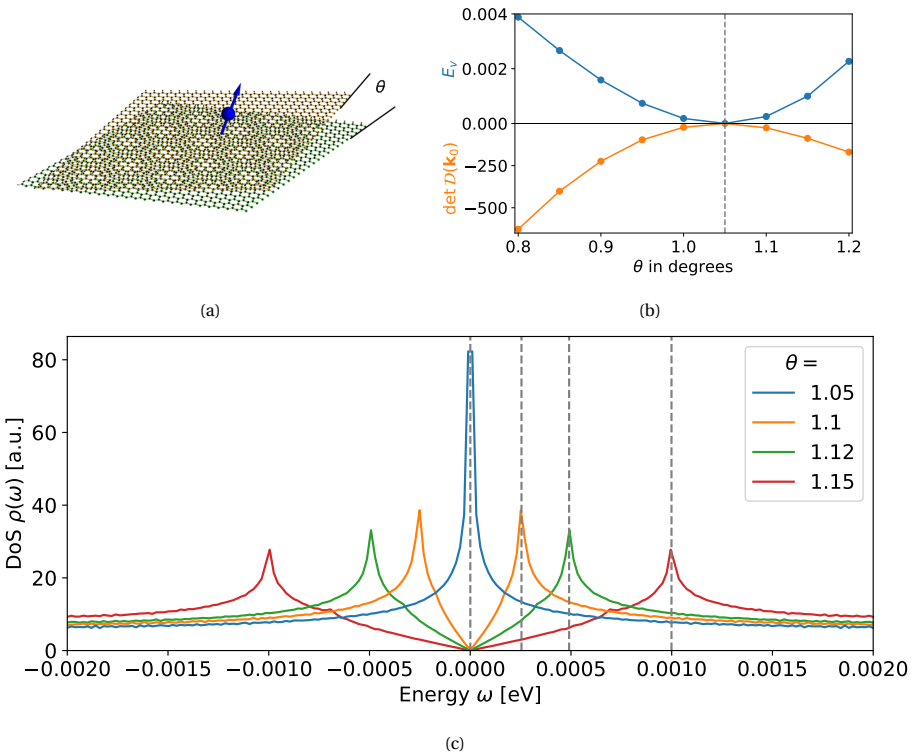

Figure 4.1: (a) Schematic representation of a magnetic impurity on the surface of the twisted bilayer graphene host material, with inter-layer twist angle θ. (b) Vanishing vHs saddle point scale E_v (top) and determinant of the saddle point Hessian (bottom) as the magic angle is approached, showing how two vHs's coalesce into a single HO-vHs. (c) Evolution of the clean TBG density of states for different twist angles near the magic angle at $\theta = 1.05°$. Vertical dashed lines indicate the energy of the dispersion saddle points E_v, which determine the van Hove singularity locations.

4.2. Van Hove singularities in the Bistritzer-MacDonald model

Before considering a Kondo impurity in TBG, we first analyze the clean host material, focusing on how the vHs's affect the band structure and local DoS. In the first part of this section we briefly recall the details of the Bistritzer-MacDonald (BM) model of TBG and its particle-hole symmetric limit. The original derivations were performed in Refs. [103, 161, 210]; further details are provided in the Appendices. In the second part, we analyze the formation of flat bands from saddle points and discuss the detailed structure of the lowest energy bands.

4.2.1. Particle-hole symmetric Bistritzer-MacDonald model

To describe TBG with a small twist angle θ, it is necessary to take into account both the intralayer hopping parameter t for each of the individual graphene layers, as well as the interlayer tunneling w. In the following we take these to be $t \approx 2.87\,\text{eV}$ and $w \approx 0.11\,\text{eV}$, as used in Ref. [103]. The twist angle between the layers generates a Moiré pattern with an emergent superlattice structure. For small twist angles θ, the characteristic Moiré length scale L_θ is given by $L_\theta = \sqrt{3}a/[2\sin(\theta/2)]$ with $a = 1.42\text{Å}$ being the interatomic distance in monolayer graphene. The corresponding effective low-energy Hamiltonian near the K point of the Moiré Brillouin zone (MBZ) has the form [103, 210],

$$H(\boldsymbol{k}) = \begin{pmatrix} h^K_{\frac{\theta}{2}}(\boldsymbol{k}) & wT_1 & wT_2 & wT_3 \\ wT_1^\dagger & h^K_{-\frac{\theta}{2}}(\boldsymbol{k}-\mathbf{q}_1) & 0 & 0 \\ wT_2^\dagger & 0 & h^K_{-\frac{\theta}{2}}(\boldsymbol{k}-\mathbf{q}_2) & 0 \\ wT_3^\dagger & 0 & 0 & h^K_{-\frac{\theta}{2}}(\boldsymbol{k}-\mathbf{q}_3) \end{pmatrix}. \tag{4.1}$$

The wave vector $\boldsymbol{k}$ is measured relative to the K point, and the Hamiltonian acts on 8-component wavefunctions $\Psi = \left(\psi_{0,\boldsymbol{k}}, \psi_{1,\boldsymbol{k}}, \psi_{2,\boldsymbol{k}}, \psi_{3,\boldsymbol{k}}\right)^T$, where $\psi_{0,\boldsymbol{k}}$ is a two-component spinor in the A-B sublattice basis in the top layer, and $\psi_{1(2,3),\boldsymbol{k}}$ are spinors in bottom layer at wave vectors $\boldsymbol{k} - \boldsymbol{q}_{1(2,3)}$. Here $h^K_\phi(\boldsymbol{k})$ is the effective low-energy Hamiltonian of single layer graphene near the K point, in a coordinate frame rotated by angle ϕ,

$$h^K_\phi(\boldsymbol{k}) = k v_F \begin{bmatrix} 0 & e^{i(\theta_{\boldsymbol{k}}-\phi)} \\ e^{-i(\theta_{\boldsymbol{k}}-\phi)} & 0 \end{bmatrix}. \tag{4.2}$$

Here, the angle θ_k measures the orientation of the momentum relative to the x-axis, $k = |\boldsymbol{k}|$, and the Fermi velocity is $v_F = 9.3 \times 10^7$ cm/s. The wave vectors $\boldsymbol{q}_{1,2,3}$ connecting K-points of the top and bottom layers are,

$$\mathbf{q}_1 = k_\theta\{0, -1\}, \tag{4.3a}$$

$$\mathbf{q}_2 = k_\theta \left\{\frac{\sqrt{3}}{2}, \frac{1}{2}\right\}, \tag{4.3b}$$

$$\mathbf{q}_3 = k_\theta \left\{-\frac{\sqrt{3}}{2}, \frac{1}{2}\right\}, \tag{4.3c}$$

with Moiré wave number, $k_\theta \equiv |\mathbf{q}_j| = \frac{8\pi}{3\sqrt{3}a}\sin\left(\frac{\theta}{2}\right)$.

Finally, the interlayer tunneling matrices $T_{1(2,3)}$ are expressed in terms of Pauli ma-

trices, viz:

$$T_1 = 1 + \sigma_x \,, \tag{4.4a}$$

$$T_2 = 1 - \frac{\sigma_x}{2} - \frac{\sqrt{3}\sigma_y}{2} \,, \tag{4.4b}$$

$$T_3 = 1 - \frac{\sigma_x}{2} + \frac{\sqrt{3}\sigma_y}{2} \,. \tag{4.4c}$$

The Hamiltonian Eq. (4.1) captures the essential physics of TBG and correctly predicts the first magic angle at $\theta \simeq 1.05°$. At the K point of the MBZ one finds that the lowest energy bands have a Dirac cone dispersion with an effective Fermi velocity,

$$v_F^\star = \frac{1 - 3w^2/(\hbar v_F k_\theta)^2}{1 + 6w^2/(\hbar v_F k_\theta)^2} \tag{4.5}$$

which vanishes exactly at the magic angle, where $\hbar v_F k_\theta = \sqrt{3}w$.

In the following, we will use the particle-hole symmetric version of the BM model. This form is obtained from Eq. (4.1) by eliminating subleading (second-order) corrections in the diagonal elements coming from the effect of the twist on the single layer Hamiltonian [210]. This is simply achieved by setting $\phi = 0$ in Eq. (4.2),

$$H(\boldsymbol{k}) = \begin{pmatrix} h_0^K(\boldsymbol{k}) & wT_1 & wT_2 & wT_3 \\ wT_1^\dagger & h_0^K(\boldsymbol{k}-\mathbf{q}_1) & 0 & 0 \\ wT_2^\dagger & 0 & h_0^K(\boldsymbol{k}-\mathbf{q}_2) & 0 \\ wT_3^\dagger & 0 & 0 & h_0^K(\boldsymbol{k}-\mathbf{q}_3) \end{pmatrix} . \tag{4.6}$$

The low-energy TBG DoS $\rho(\omega)$, obtained by diagonalizing this Hamiltonian is shown in Fig. 4.1c, for different twist angles in the vicinity of the magic angle at $\theta = 1.05°$. When precisely at the magic angle, we see a single divergence in the DoS at the Fermi energy. We measure energies relative to the Fermi energy and set $E_F = 0$, such that $\rho(\omega) = \rho(-\omega)$, embodying the particle-hole symmetry of Eq. (4.6). However, moving away from the magic angle, we have a Dirac cone feature, with pseudogap vanishing DoS $\rho(\omega) \sim |\omega|$ below an emergent scale $|\omega| \ll E_v$. We also see two vHs points with diverging DoS at $\omega = \pm E_v$. Below we analyze the low-energy bands and vHs structure of the model, extracting the angle dependence of the vHs scale E_v.

4.2.2. Characterization of van Hove singularities in the particle-hole symmetric BM model

We start our analysis of vHs properties in TBG by recalling the classification recently introduced in Refs. [83, 84, 211], which expands the definition from the usual vHs

with logarithmically diverging DoS [177] to include HO-vHs with power-law diverging DoS. For a band dispersion $\epsilon(\boldsymbol{k})$, which is a function of the 2D momentum vector $\boldsymbol{k}$, we calculate the first derivatives $\nabla_{\boldsymbol{k}}\epsilon(\boldsymbol{k})$, and the Hessian matrix of second derivatives $\mathscr{D}_{ij}(\boldsymbol{k}) \equiv \frac{1}{2}\partial_{k_i}\partial_{k_j}\varepsilon(\boldsymbol{k})$. The Hellman-Feynman theorem allows to carry this out with high numerical accuracy (see Appendix 4.6.1). A logarithmic vHs arises at a point $\boldsymbol{k}_0$ in the dispersion corresponding to a saddle point when:

$$\text{log vHs:} \quad \nabla_{\boldsymbol{k}}\varepsilon(\boldsymbol{k}_0) = \mathbf{0} \;\text{ and }\; \det\mathscr{D}(\boldsymbol{k}_0) < 0\,. \tag{4.7}$$

The negative Hessian determinant means that we have both a maximum and a minimum in each of the principal directions of the saddle point. A higher-order saddle point, corresponding to a HO-vHs, is instead characterized by zero determinant of Hessian matrix:

$$\text{HO-vHs:} \quad \nabla_{\boldsymbol{k}}\varepsilon(\boldsymbol{k}_0) = \mathbf{0} \;\text{ and }\; \det\mathscr{D}(\boldsymbol{k}_0) = 0\,. \tag{4.8}$$

In addition, higher-order saddle points can be classified according to the leading polynomial terms in an expansion of the dispersion $\epsilon(\boldsymbol{k})$ around the saddle point $\boldsymbol{k}_0$ [84, 211]. These leading terms in the expansion correspond directly to the numerical exponent of the power-law divergence in the DoS.

With the help of this classification, we proceed to investigate the structure of the lowest band in the BM model Hamiltonian given by Eq. (4.6). Using particle-hole symmetry in conjunction with the transformation $k_x \to -k_x$ allows us to concentrate only on the lowest positive energy band for our analysis. Technical details of our numerical implementation are presented in Appendix 4.6.1. In Fig. 4.1b we show the numerically-computed E_v scale (top panel) and the determinant of the saddle-point Hessian $\det\mathscr{D}(\boldsymbol{k}_0)$ (bottom panel) as a function of twist angle. Both are seen to vanish at the magic angle, heralding the emergence of the HO-vHs at this point. This behavior is further analyzed below.

In Fig. 4.2 we plot the momentum-resolved spectrum of the BM model for twist angles $\theta = 1.2^\circ$ (panel a) and $\theta = 1.05^\circ$ (panel b). We compute $\nabla_{\boldsymbol{k}}\varepsilon(\boldsymbol{k})$ throughout the MBZ and search for the vHs points for which $\nabla_{\boldsymbol{k}}\varepsilon(\boldsymbol{k}) = \mathbf{0}$. These are indicated in both panels as the red circle points.

Having located the vHs points in the MBZ for a given twist angle, we can classify them and study their neighborhood in momentum space. Away from the magic angle (e.g. for $\theta = 1.2^\circ$ shown in Fig. 4.2a), we indeed find a negative determinant of the Hessian $\det\mathscr{D}(\boldsymbol{k}_0) < 0$, and the vHs's have a local hyperbolic geometry in momentum space. The dispersion is found to have the leading form,

$$\epsilon_{\mathbf{p}} = E_v + \alpha p_x^2 - \beta p_y^2\,, \tag{4.9}$$

where the coefficients are obtained from the eigenvalues of the Hessian, and the labels p_x and p_y are measured in the principal directions of the saddle point, with

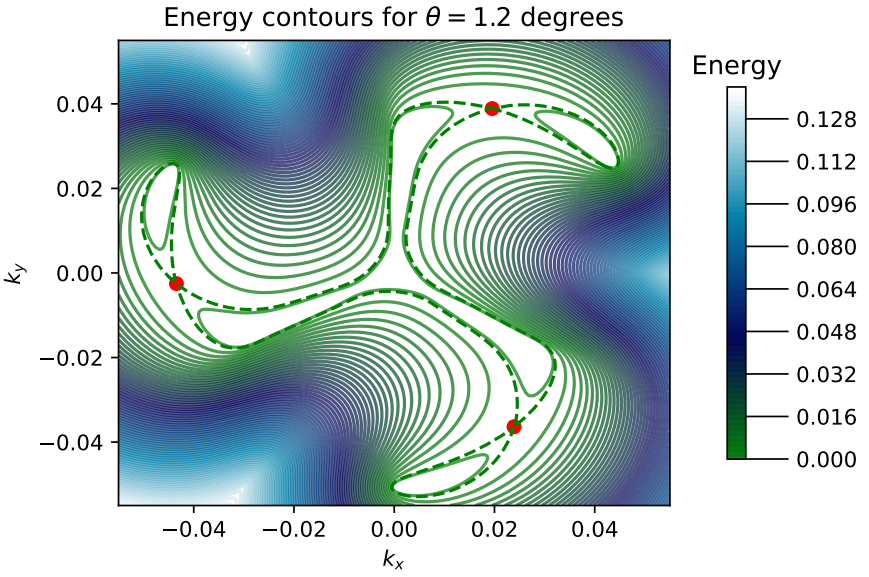

(a) Conventional vHs

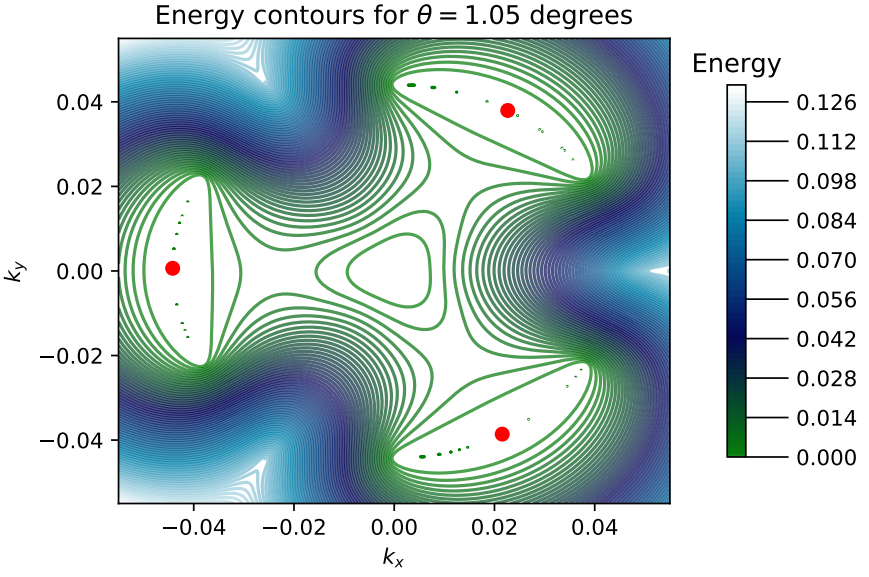

(b) Higher Order vHs at the magic angle

Figure 4.2: Low-energy features of the particle-hole symmetric BM model of pristine TBG, showing energy contours of the dispersion $\varepsilon(\boldsymbol{k})$ as a function of momentum $\boldsymbol{k}$ in the extended MBZ. Red points show the saddle points of the dispersion, corresponding to the van Hove singularities. Dashed lines show the contours at energy E_v, on which the van Hove points sit.

$\mathbf{p} = 0$ defining the saddle point itself. The corresponding leading correction to the DoS then takes the form,

$$\rho(\omega) = \frac{1}{4\pi^2}\frac{1}{\sqrt{\alpha\beta}}\ln\left|\frac{D}{\omega - E_v}\right|, \tag{4.10}$$

where D is a high-energy cutoff, taken to be the conduction electron bandwidth. In this way, we may extract the vHs scale E_v.

As we begin twisting toward the magic angle, the vHs energy scale E_v starts to decrease, and the two logarithmic singularities at $\omega = \pm E_v$ therefore move closer together. Furthermore, the magnitude of the Hessian at the vHs, $|\det \mathscr{D}(\boldsymbol{k}_0)|$, also decreases. The two vHs points merge at $\omega = 0$ precisely at the magic angle $\theta = 1.05°$ [178], at which point the Hessian also vanishes, $\det \mathscr{D}(\boldsymbol{k}_0) = 0$. This transition is shown in Fig. 4.1b. As the magic angle is approached and the HO-vHs is formed, we see a further flattening of the dispersion in the p_y direction. The fittingly-named higher-order singularity requires a higher-order polynomial to faithfully capture its dispersion. The lowest polynomial which correctly captures all the symmetries is given by,

$$\epsilon_{\mathbf{p}} = \alpha p_x^2 + \gamma p_x p_y^2 + \kappa p_y^4 . \tag{4.11}$$

This comes hand-in-hand with a sharper, power-law divergence in the DoS,

$$\rho(\omega) = (2\pi)^{-\frac{5}{2}}\Gamma(\tfrac{1}{4})^2(4\alpha\tilde{\Gamma}^2)^{-1/4}\,|\omega|^{-1/4}, \tag{4.12}$$

with $\tilde{\Gamma}^2 = \gamma^2 - 4\alpha\kappa$ and $\Gamma(x)$ the usual gamma function.

The low-energy DoS at different angles can be computed numerically by binning histograms of energies for the lowest band of the BM model, as shown in Fig.4.1c. Away from the magic angle, the numerical calculation indicates a linear DoS around the Fermi energy, coming from the Dirac cone in the spectrum. Around $\omega = \pm E_v$ we see the vHs log-divergences. At the magic angle, the HO-vHs around the Fermi energy 'eat up' the Dirac cone, and we have instead a large DoS at low energies, diverging as $\rho(\omega) \sim |\omega|^{-1/4}$.

4.3. The Kondo problem

The Kondo effect is a classic paradigm in many-body quantum physics [188]. The corresponding Kondo model features a single quantum spin-$\frac{1}{2}$ magnetic impurity coupled by antiferromagnetic exchange to a single channel of non-interacting conduction electrons. Originally, the Kondo model was formulated to describe dilute magnetic impurities such as iron, in bulk metals such as gold [185, 212]. In these metallic systems, an impurity local moment becomes strongly entangled with its surrounding conduction electrons at low temperatures, and is dynamically screened

[213–215]. This leads to dramatically enhanced spin-flip scattering in the host metal, which can be detected spectroscopically [186].

A more microscopic starting point is provided by the single impurity Anderson model [188], which describes the impurity as a single quantum orbital with strong electron interactions,

$$\begin{aligned} H_{\mathrm{AM}} = H_{\mathrm{host}} \quad & +\epsilon_d \textstyle\sum_\sigma d_\sigma^\dagger d_\sigma + U_d d_\uparrow^\dagger d_\uparrow d_\downarrow^\dagger d_\downarrow \\ & +g \textstyle\sum_\sigma \left(d_\sigma^\dagger c_{0,\sigma} + c_{0,\sigma}^\dagger d_\sigma \right), \end{aligned} \tag{4.13}$$

where $d_\sigma^{(\dagger)}$ is an annihilation (creation) operator for an impurity electron with spin $\sigma = \uparrow/\downarrow$, and $H_{\mathrm{host}} = \sum_{k,\sigma} \epsilon_k c_{k,\sigma}^\dagger c_{k,\sigma}$ describes the clean host. Here $c_{k,\sigma}^{(\dagger)}$ annihilates (creates) a conduction electron of the host material with momentum k and spin σ. We do not employ band indices in this expression. The impurity couples locally in real-space to the effective host orbital $c_{0,\sigma} = \sum_k \xi_k c_{k,\sigma}$, where ξ_k is the weight of state k at the impurity location (taken to be at the origin).

For small host-impurity hybridization g, repulsive Coulomb interaction $U_d > 0$, and suitably-chosen impurity potential $-U_d < \epsilon_d < 0$, a spin-$\frac{1}{2}$ local moment can be trapped on the impurity. Projecting onto this doubly-degenerate spin-$\frac{1}{2}$ manifold of impurity states by eliminating virtual excitations to empty or doubly-occupied impurity configurations by means of a Schrieffer-Wolff (SW) transformation [188, 216] yields the simpler Kondo model,

$$H_{\mathrm{KM}} = H_{\mathrm{host}} \quad + J \boldsymbol{S} \cdot \boldsymbol{s}_0 + V \textstyle\sum_\sigma c_{0,\sigma}^\dagger c_{0,\sigma}, \tag{4.14}$$

where $J > 0$ is the antiferromagnetic exchange interaction between the impurity spin-$\frac{1}{2}$ degree of freedom $\boldsymbol{S}$, and the *spin density* of the host conduction electrons at the impurity position $\boldsymbol{s}_0 = \frac{1}{2} \sum_{\alpha,\beta} c_{0,\alpha}^\dagger \boldsymbol{\sigma}_{\alpha\beta} c_{0,\beta}$, where $\boldsymbol{\sigma}$ is the vector of Pauli matrices. The third term describes potential scattering of the host conduction electrons induced by the impurity (since $c_{0,\sigma}^\dagger c_{0,\sigma} = \sum_{k,k'} \xi_k \xi_{k'} c_{k,\sigma}^\dagger c_{k',\sigma}$).

The standard Schrieffer-Wolff result [188, 216], which becomes exact in the limit $U_d/g^2 \to \infty$, yields $J = 2g^2[(U_d + \epsilon_d)^{-1} - (\epsilon_d)^{-1}]$ and $V = -g^2[(U_d + \epsilon_d)^{-1} + (\epsilon_d)^{-1}]$. At the particle-hole symmetric point of the model $\epsilon_d = -U_d/2$, we therefore obtain $J = 8g^2/U_d$ and $V = 0$ (the latter result can be viewed as a many-body quantum destructive interference effect between particle and hole processes). Although the Kondo model Eq. (4.14) correctly captures the low-energy physics of Eq. (4.13), it should be noted that for realistic values of U_d, ϵ_d, and g outside of the strict perturbative regime, the values of the effective parameters J and V must be obtained by more sophisticated means that take into account renormalization from the conduction electrons and the specific conduction electron DoS [217]. We also emphasize that J and V are not independent parameters in Eq. (4.14), being both derived from the same microscopic parameters of the underlying Anderson model.

The physics of the impurity problem is controlled by the local (free) conduction electron DoS seen by the impurity, $\rho_\sigma(\omega) = -\frac{1}{\pi}\mathrm{Im}\,\langle\langle c_{0,\sigma}; c^\dagger_{0,\sigma}\rangle\rangle^0$, where $\langle\langle c_{0,\sigma}; c^\dagger_{0,\sigma}\rangle\rangle$ is the retarded, real-frequency local host Green's function at the impurity position, and the 0 superscript denotes that it is calculated for the clean host.

In this work we consider a single magnetic impurity (the 'dilute limit') embedded in an otherwise clean host TBG system modelled by the BM model. $SU(2)$ spin symmetry is taken to be unbroken. We also assume that the impurity couples equally to all BM bands independently of the impurity position (ξ_k is constant for all momenta and band indices), such that $\rho_\sigma(\omega) \equiv \rho(\omega)$ is the TBG DoS, whose low-energy form is described by Eqs. (4.10) or (4.12). This is certainly a simplification, since details of the impurity-TBG hybridization will naturally affect details of the impurity response. The specific form of the impurity hybridization function will in practice depend on the impurity location within the moiré unit cell and how the impurity couples in real-space to the constituent TBG carbon atoms. We leave such *ab initio* studies for future work. However, the rich physics uncovered below will remain qualitatively unaltered provided the impurity hybridization function still features van Hove divergences flanking a central pseudogap Dirac cone. Since the origin of these features is rooted deeply in the symmetry and topology of the TBG material, we expect the idealized Kondo physics described here to be rather generic. On the other hand, insights from monolayer graphene [195] indicate that the physics of vacancies in TBG or substitutional dopants may drastically differ, since the local DoS in these cases is strongly modified.

In the rest of this section we review the methods that we use to attack the problem as well as the quantities to be analyzed.

4.3.1. Poor man's scaling approach

The Kondo model as defined by Eq. (4.14) is a nontrivial strong correlation problem. For metallic host systems, the first insights were provided by Kondo's calculation of the scattering T-matrix [212], which is related to the impurity spectral function. Kondo found a low-temperature divergence in perturbation theory: even when the bare J is small, straight perturbation theory does not give a good description of the low-temperature physics or a proper understanding of the many-body ground state of the system. This divergence was better understood by Anderson's self-coined 'poor-man's scaling' approach [218] – a precursor to the renormalization group (RG). It identified an emergent low-energy scale T_K – the Kondo temperature – below which perturbation theory breaks down, and the problem becomes a strong coupling problem. We briefly introduce the method here, since we will employ it in the next section to understand analytically the scaling properties of an impurity in the TBG host.

Conventionally in the poor man's scaling approach, one uses dimensionless couplings $j = \rho_0 J$ and $v = \rho_0 V$ with $\rho_0 = \rho(\omega = 0)$ the Fermi level DoS. However, for consideration of Dirac systems where ρ_0 may in fact vanish, a different choice is required. Here we simply use the original dimensionful couplings J and V. Furthermore, we assume that the host DoS is particle-hole symmetric, meaning $\rho(\omega) = \rho(-\omega)$, a property satisfied by Eq. (4.6); and is defined within a band of halfwidth D, meaning $\rho(\omega) \propto \theta(D - |\omega|)$.

Anderson's scaling procedure goes as follows [218]: (i) integrate out high energy conduction electron states $D - \delta D < |\omega| < D$ close to the band edges in a shell of width δD; (ii) incorporate the effect of virtual excitations to these eliminated states perturbatively by rescaling the couplings J and V to give an effective Hamiltonian of the same form but defined with a reduced bandwidth $D \to D - \delta D$; (iii) study the flow of the parameters J and V on successive reduction of the bandwidth. Making δD infinitessimal, one obtains the following scaling equations,

$$\begin{aligned} \frac{dJ}{dD} &= -\frac{\rho(D)}{D} J^2 , \\ \frac{dV}{dD} &= 0 . \end{aligned} \tag{4.15}$$

The first equation determines the flow of the coupling constant J on reducing the bandwidth, whereas the second equation shows that the potential scattering V does not flow. If the bare model is particle-hole symmetric then no potential scattering is generated under the scaling procedure. In the remainder of this paper we will focus on the case $V = 0$. The scaling equation for J gives insight into the breakdown of perturbation theory and hence T_K, by identifying the point where the rescaled J diverges. We consider various relevant situations in the following.

4.3.2. Numerical Renormalization Group

Wilson's numerical renormalization group [219, 220] (NRG) is a non-perturbative technique for solving quantum impurity type problems. It builds upon Anderson's perturbative scaling ideas [218], but overcomes its limitations by establishing a more general framework in terms of which physical quantities can be calculated numerically-exactly, down to zero temperature. Wilson's original formulation of NRG [219], designed to obtain the thermodynamic properties of a single magnetic impurity in a metal, has since been extended to deal with arbitrary host systems [220–222], and to the calculation of dynamical quantities via the full-density-matrix NRG approach [223, 224]. The former has allowed NRG to be applied to monolayer graphene [193], and other Dirac systems [196, 197]. The latter provides access to highly accurate spectral data, with excellent real-frequency resolution, at any temperature. NRG has also been adapted over the years to extend the range of problems that can be

tackled and improve accuracy or efficiency [225–232], making it the gold-standard method of choice for solving generalized quantum impurity problems.

The basic NRG algorithm [219, 220] proceeds as follows. (i) The local conduction electron density of states $\rho(\omega)$ of the pristine host material (without the impurity) must first be calculated.
(ii) This DoS is then discretized logarithmically by dividing it up into intervals according to the discretization points $\pm D\Lambda^{-n}$, where D is the bare conduction electron bandwidth, $\Lambda > 1$ is the NRG discretization parameter, and $n = 0, 1, 2, 3, \ldots$. The continuous electronic density in each interval is replaced by a single pole at the average position with the same total weight, yielding $\rho^{\mathrm{disc}}(\omega)$.
(iii) The conduction electron part of the Hamiltonian H_{host} is then mapped into the form of a 'Wilson chain',

$$H_{\mathrm{host}} \to H_{\mathrm{host}}^{\mathrm{disc}} = \sum_{\sigma} \sum_{n=0}^{\infty} \Big[\quad t_n \left(f_{n,\sigma}^{\dagger} f_{n+1,\sigma} + f_{n+1,\sigma}^{\dagger} f_{n,\sigma} \right) + \epsilon_n f_{n,\sigma}^{\dagger} f_{n,\sigma} \Big], \tag{4.16}$$

where the Wilson chain coefficients $\{t_n\}$ and $\{\epsilon_n\}$ are determined such that the DoS at the end of the chain reproduces exactly the discretized host DoS, that is $-\frac{1}{\pi}\mathrm{Im}\,\langle\langle f_{0,\sigma}; f_{0,\sigma}^{\dagger}\rangle\rangle = \rho^{\mathrm{disc}}(\omega)$. For a system with particle-hole symmetry, $\epsilon_n = 0$ for all n. Due to the logarithmic discretization, the Wilson chain hopping parameters decay roughly exponentially down the chain, $t_n \sim \Lambda^{-n/2}$, although the precise details are also important since they encode the specific host DoS [220].
(iv) The impurity is coupled to site $n = 0$ of the Wilson chain. We define a sequence of Hamiltonians H_N comprising the impurity and the first N Wilson chain sites,

$$H_N = H_{\mathrm{imp}} + H_{\mathrm{hyb}} + \sum_{\sigma} \Big[\sum_{n=0}^{N} \epsilon_n f_{n,\sigma}^{\dagger} f_{n,\sigma} + \sum_{n=0}^{N-1} t_n \left(f_{n,\sigma}^{\dagger} f_{n+1,\sigma} + f_{n+1,\sigma}^{\dagger} f_{n,\sigma} \right) \Big], \tag{4.17}$$

where for the Anderson model $H_{\mathrm{imp}} = \epsilon_d \sum_\sigma d_\sigma^{\dagger} d_\sigma + U_d d_\uparrow^{\dagger} d_\uparrow d_\downarrow^{\dagger} d_\downarrow$ and $H_{\mathrm{hyb}} = g\sum_\sigma (d_\sigma^{\dagger} f_{0,\sigma} + f_{0,\sigma}^{\dagger} d_\sigma)$ while for the Kondo model $H_{\mathrm{imp}} + H_{\mathrm{hyb}} = J\boldsymbol{S}\cdot\boldsymbol{s}_0 + V\sum_\sigma f_{0,\sigma}^{\dagger} f_{0,\sigma}$ with $\boldsymbol{s}_0 = \frac{1}{2}\sum_{\alpha,\beta} f_{0,\alpha}^{\dagger} \boldsymbol{\sigma}_{\alpha\beta} f_{0,\beta}$. From Eq. (4.17) we obtain the recursion relation,

$$H_N = H_{N-1} + \sum_{\sigma} \Big[\epsilon_N f_{N,\sigma}^{\dagger} f_{N,\sigma} + t_N \left(f_{N-1,\sigma}^{\dagger} f_{N,\sigma} + f_{N,\sigma}^{\dagger} f_{N-1,\sigma} \right) \Big], \tag{4.18}$$

such that the full (discretized) model is obtained as $H^{\mathrm{disc}} = \lim_{N\to\infty} H_N$ [233].
(v) Starting from the impurity, we build up the chain by successively adding Wilson chain sites using the recursion, Eq. (4.18). At each step N, the intermediate Hamiltonian H_N is diagonalized, and only the lowest N_s states are retained to construct the

Hamiltonian H_{N+1} at the next step (the higher energy states are discarded). In such a way, we focus on progressively lower energy scales with each iteration. Furthermore, the iterative diagonalization and truncation procedure can be viewed as an RG transformation [219], $H_{N+1} = \mathscr{R}[H_N]$.
(vi) The partition function Z_N can be calculated from the diagonalized Hamiltonian H_N at each step N. Wilson used RG arguments to show [219] that thermodynamic properties obtained from Z_N at an effective temperature $T_N \sim \Lambda^{-N/2}$ accurately approximate those of the original undiscretized model at the same temperature. The sequence of H_N can therefore be viewed as coarse-grained versions of the full model, which faithfully capture the physics at progressively lower and lower temperatures.
(vii) The discarded states at each step form a complete set (the Anders-Schiller basis [223]), from which the NRG full density matrix can be constructed. This provides a rigorous way of calculating real-frequency dynamical quantities via the Lehmann representation [224].

In this work, we take the DoS $\rho(\omega)$ of the TBG system for a given twist angle θ (as calculated from the BM model in Sec. 4.2), discretize it logarithmically, and map to Wilson chains. The DoS used and the resulting Wilson chains are shown in Appendix 4.6.2. NRG is then used to solve the Anderson and Kondo models describing an impurity embedded in the TBG host. Thermodynamic and dynamical quantities are calculated and discussed in Sec. 4.4. Throughout, we use an NRG discretization parameter $\Lambda = 2$ and retain $N_s = 4000$ states at each step of the calculation.

4.3.3. Observables

The physics of an impurity in the TBG host can be characterized by a number of observables, both thermodynamic and dynamical. Here we consider the impurity contribution to the total thermal entropy $S_{\text{imp}}(T)$ as a function of the temperature T, and the low-T impurity spectral function $A(\omega)$ as a function of energy ω.

The impurity entropy readily allows us to extract the Kondo scale T_K from NRG data, to track accurately the RG flow, and to identify RG fixed points. It is defined as $S_{\text{imp}}(T) = S_{\text{tot}}(T) - S_0(T)$, where S_{tot} is the entropy of the entire system, while S_0 is the entropy of the free TBG host without impurities. The residual impurity entropy $S_{\text{imp}}(T = 0)$, is a finite universal number of order unity which characterizes the stable RG fixed point and hence the ground state of the system; for example $S_{\text{imp}}(0) = \ln 2$ for a free, unscreened impurity spin $S = \frac{1}{2}$ local moment.

The impurity spectral function gives dynamical information and is accessible experimentally via scanning tunneling spectroscopy (STS), which probes the energy-resolved impurity density of states [186]. For an Anderson impurity it is related to the impurity Green's function, $A(\omega) = -\frac{1}{\pi}\text{Im}\, G_{dd}(\omega)$ where $G_{dd}(\omega) = \langle\langle d_\sigma; d_\sigma^\dagger\rangle\rangle$.

Electronic scattering in the TBG system induced by the impurity is characterized by the t-matrix, which in turn is controlled by the impurity Green's function. In momentum space, the t-matrix equation reads,

$$G_{kk'}(\omega) = \delta_{kk'} G^0_{kk}(\omega) + G^0_{kk}(\omega)\, T_{kk'}(\omega) G^0_{k'k'}(\omega)\,, \tag{4.19}$$

where $G^{(0)}_{kk'}(\omega) = \langle\langle c_{k,\sigma}; c^\dagger_{k',\sigma}\rangle\rangle^{(0)}$ is the electron Green's function for the full (free) TBG system with (without) the impurity, and $T_{kk'}(\omega) = g^2 \xi_k \xi_{k'} G_{dd}(\omega)$ is the t-matrix itself. Transforming to real space, the t-matrix equation becomes,

$$G_{\boldsymbol{r}_i \boldsymbol{r}_j}(\omega) = G^0_{\boldsymbol{r}_i \boldsymbol{r}_j}(\omega) + G^0_{\boldsymbol{r}_i \boldsymbol{r}_0}(\omega)\, T(\omega) G^0_{\boldsymbol{r}_0 \boldsymbol{r}_j}(\omega)\,, \tag{4.20}$$

where $G^{(0)}_{\boldsymbol{r}_i \boldsymbol{r}_j}(\omega)$ are the full (free) electronic propagators between real-space sites $\boldsymbol{r}_i$ and $\boldsymbol{r}_j$ of the TBG system, and the local t-matrix is $T(\omega) = g^2 G_{dd}(\omega)$. The impurity is taken to be located at site $\boldsymbol{r}_0$.

A related experimental quantity obtained by Fourier transform STS [184] (FT-STS) is the quasiparticle interference (QPI) pattern, defined as,

$$\Delta\rho(\boldsymbol{q}, \omega) = \sum_i e^{-i\boldsymbol{q}\cdot\boldsymbol{r}_i} \Delta\rho(\boldsymbol{r}_i, \omega)\,, \tag{4.21}$$

where $\Delta\rho(\boldsymbol{r}_i, \omega) = -\frac{1}{\pi}\mathrm{Im}\,[G_{\boldsymbol{r}_i \boldsymbol{r}_i}(\omega) - G^0_{\boldsymbol{r}_i \boldsymbol{r}_i}(\omega)]$ is the difference in electronic density at site $\boldsymbol{r}_i$ due to the impurity. As such, the QPI pattern $\Delta\rho(\boldsymbol{q}, \omega)$ can be obtained entirely from the free TBG propagators and the impurity Green's function, via the t-matrix equation.

In the following, we study the zero temperature, $T = 0$, impurity spectral function $A(\omega)$ using NRG; the t-matrix and QPI can be obtained from this as described above.

4.3.4. Limiting cases of the Kondo problem

The physics of the Kondo model strongly depends on the host DoS. For the problem of a magnetic impurity in a TBG host, as modelled using the BM model, there are a number of relevant limits. We assume that the impurity couples to all the orbitals in the same way meaning the local TBG DoS $\rho(\omega)$ is the only relevant quantity characterizing the host. Furthermore, we consider here the particle-hole symmetric case $V = 0$ for simplicity.

The main insights of the ensuing discussion are summarized in Table 4.1.

The metallic limit

The case of a magnetic impurity embedded in a metallic host is the most commonly encountered and well-studied situation, with extensive literature to its name (see

	Density of States, $\rho(\omega)$	Kondo Temperature, T_K	$S_{\text{imp}}(T=0)$
Metal	ρ_0	$De^{-1/\rho_0 J}$	0
vHS	$\rho_0\left[1+a\ln\left(D/\lvert\omega\rvert\right)\right]$	$De^{\frac{1}{a}-\frac{1}{a}\sqrt{1+\frac{2a}{\rho_0 J}}}$	0
HOvHS	$\rho_0\lvert\omega\rvert^{-\alpha}$	$D\left(1+\frac{\alpha D^\alpha}{\rho_0 J}\right)^{-1/\alpha}$	$-2\alpha\ln 2$
Dirac	$\rho_0\lvert\omega\rvert$	$T_K=0$	$\ln 2$

Table 4.1: Summary of properties for the Kondo model with the different host DoS encountered in this work.

Ref. [188] for an introduction). The most important feature of the problem is that upon reducing the temperature, the system becomes increasingly strongly correlated. This is captured by the poor-man's scaling equation, Eq. (4.15). In a metal, it is a reasonable assumption that the DoS is roughly constant within the relevant energy window, $\rho(\omega)\approx\rho_0$. Integrating Eq. (4.15) then straightforwardly yields,

$$J(\Lambda)=\frac{J_0}{1+\rho_0 J_0\ln\left(\frac{\Lambda}{D}\right)}\,, \tag{4.22}$$

where Λ is the energy scale of interest whereas D is the starting high-energy cutoff (physically D is the conduction electron bandwidth). J_0 is the starting value of the coupling constant at the scale D (with $J_0\equiv J$ in Eq. (4.14)) whereas $J(\Lambda)$ is the running coupling strength at energy scale Λ. Perturbation theory breaks down, once the running coupling $J(\Lambda=T_K)\to\infty$. This happens at the root of the denominator and the corresponding running energy scale reads

$$T_K=De^{-1/(\rho_0 J_0)}\,. \tag{4.23}$$

This energy scale has a number of interpretations. One implication is that for temperatures $T\gg T_K$, the physics can be captured using a perturbative expansion around $J=0$, meaning the limit of a free impurity henceforth referred to as the local moment (LM) regime. Consequently, the impurity entropy, up to small correction, is that of a free spin, meaning $S_{\text{imp}}^{\text{LM}}=\log 2$.

Conversely, for $T\sim T_K$, perturbation theory breaks down. Nozières showed [234] that at zero temperature, the ground state is a complicated many-body spin-singlet state and the system is a local Fermi liquid. The low-temperature limit $T\ll T_K$ is referred to as the strong coupling (SC) regime. The corresponding impurity entropy is that of a unique state with $S_{\text{imp}}^{\text{SC}}=0$. The strong coupling physics in this regime shows up in the local spectral function $A(\omega)$ as a strong quasiparticle resonance around the Fermi energy, with a spectral pinning condition satisfying the Friedel sum rule [188]. The RG flow between the two fixed points is relatively simple, with $J(\Lambda)$ increasing from LM to SC as the energy scale Λ is decreased. This is illustrated in the upper panel of Fig. 4.3. The Kondo scale T_K is the scaling invariant along this RG flow. Note that

in the metallic case, the potential scattering V is strictly marginal and consequently plays no role.

Close to a van Hove singularity

This case is a twist on the usual metallic Kondo problem, with very similar physics. The poor man's scaling analysis points to an RG flow from weak to strong coupling, with the running coupling $J(\Lambda)$ again increasing from LM to SC as the energy scale Λ is decreased (Fig. 4.3, upper panel). The main difference from the standard metallic case is an enhanced Kondo temperature [235–237] due to the enhanced DoS, which diverges logarithmically at low energies for standard vHs points. Taking the low-energy form of the DoS to be $\rho(\omega) = \rho_0(1 + a\ln(D/|\omega|))$, we can integrate Eq. (4.15) and, as before, extract the Kondo scale from the divergence in $J(\Lambda)$. In this case we obtain,

$$T_K = De^{\frac{1}{a} - \frac{1}{a}\sqrt{1+\frac{2a}{\rho_0 J_0}}} . \tag{4.24}$$

Note that for $a \to 0$ the DoS becomes metallic and we recover the metallic limit result for T_K.

This expression has two limiting cases and the relevant parameter is now $a/(\rho_0 J_0)$: (i) For $a/(\rho_0 J_0) \ll 1$, the logarithmic enhancement of the DoS plays no role and one recovers the metallic limit result, $T_K = De^{-1/(\rho_0 J_0)}$ since the system starts out already close to the SC fixed point; (ii) In the opposite limit, $a/(\rho_0 J_0) \gg 1$, we find $T_K = De^{-\sqrt{\frac{2}{a\rho_0 J_0}}}$, which is strongly boosted relative to the metallic case. The Kondo temperature T_K is therefore enhanced in the vicinity of a vHs. As expected, the impurity entropy is quenched at low temperatures, $S_{\text{imp}}(T \to 0) = 0$, embodying Kondo singlet formation. In terms of the impurity spectral function $A(\omega)$, the quasiparticle Kondo resonance around the fermi energy is in fact suppressed logarithmically by the logarithmically diverging DoS of the free host [189]. However, the fact that $A(\omega = 0) = 0$ should not in this case be interpreted as a flow towards weak coupling since the relevant quantity is rather $\rho(\omega) \times A(\omega)$, which remains finite as $|\omega| \to 0$ and satisfies a generalized Friedel sum rule [238] for strong coupling physics.

Close to a Higher Order van Hove singularity

As discussed in Sec. 4.2, a HO-vHs is characterized by a power-law divergence in the DoS. In the following discussion, we neglect the metallic background on top of which the power-law divergence sits, and take the DoS to be of the form $\rho(\omega) = \rho_0|\omega|^{-\alpha}$ with $0 < \alpha < 1$. This problem falls into the class of power-law Kondo problems [239]. Intuitively, one expects the Kondo temperature to be further enhanced through the

more strongly divergent DoS. Integrating Eq. (4.15) with this DoS yields,

$$T_K = \frac{D}{\left(1+\frac{\alpha D^\alpha}{\rho_0 J_0}\right)^{1/\alpha}} . \tag{4.25}$$

This problem also has two limits, one characterized by the local moment physics of a free impurity (LM) the other limit by a particle-hole symmetric strong coupling fixed point that we henceforth call $\mathrm{SSC_{HO}}$. This RG fixed point has properties that are slightly different from the metallic strong coupling fixed point SC. It is characterized by a $T \to 0$ impurity entropy of $S_{\mathrm{imp}} = -2\alpha \ln 2$, which is negative. We emphasize that although the total thermodynamic entropy is of course never negative, the *impurity contribution* to the total system entropy as defined in Sec. 4.3.3 can be negative, if the presence of the impurity causes dramatic changes to the host (local) electronic structure, relative to the clean host. This is precisely the case for the power-law Kondo model [239]. As for the impurity spectral function, the quasiparticle Kondo resonance is suppressed by the divergent free host DoS, and we find $A(\omega) \sim |\omega|^\alpha$ at low energies. But again, the signature of Kondo singlet formation and strong coupling physics is that $\rho(\omega) \times A(\omega)$ remains finite as $|\omega| \to 0$, which is indeed the case for $\mathrm{SSC_{HO}}$.

The RG flow in the particle-hole symmetric case considered here is again one-dimensional, running from LM to $\mathrm{SSC_{HO}}$ as the energy scale or temperature is reduced (see middle panel of Fig. 4.3). We note that strong particle-hole asymmetry can play a role in the power-law Kondo model, unlike the pure metallic case, and leads to the intricate phase diagram discussed in Ref. [239].

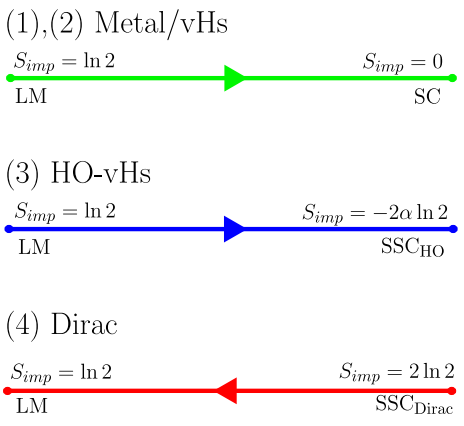

Figure 4.3: One-dimensional RG diagram showing the flow into different stable fixed points as the temperature is lowered, for different host density of states profiles.

The limit of a two-dimensional Dirac cone

The linear vanishing DoS associated with a Dirac cone in two dimensional systems gives rise to a subtle impurity problem which falls into the class of so-called pseudogap Kondo models. This is by far the most complicated situation; it has been discussed at length in Refs. [194, 238, 240–242]. In the following, we focus on the particle-hole symmetric case, with a linear pseudogap $\rho(\omega) = \rho_0|\omega|$ that is characteristic of 2d Dirac materials. Naively, one might expect a reduced Kondo temperature due to the reduced DoS of a Dirac cone compared with that of a metal. In fact, the Kondo effect is suppressed entirely in this case and T_K vanishes, regardless of the strength of the bare coupling J_0. The LM fixed point is stable and the impurity local moment remains unscreened.

For large bare J_0 the system starts off close to the particle-hole symmetric strong coupling fixed point of the linear pseudogap Kondo model, dubbed $\mathrm{SSC}_{\mathrm{Dirac}}$. In this regime, the impurity entropy is $S_{\mathrm{imp}} = 2\ln 2$. However, this fixed point is unstable and RG flow on reducing the temperature tends towards the LM fixed point with entropy $S_{\mathrm{imp}} = \ln 2$. Unlike the other cases considered, here the renormalized running coupling $J(\Lambda)$ *decreases* on reducing temperature, so that the impurity always becomes asymptotically free as $T \to 0$. This is illustrated in the lower panel of Fig. 4.3. The Kondo effect can only be revived by doping so that the Dirac point is not longer at the fermi energy (in which case the low-energy DoS is finite and we recover the metallic scenario); or if very strong potential scattering is introduced. For the linear pseudogap case $\rho(\omega) \sim |\omega|$ the impurity spectral function also goes as $A(\omega) \sim |\omega|$. Note that in this case $\rho(\omega) \times A(\omega) \to 0$ as $|\omega| \to 0$, indicating a free impurity at low energies.

4.4. Results and discussion

We now turn to our full NRG results for a magnetic impurity embedded in the TBG host. The impurity is taken to be of Anderson type (Eq. 4.13), and the BM model is used for the host (Eq. 4.6). The observables of primary interest are the temperature-dependence of the entropy $S_{\mathrm{imp}}(T)$, and the energy-resolved impurity spectral function $A(\omega)$ at $T = 0$, for TBG systems with different twist angles – see Fig. 4.4. The most dramatic changes are observed in the vicinity of the magic angle at $\theta = 1.05^\circ$, and this is where we focus our discussion. The physical quantities we calculate reveal a complex RG flow in the system, illustrated in Fig. 4.5. The physics precisely at the magic angle is also investigated in detail, and the dependence of the Kondo temperature on microscopic parameters is extracted – see Fig. 4.6.

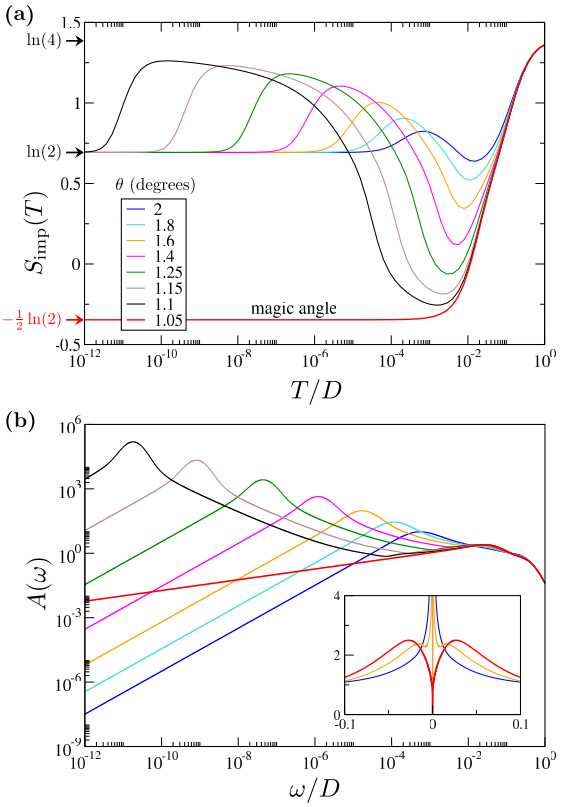

Figure 4.4: NRG results for an Anderson impurity in the TBG host material described by the BM model, at various twist angles θ approaching the magic angle at $\theta = 1.05°$. (a) Impurity entropy $S_{\rm imp}(T)$ vs temperature T; and (b) Impurity spectral function $A(\omega)$ vs energy ω at $T = 0$. Inset shows low-energy spectral details on a linear scale for representative cases approaching the magic angle. All plots shown for $U_d = 0.4D$, $\epsilon_d = -U_d/2$ and $g = 0.2D$, with D the TBG bandwidth.

Consider first the entropy flows presented in Fig. 4.4(a). At the highest temperatures $T \sim D$, the impurity has four thermally populated configurations (empty, doubly-occupied, and up/down spin states) and the entropy for all systems is therefore ln(4) in this limit. On the scale $T \sim U$ the empty and doubly-occupied impurity configurations become thermally inaccessible and only the local moment states of the impurity survive. Note that this high-T charge-freezing crossover is absent in the Kondo model, which features only the two impurity spin states from the outset. Far away from the magic angle, where the low-energy TBG DoS is dominated by the linear pseudogap of the Dirac cone, the Kondo effect is inoperative and the impurity spin degrees of freedom remain unscreened down to $T = 0$. The impurity entropy therefore saturates at the LM value of ln(2). This is the basic picture for the blue line in Fig. 4.4(a) obtained for twist angle $\theta = 2°$. In the opposite limit, when the system is tuned to the magic angle $\theta = 1.05°$ the impurity physics is dominated by the

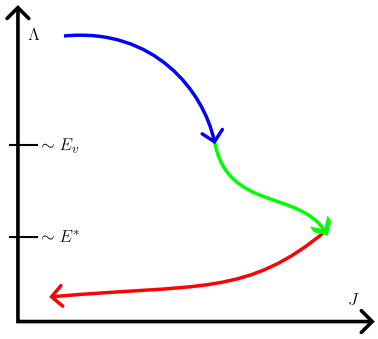

Figure 4.5: Near the magic angle, the TBG host DoS has a compound structure. At high energies Λ, the power-law diverging DoS associated with the HO-vHs generates a rapid RG flow towards strong coupling – blue arrow. On the scale of E_v the DoS crosses over to logarithmic vHs – green arrow. Below E_v the Dirac cone pseudogap dominates the DoS and $J(\Lambda)$ begins to decrease again as the system flows back towards the free local moment regime on an emergent scale E^*. The color-coding is the same as that in Fig. 4.3.

power-law divergence in the low-energy DoS of TBG. The physics in this case is effectively that of the power-law Kondo model discussed in the previous section. Since $\rho(\omega) \sim |\omega|^{-1/4}$, the entropy saturates to $-\frac{1}{2}\ln(2)$ for $T \ll T_K$, where the Kondo scale T_K itself is strongly enhanced. This is precisely what we observe for the red line in Fig. 4.4(a).

However, the situation is much more complex for twist angles close to (but not at) the magic angle. To understand the full RG flow in this intermediate regime, consider Fig. 4.5, together with the fixed point discussion in Sec. 4.3.4 and the RG flow diagrams in Fig. 4.3. Note that the same color-coding is used in Figs. 4.3 and 4.5.

Near the magic angle, the TBG host DoS has a compound structure featuring multiple elements, each of which corresponding to a different limiting Kondo problem. At high energies, the system shows behavior that is characteristic of the HO-vHs, denoted in blue in Fig. 4.5. This behavior crosses over to that of a standard logarithmic vHs on the scale of E_v, denoted in green. Far below this scale, the linear vanishing pseudogap DoS of the Dirac cone emerges, denoted in red. Depending on the energy window, the RG flow will therefore be controlled by the different regimes depicted in Fig. 4.3.

This RG flow is reflected in the temperature dependence of the entropy. After the charge degrees of freedom are frozen out on the high-temperature scale of $T \sim U$ and the impurity entropy reaches $\sim \ln(2)$ characteristic of the LM regime, the system then rapidly flows towards $\mathrm{SSC}_{\mathrm{HO}}$ on further reducing the temperature. On this trajectory, the effective coupling strength $J(\Lambda)$ grows as the energy scale Λ decreases, and the entropy approaches $S_{\mathrm{imp}} = -\frac{1}{2}\ln 2$. However, at the scale E_v the physics of the logarithmic vHs takes over and the system starts to flow towards the regular SC fixed

point with $S_{\rm imp} = 0$. The running coupling $J(\Lambda)$ continues to increases. But on the 'other side' of the vHs in energy space, as the temperature is further decreased, the effect of the low-energy pseudogap DoS begins to dominate. Interestingly though, at this point in the RG flow the system already has a very strong coupling strength $J(\Lambda)$, which puts the system close to the unstable $\mathrm{SSC}_{\rm Dirac}$ fixed point. The entropy therefore 'overshoots' up to ln(4) characteristic of this fixed point. The ultimate RG flow on the lowest energy scales is therefore between $\mathrm{SSC}_{\rm Dirac}$ and the stable LM fixed point of the pseudogap Kondo problem, with a residual $T = 0$ entropy of ln(2). The ground state is an unscreened local moment with ln(2) entropy in all cases except when precisely at the magic angle (where $E_\nu = 0$ such that this final part of the flow towards LM is omitted). Our NRG results for the entropy show that the final low-temperature flow between $\mathrm{SSC}_{\rm Dirac}$ and LM is controlled by an emergent energy scale $E^* \sim |E_\nu|^3$. As we get closer to the magic angle, the E_ν scale reduces and the lines fold progressively onto that of the red line for the magic angle itself. The E^* scale rapidly becomes very small. This gives a finite window in twist angle over which magic angle physics can be observed at intermediate temperatures.

The same RG flow is demonstrated by the $T = 0$ spectral function for the impurity $A(\omega)$, which we plot in Fig. 4.4(b) for the same systems. On the lowest energy scales $|\omega| \ll E^*$, we find $A(\omega) \sim |\omega|$ characteristic of the linear pseudogap Kondo model, for all cases except when precisely at the magic angle. This is because the physics here is controlled by the Dirac cone and the resulting RG flow toward the LM fixed point. By contrast, at the magic angle, the enhanced DoS leads to strong coupling physics and a flow towards the $\mathrm{SSC}_{\rm HO}$ fixed point for all $|\omega| \ll T_K$, yielding $A(\omega) \sim |\omega|^{1/4}$ (red line). As the magic angle is approached, the E_ν scale diminishes and so the spectrum progressively folds onto the magic angle result, see e.g. black line for $\theta = 1.1^\circ$ in Fig. 4.4(b). The most prominent feature of the impurity spectral function is however the dramatic peak on the scale of E^* (note the log scale), which characterizes the flow between $\mathrm{SSC}_{\rm Dirac}$ and LM fixed points. This is highlighted in the inset to Fig. 4.4(b) which compares on a linear scale the magic angle result (red line) to systems at $\theta = 1.6^\circ$ (orange) and 2° (blue). The rapid change in position and intensity of this spectral peak on nearing the magic angle demonstrates that quantum impurities are highly sensitive probes of magic angle physics in TBG systems.

In Fig. 4.6 we turn to an analysis of NRG results for systems at the magic angle itself. In the main panel (top) we plot the impurity entropy $S_{\rm imp}(T)$ for impurities of either Anderson type (Eq. 4.13, points) or Kondo type (Eq. 4.14, lines), for different impurity-host couplings.

At the highest temperatures $T \sim D$, the Anderson impurity again shows ln(4) entropy for the four quasi-degenerate impurity states. At lower temperatures $T \sim U$, the charge configurations on the impurity in the Anderson model are frozen out and only the local moment spin states survive, giving ln(2) entropy. In this regime the

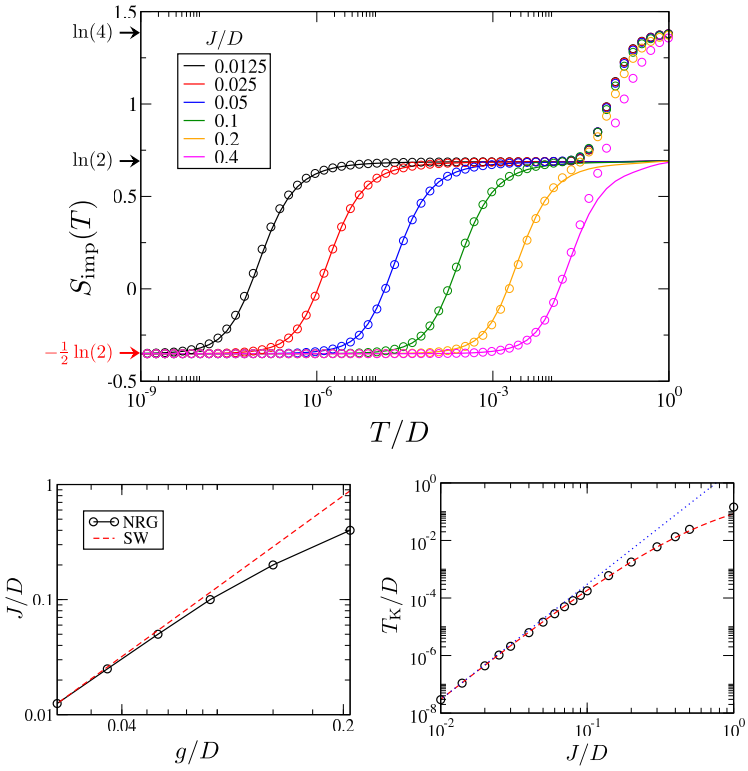

Figure 4.6: NRG results for an impurity embedded in magic angle TBG. Main panel: Entropy $S_{\rm imp}$ vs T for Anderson and Kondo impurities (points and lines respectively) for different impurity-host couplings. For a given Kondo J, the low temperature physics of an Anderson model with fixed $U = 0.4D$ is fit by tuning g. The relationship between J and g is shown in the lower-left inset (points), comparing with the SW result (red dashed line). The evolution of T_K with J is shown in the lower-right inset (points), comparing with Eq. 4.25 (red dashed line) and its small-J asymptote (blue dotted line). T_K is extracted numerically from NRG results for the entropy, defined in practice via $S_{\rm imp}(T = T_K) = 0$.

system is close to the LM fixed point. RG flow towards the SSC_{HO} strong coupling fixed point results in a crossover in the entropy on the scale of the Kondo temperature $T \sim T_K$ to $S_{\rm imp} = -\frac{1}{2}\ln(2)$. This remains the $T = 0$ residual impurity entropy for TBG systems at the magic angle. However, the Kondo scale itself varies with the impurity-host coupling, as seen in the main panel of Fig. 4.6 by the evolution of the different lines. For good scale separation $T_K \ll U$, we see clear two-stage behavior, with distinct crossovers to and from the LM fixed point in the Anderson model. However, given the strongly enhanced T_K at the magic angle, such a scale separation may not be in evidence in practice (see e.g. pink and orange lines in Fig. 4.6 which show a more or less direct crossover in the entropy from $\ln(4)$ to $-\frac{1}{2}\ln(2)$; or indeed the cases close to the magic angle in Fig. 4.4).

By contrast, the Kondo impurity features only the local moment spin configurations

and hence has a ln(2) entropy at high temperatures $T \sim D$. The Kondo scale generated by finite antiferromagnetic exchange coupling J results in the same crossover to the SSC_{HO} fixed point, with the same $T = 0$ residual entropy of $-\frac{1}{2}\ln(2)$. Indeed, RG arguments imply [188] that the physics of the Anderson and Kondo models for $T \ll U$ should be identical, providing the effective Kondo coupling J is chosen appropriately for a given U and g of the Anderson model. To verify this Anderson-Kondo mapping in the magic-angle TBG setting, in Fig. 4.6 we considered Kondo models with different J and then fit Anderson models to match the low-temperature physics by tuning g at fixed U. In such a way, the Kondo and Anderson models have the same Kondo temperature T_K. The precise agreement in the universal regime confirms that at particle-hole symmetry the effective Kondo model is a faithful description of the more microscopic Anderson model.

The Anderson-Kondo mapping can be performed perturbatively via the approximate SW transformation [188, 216] as described in Sec. 4.3. The exact relationship between J and g as extracted from our NRG results is shown in the lower left panel of Fig. 4.6 as the circle points. The SW result (red dashed line) is seen to work well when the bare coupling of the underlying Anderson model is small, $g \ll U$ (small T_K regime). Away from this limit, NRG results show that the Kondo model is still the correct low-energy effective model, but that non-perturbative techniques must be used to obtain the correct effective model parameters [217]. The evolution of the numerically-extracted Kondo temperature as a function of the effective J is shown in the lower right panel of Fig. 4.6 (points), and is compared with the analytic result for the Kondo model Eq. 4.25 (red dashed line). The blue dotted line is the asymptotic small-J limit of this expression, $T_K \sim (4\rho_0 J)^{1/\alpha}$.

Our full NRG results for an impurity in magic angle TBG therefore confirm the analytic predictions of the previous sections. For a comparison with results for an impurity coupled to a standard logarithmic vHs, see Appendix 4.6.3.

Finally, we comment on the role of potential scattering and particle-hole symmetry breaking. In the above analysis we have for simplicity neglected particle-hole asymmetry in the TBG host DoS by employing the symmetric BM model. However, we believe this approximation is well-justified and does not affect the presented results. Although in principle particle-hole asymmetry can lead to Kondo screening in the linear pseudogap case [194] relevant to the low-energy Dirac cone in TBG away from the magic angle, the singlet-doublet quantum phase transition arises only at very strong asymmetry. In practice, the relatively small particle-hole symmetry breaking in TBG means that the impurity problem is far away from the asymmetric strong coupling Kondo phase. Within the doublet local moment phase, particle-hole asymmetry is RG irrelevant and can be safely ignored. We have also assumed that the impurity itself is particle-hole symmetric ($\epsilon_d = -U_d/2$ in the Anderson model, or $V = 0$ in the Kondo model). Relaxing this condition induces potential scattering in

the TBG host. Very strong deviations away from the half-filled Anderson impurity are required to destroy the local moment ground state (the resulting asymmetric Kondo strong coupling state is continuously connected to the trivial empty orbital state of the impurity). In this regime, the mapping to the Kondo model breaks down (the large value of V in the Kondo model required for Kondo screening is unphysical). Therefore, we argue that the results presented above are generic for a local moment impurity embedded in a TBG host material.

4.5. Conclusions

In this paper, we have studied the physics of a single magnetic impurity in TBG at, and close to, the magic angle. We find a surprisingly rich range of behavior, rooted in the unique evolution of the TBG density of states. It is interesting to note that there is no Kondo screened ground state in general, only at the magic angle. However, the signatures at finite temperature relevant to experiment show highly nontrivial structure due to the interplay between van Hove and Dirac physics on the level of a strongly correlated quantum impurity problem. Close to the magic angle, the TBG host density of states at different energy scales yields different limits of paradigmatic Kondo models – from logarithmic and power-law diverging Kondo to pseudogap vanishing Kondo. The subtle renormalization group flow between these limits shows up in the temperature and energy dependence of physical observables.

The behavior we uncover should be detectable in STM experiments. Indeed we argue that the impurity response in TBG gives a very clear signature of magic angle physics. Magnetic impurities may therefore prove useful as highly sensitive *in-situ* probes for moiré materials.

An interesting direction of future research is the role of the RKKY interaction between multiple magnetic impurities in TBG, and how it competes with the Kondo effect of individual impurities near the magic angle.

Although van Hove-boosted Kondo physics may be observable in other systems (including 3d bulk metals [243, 244] with magnetic impurities), we note that TBG stands out as a uniquely tunable platform. Furthermore, TBG also allows one to study the complex interplay of these effects with Dirac physics.

Acknowledgments

We thank S. Polla, V. Cheianov, L. Classen, A. Chubukov, and L. Fu for helpful discussions. this work is part of the D-ITP consortium, a program of the Netherlands Organisation for Scientific Research (NWO) that is funded by the Dutch Ministry of

Education, Culture and Science (OCW). DOO acknowledges the support from the Netherlands Organization for Scientific Research (NWO/OCW) and from the European Research Council (ERC) under the European Union's Horizon 2020 research and innovation programme. AKM acknowledges funding from the Irish Research Council through the Laureate Award 2017/2018 grant IRCLA/2017/169.

4.6. Appendix

4.6.1. Locating saddle point positions in the particle-hole symmetric BM model

To locate the saddle points in the Brillouin zone, we require gradients of the energy. The flat bands make it imperative that the first derivative is computed very accurately, and this means that we must avoid crude finite difference methods for numerical derivatives of the energy. This problem can be addressed by utilizing our analytical access to the Hamiltonian itself, and implementing the Hellman-Feynman theorem,

$$\frac{\partial E}{\partial k^i} = \langle \psi_k | \frac{\partial H}{\partial k^i} | \psi_k \rangle , \tag{4.26}$$

where ψ_k is the wavefunction of the lowest positive energy band at momentum $\boldsymbol{k}$. A more extended analysis of this method has been introduced recently in [245].

The saddle point is found by minimizing the value of $\left(\partial_{k_x}\epsilon_{\boldsymbol{k}}\right)^2 + \left(\partial_{k_y}\epsilon_{\boldsymbol{k}}\right)^2$ over the Brillouin zone vectors, by using the conjugate gradient method. The coefficients for the local energy dispersion are then calculated along the principal directions of the saddle point. These directions are given by the eigenvectors of the Hessian matrix, and are in general different from the k_x and k_y of the Brillouin zone. Derivatives are convenient to compute along the natural Brillouin zone directions, however. The trick to overcome this is to note that a matrix formed from n derivatives of a scalar transforms like a rank-n tensor. Then the tensor transformation rule can be used with a covariant Jacobian to obtain the coefficients along the rotated axes.

One subtlety is that for angles very close to the magic angle, there are secondary vHs points at other locations in the Brillouin zone than those indicated in Fig. 4.2a. For the purposes of the Kondo effect, we have only considered the one with the largest spectral weight, since this is found to dominate the results of our NRG calculations. This is done by computing the local dispersion coefficients α and β at each of the saddle points, and picking the one with the largest value of $\frac{1}{\sqrt{\alpha\beta}}$.

4.6.2. Mapping from TBG density of states to the NRG Wilson chain

The TBG DoS away from the magic angle has two qualitative features: the linear-pseudogap Dirac cone at low energies and the divergence due to the vHs on the scale of E_v. We extract an effective model DoS from analysis of the BM model for different twist angles – see left panels of Fig. 4.7 for the cases explicitly considered in the main text (we have rescaled the energy range in terms of the bandwidth cutoff and normalized the spectrum to unity). This DoS is then discretized logarithmically and mapped to a Wilson chain [220] as described in Sec. 4.3.2. The corresponding Wilson chain hopping parameters are plotted in the right panels of Fig. 4.7. The results show that the different DoS elements can be captured in NRG through the crossover behavior in the functional form of the Wilson chain.

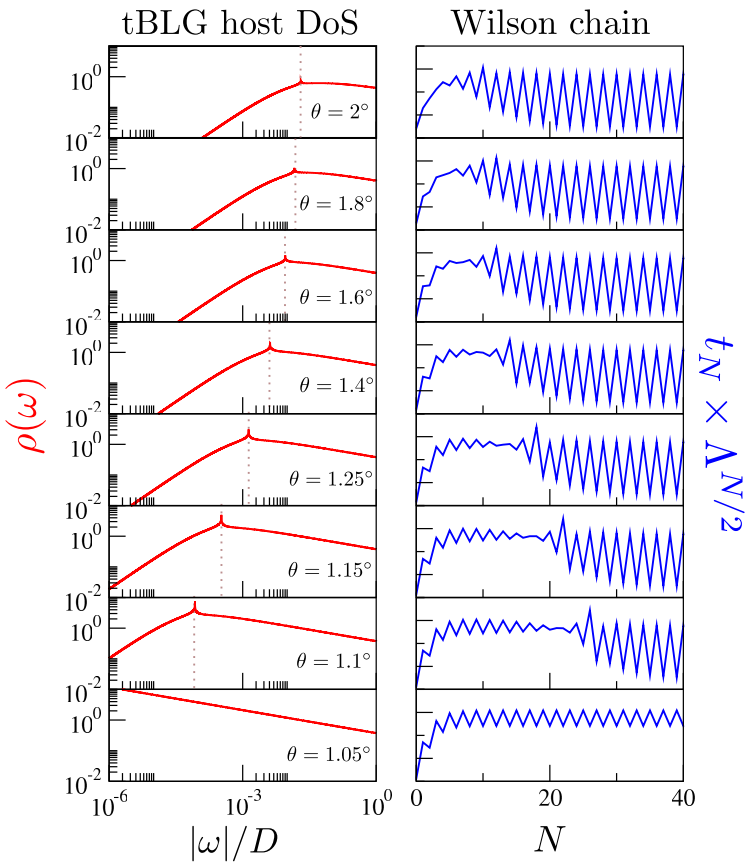

Figure 4.7: Left panels: DoS used in our NRG calculations, obtained from analysis of the effective BM model, for different twist angles θ as used in the main text. Vertical dotted lines show the E_v scale at which the vHs divergence occurs. This scale moves to lower energies as the magic angle is approached. Right panels: corresponding Wilson chain coefficients.

4.6.3. NRG calculations for an impurity coupled to a conventional log-vHs host

In Fig. 4.8 we provide reference NRG calculations for a Kondo impurity coupled to a pure log-diverging DoS. This gives a useful comparison to our result for an impurity embedded in the magic-angle TBG system, which has a HO-vHs point and hence a stronger power-law diverging DoS. As predicted from our perturbative scaling (poor man's scaling) results, the system flows towards strong coupling in all cases, in which the impurity is Kondo-screened. The residual entropy at $T = 0$ is seen to be $S_{\text{imp}} = 0$, although this limit is approached logarithmically slowly from below. This is characteristic of the logarithmic DoS. From the scaling with bare coupling strength J in the left panel, the Kondo temperature T_K is seen to be enhanced relative to the metallic case, but substantially suppressed relative to the power-law diverging DoS case. In the right panel, we analyze the behavior of T_K in more detail, comparing NRG results at different J (circle points) with our analytic formula Eq. 4.24 (black line). The results agree almost perfectly. The red dashed line is the asymptotic result at small J, which also does remarkably well compared with exact NRG results.

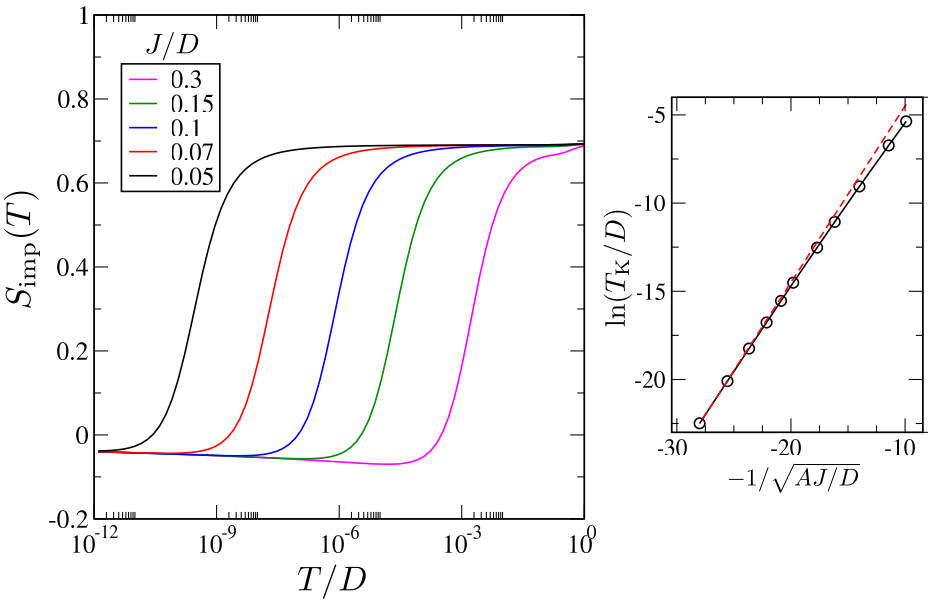

Figure 4.8: Main panel: NRG results for the impurity entropy S_{imp} vs temperature T for different bare coupling strengths J, in a system with a pure log-diverging DoS (standard vHs). Right inset shows the extracted T_K scale (points), compared with Eq. 4.24 (black line) and the asymptotic result $T_K \sim De^{-1/\sqrt{AJ/D}}$ (red dashed line), with $A = a\rho_0 D/2$.

Bibliography

[1] M. Born and R. Oppenheimer, *Zur quantentheorie der molekeln [on the quantum theory of molecules]*, *Annalen der Physik* **389** (1927), no. 20 457–484.

[2] N. W. Ashcroft and N. D. Mermin, *Solid state physics*. Holt, Rinehart and Winston, New York, 1976.

[3] J. M. Luttinger and J. C. Ward, *Ground-state energy of a many-fermion system. ii*, *Physical Review* **118** (1960), no. 5 1417.

[4] G. Baym and L. P. Kadanoff, *Conservation laws and correlation functions*, *Physical Review* **124** (1961), no. 2 287.

[5] D. Pines and P. NoziÈres, *Microscopic theories of the electron liquid*, in *Theory of quantum liquids*, pp. 270–344. CRC Press, 2018.

[6] B. Keimer, S. A. Kivelson, M. R. Norman, S. Uchida, and J. Zaanen, *From quantum matter to high-temperature superconductivity in copper oxides*, *Nature* **518** (2015), no. 7538 179–186.

[7] A. Damascelli, Z. Hussain, and Z.-X. Shen, *Angle-resolved photoemission studies of the cuprate superconductors*, *Reviews of modern physics* **75** (2003), no. 2 473.

[8] J. Zaanen, *Planckian dissipation, minimal viscosity and the transport in cuprate strange metals*, *SciPost Physics* **6** (May, 2019) 061.

[9] D. v. d. Marel, H. Molegraaf, J. Zaanen, Z. Nussinov, F. Carbone, A. Damascelli, H. Eisaki, M. Greven, P. Kes, and M. Li, *Quantum critical behaviour in a high-t c superconductor*, *Nature* **425** (2003), no. 6955 271–274.

[10] B. Michon, C. Berthod, C. W. Rischau, A. Ataei, L. Chen, S. Komiya, S. Ono, L. Taillefer, D. van der Marel, and A. Georges, *Reconciling scaling of the optical conductivity of cuprate superconductors with planckian resistivity and specific heat*, *Nature Communications* **14** (2023), no. 1 3033.

[11] N. E. Hussey, *Phenomenology of the normal state in-plane transport properties of high-tc cuprates*, *Journal of Physics: Condensed Matter* **20** (2008), no. 12 123201.

[12] J. Ayres, M. Berben, M. Čulo, Y.-T. Hsu, E. van Heumen, Y. Huang, J. Zaanen, T. Kondo, T. Takeuchi, J. Cooper, et al., *Incoherent transport across the strange-metal regime of overdoped cuprates*, *Nature* **595** (2021), no. 7869 661–666.

[13] C. Varma, P. B. Littlewood, S. Schmitt-Rink, E. Abrahams, and A. Ruckenstein, *Phenomenology of the normal state of cu-o high-temperature superconductors*, *Physical Review Letters* **63** (1989), no. 18 1996.

[14] A. Ruckenstein and C. M. Varma, *A theory of marginal fermi-liquids*, *Physica C: Superconductivity* **185** (1991) 134–140.

[15] C. Varma, *Towards a theory of the marginal fermi-liquid state*, *Journal of Physics and Chemistry of Solids* **54** (1993), no. 10 1081–1084.

[16] C. M. Varma, Z. Nussinov, and W. Van Saarloos, *Singular or non-fermi liquids*, *Physics Reports* **361** (2002), no. 5-6 267–417.

[17] P. Littlewood and C. Varma, *Phenomenology of the normal and superconducting states of a marginal fermi liquid*, *Journal of applied physics* **69** (1991), no. 8 4979–4984.

[18] S. Sachdev, *Quantum Phase Transitions*. Cambridge University Press, 2 ed., 2011.

[19] J. Maldacena and D. Stanford, *Comments on the Sachdev-Ye-Kitaev model*, *Physical Review D* **94** (Nov., 2016) 106002. arXiv: 1604.07818.

[20] A. Schellekens, *Conformal field theory*, *Lecture Notes. NIKHEF% E/95* (1995).

[21] S. Sachdev and J. Ye, *Gapless spin-fluid ground state in a random quantum heisenberg magnet*, *Physical review letters* **70** (1993), no. 21 3339.

[22] S. Sachdev, *Bekenstein-hawking entropy and strange metals*, *Physical Review X* **5** (2015), no. 4 041025.

[23] Y. Gu, A. Kitaev, S. Sachdev, and G. Tarnopolsky, *Notes on the complex Sachdev-Ye-Kitaev model*, *Journal of High Energy Physics* **2020** (Feb., 2020) 157.

[24] I. Esterlis and J. Schmalian, *Cooper pairing of incoherent electrons: An electron-phonon version of the sachdev-ye-kitaev model*, *Physical Review B* **100** (2019), no. 11 115132.

[25] Y. Wang and A. V. Chubukov, *Quantum phase transition in the yukawa-syk model*, *Physical Review Research* **2** (2020), no. 3 033084.

[26] Y. Wang, *Solvable strong-coupling quantum-dot model with a non-fermi-liquid pairing transition*, *Physical review letters* **124** (2020), no. 1 017002.

[27] L. Classen and A. Chubukov, *Superconductivity of incoherent electrons in the yukawa sachdev-ye-kitaev model*, *Physical Review B* **104** (2021), no. 12 125120.

[28] G.-A. Inkof, K. Schalm, and J. Schmalian, *Quantum critical eliashberg theory, the sachdev-ye-kitaev superconductor and their holographic duals, npj Quantum Materials* **7** (2022), no. 1 56.

[29] G. Pan, W. Wang, A. Davis, Y. Wang, and Z. Y. Meng, *Yukawa-syk model and self-tuned quantum criticality, Physical Review Research* **3** (2021), no. 1 013250.

[30] A. Davis and Y. Wang, *Quantum chaos and phase transition in the yukawa–sachdev-ye-kitaev model, Physical Review B* **107** (2023), no. 20 205122.

[31] L. Grunwald, G. Passetti, and D. M. Kennes, *Dynamical onset of light-induced unconventional superconductivity—a yukawa-sachdev-ye-kitaev study, Communications Physics* **7** (2024), no. 1 79.

[32] W. Choi, O. Tavakol, and Y. B. Kim, *Pairing instabilities of the yukawa-syk models with controlled fermion incoherence, SciPost Physics* **12** (2022), no. 5 151.

[33] A. A. Patel, H. Guo, I. Esterlis, and S. Sachdev, *Universal theory of strange metals from spatially random interactions, Science* **381** (2023), no. 6659 790–793.

[34] D. Valentinis, G. A. Inkof, and J. Schmalian, *Correlation between phase stiffness and condensation energy across the non-fermi to fermi-liquid crossover in the yukawa-sachdev-ye-kitaev model on a lattice, Physical Review Research* **5** (2023), no. 4 043007.

[35] I. Esterlis, H. Guo, A. A. Patel, and S. Sachdev, *Large-n theory of critical fermi surfaces, Physical Review B* **103** (2021), no. 23 235129.

[36] H. Guo, A. A. Patel, I. Esterlis, and S. Sachdev, *Large-n theory of critical fermi surfaces. ii. conductivity, Physical Review B* **106** (2022), no. 11 115151.

[37] H. Guo, S. Sachdev, and A. A. Patel, *Large n theory of critical fermi surfaces iii: Cyclotron resonance and quantum oscillation, arXiv preprint arXiv:2308.01956* (2023).

[38] C. Li, D. Valentinis, A. A. Patel, H. Guo, J. Schmalian, S. Sachdev, and I. Esterlis, *Strange metal and superconductor in the two-dimensional yukawa-sachdev-ye-kitaev model, arXiv preprint arXiv:2406.07608* (2024).

[39] S.-S. Lee, *Low-energy effective theory of fermi surface coupled with u (1) gauge field in 2+ 1 dimensions, Physical Review B—Condensed Matter and Materials Physics* **80** (2009), no. 16 165102.

[40] M. A. Metlitski, D. F. Mross, S. Sachdev, and T. Senthil, *Cooper pairing in non-fermi liquids*, *Physical Review B* **91** (2015), no. 11 115111.

[41] A. V. Chubukov, A. Abanov, Y. Wang, and Y.-M. Wu, *The interplay between superconductivity and non-fermi liquid at a quantum-critical point in a metal*, *Annals of Physics* **417** (2020) 168142.

[42] A. Abanov and A. V. Chubukov, *Interplay between superconductivity and non-fermi liquid at a quantum critical point in a metal. i. the γ model and its phase diagram at t= 0: The case 0< γ< 1*, *Physical Review B* **102** (2020), no. 2 024524.

[43] J.-H. She and J. Zaanen, *Bcs superconductivity in quantum critical metals*, *Physical Review B—Condensed Matter and Materials Physics* **80** (2009), no. 18 184518.

[44] V. Ambegaokar and A. Baratoff, *Tunneling between superconductors*, *Physical review letters* **10** (1963), no. 11 486.

[45] D. Chowdhury, A. Georges, O. Parcollet, and S. Sachdev, *Sachdev-Ye-Kitaev Models and Beyond: A Window into Non-Fermi Liquids*, *arXiv:2109.05037 [cond-mat, physics:hep-th, physics:quant-ph]* (Sept., 2021). arXiv: 2109.05037.

[46] A. Chen, R. Ilan, F. de Juan, D. I. Pikulin, and M. Franz, *Quantum holography in a graphene flake with an irregular boundary*, *Phys. Rev. Lett.* **121** (Jul, 2018) 036403.

[47] A. Altland and M. R. Zirnbauer, *Nonstandard symmetry classes in mesoscopic normal-superconducting hybrid structures*, *Physical Review B* **55** (1997), no. 2 1142.

[48] L. Fidkowski and A. Kitaev, *Effects of interactions on the topological classification of free fermion systems*, *Physical Review B—Condensed Matter and Materials Physics* **81** (2010), no. 13 134509.

[49] L. Fidkowski and A. Kitaev, *Topological phases of fermions in one dimension*, *Physical Review B—Condensed Matter and Materials Physics* **83** (2011), no. 7 075103.

[50] A. M. García-García and J. J. Verbaarschot, *Spectral and thermodynamic properties of the sachdev-ye-kitaev model*, *Physical Review D* **94** (2016), no. 12 126010.

[51] J. Behrends, J. H. Bardarson, and B. Béri, *Tenfold way and many-body zero modes in the sachdev-ye-kitaev model*, *Physical Review B* **99** (2019), no. 19 195123.

[52] Y.-Z. You, A. W. Ludwig, and C. Xu, *Sachdev-ye-kitaev model and thermalization on the boundary of many-body localized fermionic symmetry-protected topological states*, *Physical Review B* **95** (2017), no. 11 115150.

[53] M. Fremling and L. Fritz, *A bipartite variant of the Sachdev-Ye-Kitaev model from a strained Kitaev honeycomb model*, *arXiv:2105.06119 [cond-mat]* (May, 2021). arXiv: 2105.06119.

[54] A. Kitaev, *Anyons in an exactly solved model and beyond*, *Annals of Physics* **321** (2006), no. 1 2–111.

[55] S. Trebst and C. Hickey, *Kitaev materials*, *Physics Reports* **950** (2022) 1–37.

[56] A. Banerjee, J. Yan, J. Knolle, C. A. Bridges, M. B. Stone, M. D. Lumsden, D. G. Mandrus, D. A. Tennant, R. Moessner, and S. E. Nagler, *Neutron scattering in the proximate quantum spin liquid α-rucl3*, *Science* **356** (2017), no. 6342 1055–1059.

[57] M. Fremling, M. Haque, and L. Fritz, *Bipartite sachdev-ye-kitaev model: Conformal limit and level statistics*, *Physical Review D* **105** (mar, 2022).

[58] S. Xu, L. Susskind, Y. Su, and B. Swingle, *A Sparse Model of Quantum Holography*, Aug., 2020. Number: arXiv:2008.02303 arXiv:2008.02303 [cond-mat, physics:hep-th, physics:quant-ph].

[59] A. M. Garcia-Garcia, Y. Jia, D. Rosa, and J. J. Verbaarschot, *Sparse Sachdev-Ye-Kitaev model, quantum chaos, and gravity duals*, *Physical Review D* **103** (May, 2021) 106002.

[60] E. Cáceres, A. Misobuchi, and R. Pimentel, *Sparse syk and traversable wormholes*, *Journal of High Energy Physics* **2021** (2021), no. 11 1–32.

[61] E. Cáceres, T. Guglielmo, B. Kent, and A. Misobuchi, *Out-of-time-order correlators and lyapunov exponents in sparse syk*, *Journal of High Energy Physics* **2023** (2023), no. 11 1–40.

[62] A. Kitaev and S. J. Suh, *The soft mode in the sachdev-ye-kitaev model and its gravity dual*, *Journal of High Energy Physics* **2018** (2018), no. 5 1–68.

[63] J. Maldacena, D. Stanford, and Z. Yang, *Conformal symmetry and its breaking in two-dimensional nearly anti-de sitter space*, *Progress of Theoretical and Experimental Physics* **2016** (2016), no. 12 12C104.

[64] A. Almheiri and J. Polchinski, *Models of ads2 backreaction and holography*, *Journal of High Energy Physics* **2015** (2015), no. 11 1–19.

[65] G. Sárosi, *Ads _2 holography and the syk model*, *arXiv preprint arXiv:1711.08482* (2017).

[66] J. Maldacena, *The large-n limit of superconformal field theories and supergravity*, *International journal of theoretical physics* **38** (1999), no. 4 1113–1133.

[67] S. S. Gubser, I. R. Klebanov, and A. M. Polyakov, *Gauge theory correlators from non-critical string theory*, *Physics Letters B* **428** (1998), no. 1-2 105–114.

[68] E. Witten, *Anti de sitter space and holography*, *arXiv preprint hep-th/9802150* (1998).

[69] J. Zaanen, Y. Liu, Y.-W. Sun, and K. Schalm, *Holographic duality in condensed matter physics*. Cambridge University Press, 2015.

[70] J. D. Bekenstein, *Black holes and entropy*, *Physical Review D* **7** (1973), no. 8 2333.

[71] T. Faulkner, H. Liu, J. McGreevy, and D. Vegh, *Emergent quantum criticality, fermi surfaces, and ads 2*, *Physical Review D—Particles, Fields, Gravitation, and Cosmology* **83** (2011), no. 12 125002.

[72] T. Faulkner, N. Iqbal, H. Liu, J. McGreevy, and D. Vegh, *Holographic non-fermi-liquid fixed points*, *Philosophical Transactions of the Royal Society A: Mathematical, Physical and Engineering Sciences* **369** (2011), no. 1941 1640–1669.

[73] J. Maldacena, S. H. Shenker, and D. Stanford, *A bound on chaos*, *Journal of High Energy Physics* **2016** (Aug., 2016) 106. arXiv: 1503.01409.

[74] S. H. Shenker and D. Stanford, *Black holes and the butterfly effect*, *Journal of High Energy Physics* **2014** (2014), no. 3 1–25.

[75] S. H. Shenker and D. Stanford, *Stringy effects in scrambling*, *Journal of High Energy Physics* **2015** (2015), no. 5 1–34.

[76] D. Stanford, *Many-body chaos at weak coupling*, *Journal of High Energy Physics* **2016** (Oct., 2016) 9. arXiv: 1512.07687.

[77] S. Grozdanov, K. Schalm, and V. Scopelliti, *Black hole scrambling from hydrodynamics*, *Physical Review Letters* **120** (2018), no. 23 231601.

[78] D. Bagrets, A. Altland, and A. Kamenev, *Sachdev–ye–kitaev model as liouville quantum mechanics*, *Nuclear Physics B* **911** (2016) 191–205.

[79] A. Romero-Bermúdez, K. Schalm, and V. Scopelliti, *Regularization dependence of the otoc. which lyapunov spectrum is the physical one?*, *Journal of High Energy Physics* **2019** (2019), no. 7 1–32.

[80] J. Maldacena, *Eternal black holes in anti-de sitter, Journal of High Energy Physics* **2003** (2003), no. 04 021.

[81] J. Zaanen, *Why the temperature is high, Nature* **430** (2004), no. 6999 512–513.

[82] A. C. Neto, F. Guinea, N. M. Peres, K. S. Novoselov, and A. K. Geim, *The electronic properties of graphene, Reviews of modern physics* **81** (2009), no. 1 109.

[83] N. F. Q. Yuan, H. Isobe, and L. Fu, *Magic of high-order van Hove singularity, Nature Communications* **10** (Dec., 2019) 5769.

[84] N. F. Q. Yuan and L. Fu, *Classification of critical points in energy bands based on topology, scaling, and symmetry, Phys. Rev. B* **101** (Mar, 2020) 125120.

[85] A. Chandrasekaran, A. Shtyk, J. J. Betouras, and C. Chamon, *Catastrophe theory classification of fermi surface topological transitions in two dimensions, Physical Review Research* **2** (2020), no. 1 013355.

[86] V. Zakharov, A. M. Bozkurt, A. Akhmerov, and D. Oriekhov, *Landau quantization near generalized van hove singularities: Magnetic breakdown and orbit networks, Physical Review B* **109** (2024), no. 8 L081103.

[87] L. Classen and J. J. Betouras, *High-order van hove singularities and their connection to flat bands, arXiv preprint arXiv:2405.20226* (2024).

[88] R. Markiewicz and B. Giessen, *Correlation of tc with structure in the density of states in the new high-tc superconductors, Physica C: Superconductivity* **160** (1989), no. 5-6 497–504.

[89] R. S. Markiewicz, B. Singh, C. Lane, and A. Bansil, *Investigating the cuprates as a platform for high-order van hove singularities and flat-band physics, Communications Physics* **6** (2023), no. 1 292.

[90] I. Paul and M. Civelli, *Exceptional van hove singularities in pseudogapped metals, Physical Review B* **107** (2023), no. 20 L201121.

[91] D. K. Efetov, *Towards inducing superconductivity into graphene.* Columbia University, 2014.

[92] Y. Cao, V. Fatemi, S. Fang, K. Watanabe, T. Taniguchi, E. Kaxiras, and P. Jarillo-Herrero, *Unconventional superconductivity in magic-angle graphene superlattices, Nature* **556** (Apr., 2018) 43–50.

[93] Y. Cao, V. Fatemi, A. Demir, S. Fang, S. L. Tomarken, J. Y. Luo, J. D. Sanchez-Yamagishi, K. Watanabe, T. Taniguchi, E. Kaxiras, R. C. Ashoori, and P. Jarillo-Herrero, *Correlated insulator behaviour at half-filling in magic-angle graphene superlattices, Nature* **556** (Apr., 2018) 80–84.

[94] M. Oh, K. P. Nuckolls, D. Wong, R. L. Lee, X. Liu, K. Watanabe, T. Taniguchi, and A. Yazdani, *Evidence for unconventional superconductivity in twisted bilayer graphene*, *Nature* **600** (2021), no. 7888 240–245.

[95] S. Lisi, X. Lu, T. Benschop, T. A. de Jong, P. Stepanov, J. R. Duran, F. Margot, I. Cucchi, E. Cappelli, A. Hunter, et al., *Observation of flat bands in twisted bilayer graphene*, *Nature Physics* **17** (2021), no. 2 189–193.

[96] R. Shankar, *Renormalization group for interacting fermions in d> 1*, *Physica A: Statistical Mechanics and its Applications* **177** (1991), no. 1-3 530–536.

[97] R. Shankar, *Renormalization-group approach to interacting fermions*, *Reviews of Modern Physics* **66** (1994), no. 1 129.

[98] J. Polchinski, *Effective field theory and the fermi surface*, *arXiv preprint hep-th/9210046* (1992).

[99] P. Coleman, *Introduction to many-body physics*. Cambridge University Press, 2015.

[100] B. Mihaila, *Lindhard function of a d-dimensional fermi gas*, *arXiv preprint arXiv:1111.5337* (2011).

[101] L. Classen, A. V. Chubukov, C. Honerkamp, and M. M. Scherer, *Competing orders at higher-order van hove points*, *Phys. Rev. B* **102** (Sep, 2020) 125141.

[102] J. Alfonsi, *Moiré patterns and commensurability in rotated graphene bilayers*, 2013.

[103] R. Bistritzer and A. H. MacDonald, *Moiré bands in twisted double-layer graphene*, *Proceedings of the National Academy of Sciences* **108** (2011), no. 30 12233–12237.

[104] A. Shankar, M. Fremling, S. Plugge, and L. Fritz, *Lyapunov exponents in a sachdev-ye-kitaev-type model with population imbalance in the conformal limit and beyond*, *Physical Review D* **108** (2023), no. 9 094039.

[105] J. Maldacena and X.-L. Qi, *Eternal traversable wormhole*, *arXiv preprint arXiv:1804.00491* (2018).

[106] A. Shankar, D. Oriekhov, A. K. Mitchell, and L. Fritz, *Kondo effect in twisted bilayer graphene*, *Physical Review B* **107** (2023), no. 24 245102.

[107] Y. Chang, J. Yi, A.-K. Wu, F. B. Kugler, E. Andrei, D. Vanderbilt, G. Kotliar, and J. Pixley, *Vacancy-induced tunable kondo effect in twisted bilayer graphene*, *arXiv preprint arXiv:2312.09286* (2023).

[108] D. Chowdhury, A. Georges, O. Parcollet, and S. Sachdev, *Sachdev-ye-kitaev models and beyond: Window into non-fermi liquids, Rev. Mod. Phys.* **94** (Sep, 2022) 035004.

[109] V. Rosenhaus, *An introduction to the syk model, Journal of Physics A: Mathematical and Theoretical* **52** (2019), no. 32 323001.

[110] M. Franz and M. Rozali, *Mimicking black hole event horizons in atomic and solid-state systems, Nature Reviews Materials* **3** (2018), no. 12 491–501.

[111] A. A. Patel and S. Sachdev, *Quantum chaos on a critical Fermi surface, Proceedings of the National Academy of Sciences* **114** (Feb., 2017) 1844–1849. arXiv: 1611.00003.

[112] M. Tikhanovskaya, S. Sachdev, and A. A. Patel, *Maximal quantum chaos of the critical fermi surface, arXiv preprint arXiv:2202.01845* (2022).

[113] J. Polchinski and V. Rosenhaus, *The Spectrum in the Sachdev-Ye-Kitaev Model, Journal of High Energy Physics* **2016** (Apr., 2016) 1–25. arXiv: 1601.06768.

[114] D. I. Pikulin and M. Franz, *Black hole on a chip: Proposal for a physical realization of the sachdev-ye-kitaev model in a solid-state system, Phys. Rev. X* **7** (Jul, 2017) 031006.

[115] A. Chew, A. Essin, and J. Alicea, *Approximating the sachdev-ye-kitaev model with majorana wires, Phys. Rev. B* **96** (Sep, 2017) 121119.

[116] O. Can, E. M. Nica, and M. Franz, *Charge transport in graphene-based mesoscopic realizations of Sachdev-Ye-Kitaev models, Physical Review B* **99** (Jan., 2019) 045419. arXiv: 1808.06584.

[117] I. Danshita, M. Hanada, and M. Tezuka, *Creating and probing the sachdev–ye–kitaev model with ultracold gases: Towards experimental studies of quantum gravity, Progress of Theoretical and Experimental Physics* **2017** (2017), no. 8.

[118] C. Wei and T. A. Sedrakyan, *Optical lattice platform for the sachdev-ye-kitaev model, Physical Review A* **103** (2021), no. 1 013323.

[119] S. A. Hartnoll and A. P. Mackenzie, *Planckian dissipation in metals*, 2021.

[120] A. A. Patel, J. McGreevy, D. P. Arovas, and S. Sachdev, *Magnetotransport in a Model of a Disordered Strange Metal, Physical Review X* **8** (May, 2018) 021049.

[121] S. A. Hartnoll and A. P. Mackenzie, *Colloquium: Planckian dissipation in metals, Reviews of Modern Physics* **94** (2022), no. 4 041002.

[122] Y. Gu and A. Kitaev, *On the relation between the magnitude and exponent of otocs*, *Journal of High Energy Physics* **2019** (2019), no. 2 1–21.

[123] A. I. Larkin and Y. N. Ovchinnikov, *Quasiclassical method in the theory of superconductivity*, *Sov Phys JETP* **28** (1969), no. 6 1200–1205.

[124] K. Hashimoto, K. Murata, and R. Yoshii, *Out-of-time-order correlators in quantum mechanics*, *Journal of High Energy Physics* **2017** (Oct., 2017) 138. arXiv: 1703.09435.

[125] B. Kobrin, Z. Yang, G. D. Kahanamoku-Meyer, C. T. Olund, J. E. Moore, D. Stanford, and N. Y. Yao, *Many-Body Chaos in the Sachdev-Ye-Kitaev Model*, *Physical Review Letters* **126** (Jan., 2021) 030602. arXiv: 2002.05725.

[126] B. Craps, M. De Clerck, D. Janssens, V. Luyten, and C. Rabideau, *Lyapunov growth in quantum spin chains*, *Physical Review B* **101** (May, 2020) 174313. arXiv: 1908.08059.

[127] É. Lantagne-Hurtubise, S. Plugge, O. Can, and M. Franz, *Diagnosing quantum chaos in many-body systems using entanglement as a resource*, *Physical Review Research* **2** (2020), no. 1 013254.

[128] J. Kim, I. R. Klebanov, G. Tarnopolsky, and W. Zhao, *Symmetry breaking in coupled SYK or tensor models*, *Phys. Rev. X* **9** (May, 2019) 021043.

[129] S. Sahoo, É. Lantagne-Hurtubise, S. Plugge, and M. Franz, *Traversable wormhole and Hawking-Page transition in coupled complex SYK models*, *Physical Review Research* **2** (2020), no. 4 043049, [arXiv:2006.06019].

[130] D. Chowdhury, Y. Werman, E. Berg, and T. Senthil, *Translationally Invariant Non-Fermi-Liquid Metals with Critical Fermi Surfaces: Solvable Models*, *Physical Review X* **8** (July, 2018) 031024.

[131] D. J. Gross and V. Rosenhaus, *A Generalization of Sachdev-Ye-Kitaev*, *Journal of High Energy Physics* **2017** (Feb., 2017) 93. arXiv: 1610.01569.

[132] E. Marcus and S. Vandoren, *A new class of SYK-like models with maximal chaos*, *Journal of High Energy Physics* **2019** (2019), no. 1 166.

[133] O. Parcollet and A. Georges, *Non-Fermi-liquid regime of a doped Mott insulator*, *Physical Review B* **59** (Feb., 1999) 5341–5360.

[134] S. Plugge, É. Lantagne-Hurtubise, and M. Franz, *Revival dynamics in a traversable wormhole*, *Physical Review Letters* **124** (2020), no. 22 221601, [arXiv:2003.03914].

[135] Y. Chen, H. Zhai, and P. Zhang, *Tunable quantum chaos in the sachdev-ye-kitaev model coupled to a thermal bath*, *Journal of High Energy Physics* **2017** (2017), no. 7 1–28.

[136] P. Gao, D. L. Jafferis, and A. C. Wall, *Traversable Wormholes via a Double Trace Deformation*, *Journal of High Energy Physics* **2017** (2017), no. 12 151, [arXiv:1608.05687].

[137] J. Maldacena, D. Stanford, and Z. Yang, *Diving into traversable wormholes*, *Fortschritte der Physik* **65** (2017), no. 5 1700034, [arXiv:1704.05333].

[138] J. Maldacena, A. Milekhin, and F. Popov, *Traversable wormholes in four dimensions*, 2020.

[139] D. Bak, C. Kim, and S.-H. Yi, *Bulk View of Teleportation and Traversable Wormholes*, *Journal of High Energy Physics* **2018** (2018), no. 8 140, [arXiv:1805.12349].

[140] P. Gao and H. Liu, *Regenesis and quantum traversable wormholes*, *Journal of High Energy Physics* **2019** (2019), no. 10 48, [arXiv:1810.01444].

[141] Z. Fu, B. Grado-White, and D. Marolf, *Traversable Asymptotically Flat Wormholes with Short Transit Times*, *Classical and Quantum Gravity* **36** (2019), no. 24 245018, [arXiv:1908.03273].

[142] D. Bak, C. Kim, and S.-H. Yi, *Experimental Probes of Traversable Wormholes*, *Journal of High Energy Physics* **2019** (2019), no. 12 5, [arXiv:1907.13465].

[143] X.-L. Qi and P. Zhang, *The Coupled SYK model at Finite Temperature*, *Journal of High Energy Physics* **2020** (2020), no. 5 129, [arXiv:2003.03916].

[144] R. Haenel, S. Sahoo, T. H. Hsieh, and M. Franz, *Traversable wormhole in coupled sachdev-ye-kitaev models with imbalanced interactions*, *Physical Review B* **104** (2021), no. 3 035141.

[145] M. Berenguer, A. Dey, J. Mas, J. Santos-Suárez, and A. V. Ramallo, *Floquet syk wormholes*, *Journal of High Energy Physics* **2024** (2024), no. 6 1–28.

[146] J. Maldacena and A. Milekhin, *SYK wormhole formation in real time*, 2020.

[147] S. Sahoo, E. Lantagne-Hurtubise, S. Plugge, and M. Franz, *Traversable wormhole and Hawking-Page transition in coupled complex SYK models*, *Physical Review Research* **2** (Oct., 2020) 043049.

[148] M. A. Metlitski, D. F. Mross, S. Sachdev, and T. Senthil, *Are non-Fermi-liquids stable to Cooper pairing?*, *Physical Review B* **91** (2015), no. 11 115111, [arXiv:1403.3694].

[149] J.-H. She and J. Zaanen, *BCS Superconductivity in Quantum Critical Metals*, *Physica C: Superconductivity and its Applications* **470** (2010) S911, [arXiv:0905.1225].

[150] S.-S. Zhang and A. V. Chubukov, *Density of states and spectral function of a superconductor out of a quantum-critical metal*, *Physical review letters* **131** (2023), no. 8 086502.

[151] T. Kondo, W. Malaeb, Y. Ishida, T. Sasagawa, H. Sakamoto, T. Takeuchi, T. Tohyama, and S. Shin, *Point nodes persisting far beyond Tc in Bi2212*, *Nature Communications* **6** (2015), no. 1 7699, [arXiv:1507.04312].

[152] T. J. Reber, S. Parham, N. C. Plumb, Y. Cao, H. Li, Z. Sun, Q. Wang, H. Iwasawa, M. Arita, J. S. Wen, Z. J. Xu, G. D. Gu, Y. Yoshida, H. Eisaki, G. B. Arnold, and D. S. Dessau, *Pairing, pair-breaking, and their roles in setting the Tc of cuprate high temperature superconductors*, 2015.

[153] H. Li, X. Zhou, S. Parham, T. J. Reber, H. Berger, G. B. Arnold, and D. S. Dessau, *Coherent organization of electronic correlations as a mechanism to enhance and stabilize high-T C cuprate superconductivity*, *Nature Communications* **9** (2018), no. 1 26.

[154] K. M. Bastiaans, D. Chatzopoulos, J.-F. Ge, D. Cho, W. O. Tromp, J. M. van Ruitenbeek, M. H. Fischer, P. J. de Visser, D. J. Thoen, E. F. C. Driessen, T. M. Klapwijk, and M. P. Allan, *Direct evidence for Cooper pairing without a spectral gap in a disordered superconductor above T_{C}*, *Science* **374** (2021), no. 6567 608–611, [arXiv:2101.08535].

[155] W. O. Tromp, T. Benschop, J.-F. Ge, I. Battisti, K. M. Bastiaans, D. Chatzopoulos, A. Vervloet, S. Smit, E. van Heumen, M. S. Golden, Y. Huang, T. Kondo, Y. Yin, J. E. Hoffman, M. A. Sulangi, J. Zaanen, and M. P. Allan, *Puddle formation, persistent gaps, and non-mean-field breakdown of superconductivity in overdoped (Pb,Bi)2Sr2CuO6+{\delta}*, *Nature Materials* **22** (2023), no. 6 703–709, [arXiv:2205.09740].

[156] J. Maldacena and D. Stanford, *Comments on the Sachdev-Ye-Kitaev model*, *Physical Review D* **94** (2016), no. 10 106002, [arXiv:1604.07818].

[157] T. Tummuru, S. Plugge, and M. Franz, *Josephson effects in twisted cuprate bilayers*, *Physical Review B* **105** (2022), no. 6 064501.

[158] A. A. Golubov, M. Y. Kupriyanov, and E. Il'Ichev, *The current-phase relation in josephson junctions*, *Reviews of modern physics* **76** (2004), no. 2 411.

[159] G. A. Inkof, *The quantum critical syk superconductor, lifshitz points and their holographic duals*, *PhD Thesis, University of Karlsruhe* (2022).

[160] J. M. B. Lopes dos Santos, N. M. R. Peres, and A. H. Castro Neto, *Graphene bilayer with a twist: Electronic structure*, *Phys. Rev. Lett.* **99** (Dec, 2007) 256802.

[161] E. Suárez Morell, J. D. Correa, P. Vargas, M. Pacheco, and Z. Barticevic, *Flat bands in slightly twisted bilayer graphene: Tight-binding calculations*, *Phys. Rev. B* **82** (Sep, 2010) 121407.

[162] K. Kim, A. DaSilva, S. Huang, B. Fallahazad, S. Larentis, T. Taniguchi, K. Watanabe, B. J. LeRoy, A. H. MacDonald, and E. Tutuc, *Tunable moiré bands and strong correlations in small-twist-angle bilayer graphene*, *Proceedings of the National Academy of Sciences* **114** (2017), no. 13 3364–3369.

[163] J. Liu, J. Liu, and X. Dai, *Pseudo landau level representation of twisted bilayer graphene: Band topology and implications on the correlated insulating phase*, *Phys. Rev. B* **99** (Apr, 2019) 155415.

[164] Z. Song, Z. Wang, W. Shi, G. Li, C. Fang, and B. A. Bernevig, *All magic angles in twisted bilayer graphene are topological*, *Phys. Rev. Lett.* **123** (Jul, 2019) 036401.

[165] G. Tarnopolsky, A. J. Kruchkov, and A. Vishwanath, *Origin of magic angles in twisted bilayer graphene*, *Phys. Rev. Lett.* **122** (Mar, 2019) 106405.

[166] X. Lu, P. Stepanov, W. Yang, M. Xie, M. A. Aamir, I. Das, C. Urgell, K. Watanabe, T. Taniguchi, G. Zhang, A. Bachtold, A. H. MacDonald, and D. K. Efetov, *Superconductors, orbital magnets and correlated states in magic-angle bilayer graphene*, *Nature* **574** (Oct., 2019) 653–657.

[167] R. Ojajärvi, T. Hyart, M. A. Silaev, and T. T. Heikkilä, *Competition of electron-phonon mediated superconductivity and stoner magnetism on a flat band*, *Phys. Rev. B* **98** (Aug, 2018) 054515.

[168] H. Isobe, N. F. Q. Yuan, and L. Fu, *Unconventional superconductivity and density waves in twisted bilayer graphene*, *Phys. Rev. X* **8** (Dec, 2018) 041041.

[169] F. Wu, A. H. MacDonald, and I. Martin, *Theory of phonon-mediated superconductivity in twisted bilayer graphene*, *Phys. Rev. Lett.* **121** (Dec, 2018) 257001.

[170] T. J. Peltonen, R. Ojajärvi, and T. T. Heikkilä, *Mean-field theory for superconductivity in twisted bilayer graphene*, *Phys. Rev. B* **98** (Dec, 2018) 220504.

[171] V. Kozii, H. Isobe, J. W. F. Venderbos, and L. Fu, *Nematic superconductivity stabilized by density wave fluctuations: Possible application to twisted bilayer graphene*, *Phys. Rev. B* **99** (Apr, 2019) 144507.

[172] M. Yankowitz, S. Chen, H. Polshyn, Y. Zhang, K. Watanabe, T. Taniguchi, D. Graf, A. F. Young, and C. R. Dean, *Tuning superconductivity in twisted bilayer graphene*, *Science* **363** (2019), no. 6431 1059–1064.

[173] T. Hazra, N. Verma, and M. Randeria, *Bounds on the superconducting transition temperature: Applications to twisted bilayer graphene and cold atoms*, *Phys. Rev. X* **9** (Sep, 2019) 031049.

[174] X. Hu, T. Hyart, D. I. Pikulin, and E. Rossi, *Geometric and conventional contribution to the superfluid weight in twisted bilayer graphene*, *Phys. Rev. Lett.* **123** (Dec, 2019) 237002.

[175] F. Xie, Z. Song, B. Lian, and B. A. Bernevig, *Topology-bounded superfluid weight in twisted bilayer graphene*, *Phys. Rev. Lett.* **124** (Apr, 2020) 167002.

[176] A. Julku, T. J. Peltonen, L. Liang, T. T. Heikkilä, and P. Törmä, *Superfluid weight and berezinskii-kosterlitz-thouless transition temperature of twisted bilayer graphene*, *Phys. Rev. B* **101** (Feb, 2020) 060505.

[177] L. Van Hove, *The occurrence of singularities in the elastic frequency distribution of a crystal*, *Phys. Rev.* **89** (Mar, 1953) 1189–1193.

[178] G. Li, A. Luican, J. M. B. Lopes dos Santos, A. H. Castro Neto, A. Reina, J. Kong, and E. Y. Andrei, *Observation of van Hove singularities in twisted graphene layers*, *Nature Physics* **6** (Feb, 2010) 109–113.

[179] A. Kerelsky, L. J. McGilly, D. M. Kennes, L. Xian, M. Yankowitz, S. Chen, K. Watanabe, T. Taniguchi, J. Hone, C. Dean, A. Rubio, and A. N. Pasupathy, *Maximized electron interactions at the magic angle in twisted bilayer graphene*, *Nature* **572** (Aug, 2019) 95–100.

[180] Y. Choi, J. Kemmer, Y. Peng, A. Thomson, H. Arora, R. Polski, Y. Zhang, H. Ren, J. Alicea, G. Refael, F. von Oppen, K. Watanabe, T. Taniguchi, and S. Nadj-Perge, *Electronic correlations in twisted bilayer graphene near the magic angle*, *Nature Physics* **15** (Nov, 2019) 1174–1180.

[181] M. Crommie, C. P. Lutz, and D. Eigler, *Imaging standing waves in a two-dimensional electron gas*, *Nature* **363** (1993), no. 6429 524–527.

[182] T. Jamneala, V. Madhavan, W. Chen, and M. F. Crommie, *Scanning tunneling spectroscopy of transition-metal impurities at the surface of gold*, *Physical Review B* **61** (2000), no. 15 9990.

[183] V. Madhavan, W. Chen, T. Jamneala, M. F. Crommie, and N. S. Wingreen, *Local spectroscopy of a kondo impurity: Co on au (111)*, *Physical Review B* **64** (2001), no. 16 165412.

[184] J. Hoffman, K. McElroy, D.-H. Lee, K. Lang, H. Eisaki, S. Uchida, and J. Davis, *Imaging quasiparticle interference in Bi2Sr2CaCu2O8+ δ*, *Science* **297** (2002), no. 5584 1148–1151.

[185] T. Costi, L. Bergqvist, A. Weichselbaum, J. von Delft, T. Micklitz, A. Rosch, P. Mavropoulos, P. H. Dederichs, F. Mallet, L. Saminadayar, et al., *Kondo decoherence: finding the right spin model for iron impurities in gold and silver*, *Physical review letters* **102** (2009), no. 5 056802.

[186] M. Ternes, A. J. Heinrich, and W.-D. Schneider, *Spectroscopic manifestations of the kondo effect on single adatoms*, *Journal of Physics: Condensed Matter* **21** (2008), no. 5 053001.

[187] L. Bogani and W. Wernsdorfer, *Molecular spintronics using single-molecule magnets*, *Nature materials* **7** (2008), no. 3 179–186.

[188] A. C. Hewson, *The Kondo Problem to Heavy Fermions*. Cambridge Studies in Magnetism. Cambridge University Press, 1993.

[189] P. G. Derry, A. K. Mitchell, and D. E. Logan, *Quasiparticle interference from magnetic impurities*, *Physical Review B* **92** (2015), no. 3 035126.

[190] A. K. Mitchell, P. G. Derry, and D. E. Logan, *Multiple magnetic impurities on surfaces: Scattering and quasiparticle interference*, *Physical Review B* **91** (2015), no. 23 235127.

[191] G. Mihailescu, S. Campbell, and A. K. Mitchell, *Thermometry of strongly correlated fermionic quantum systems using impurity probes*, *Physical Review A* **107** (2023), no. 4 042614.

[192] J.-H. Chen, L. Li, W. G. Cullen, E. D. Williams, and M. S. Fuhrer, *Tunable kondo effect in graphene with defects*, *Nature Physics* **7** (2011), no. 7 535–538.

[193] M. Vojta, L. Fritz, and R. Bulla, *Gate-controlled kondo screening in graphene: Quantum criticality and electron-hole asymmetry*, *EPL (Europhysics Letters)* **90** (2010), no. 2 27006.

[194] L. Fritz and M. Vojta, *The physics of Kondo impurities in graphene*, *Reports on Progress in Physics* **76** (feb, 2013) 032501.

[195] A. K. Mitchell and L. Fritz, *Kondo effect with diverging hybridization: Possible realization in graphene with vacancies*, *Physical Review B* **88** (2013), no. 7 075104.

[196] A. K. Mitchell, D. Schuricht, M. Vojta, and L. Fritz, *Kondo effect on the surface of three-dimensional topological insulators: Signatures in scanning tunneling spectroscopy*, *Physical Review B* **87** (2013), no. 7 075430.

[197] A. K. Mitchell and L. Fritz, *Kondo effect in three-dimensional dirac and weyl systems*, *Physical Review B* **92** (2015), no. 12 121109.

[198] J. Martinek, Y. Utsumi, H. Imamura, J. Barnaś, S. Maekawa, J. König, and G. Schön, *Kondo effect in quantum dots coupled to ferromagnetic leads*, *Physical review letters* **91** (2003), no. 12 127203.

[199] M. R. Calvo, J. Fernandez-Rossier, J. J. Palacios, D. Jacob, D. Natelson, and C. Untiedt, *The kondo effect in ferromagnetic atomic contacts*, *Nature* **458** (2009), no. 7242 1150–1153.

[200] E. Müller-Hartmann and J. Zittartz, *Kondo effect in superconductors*, *Physical Review Letters* **26** (1971), no. 8 428.

[201] A. Polkovnikov, S. Sachdev, and M. Vojta, *Impurity in a d-wave superconductor: Kondo effect and stm spectra*, *Physical Review Letters* **86** (2001), no. 2 296.

[202] A. Kolezhuk, S. Sachdev, R. R. Biswas, and P. Chen, *Theory of quantum impurities in spin liquids*, *Physical Review B* **74** (2006), no. 16 165114.

[203] M. Vojta, A. K. Mitchell, and F. Zschocke, *Kondo impurities in the kitaev spin liquid: Numerical renormalization group solution and gauge-flux-driven screening*, *Physical review letters* **117** (2016), no. 3 037202.

[204] W.-Y. He and P. A. Lee, *Magnetic impurity as a local probe of the $U(1)$ quantum spin liquid with spinon fermi surface*, *Physical Review B* **105** (2022), no. 19 195156.

[205] D. May, P.-W. Lo, K. Deltenre, A. Henke, J. Mao, Y. Jiang, G. Li, E. Y. Andrei, G.-Y. Guo, and F. B. Anders, *Modeling of the gate-controlled kondo effect at carbon point defects in graphene*, *Phys. Rev. B* **97** (Apr, 2018) 155419.

[206] Z.-D. Song and B. A. Bernevig, *Magic-angle twisted bilayer graphene as a topological heavy fermion problem*, *Physical review letters* **129** (2022), no. 4 047601.

[207] H. Hu, B. A. Bernevig, and A. M. Tsvelik, *Kondo lattice model of magic-angle twisted-bilayer graphene: Hund's rule, local-moment fluctuations, and low-energy effective theory*, *arXiv preprint arXiv:2301.04669* (2023).

[208] H. Hu, G. Rai, L. Crippa, J. Herzog-Arbeitman, D. Călugăru, T. Wehling, G. Sangiovanni, R. Valenti, A. Tsvelik, and B. Bernevig, *Symmetric kondo lattice states in doped strained twisted bilayer graphene*, *arXiv preprint arXiv:2301.04673* (2023).

[209] G.-D. Zhou and Z.-D. Song, *Kondo resonance, pomeranchuk effect, and heavy fermi liquid in twisted bilayer graphene–a numerical renormalization group study, arXiv preprint arXiv:2301.04661* (2023).

[210] B. Lian, Z. Wang, and B. A. Bernevig, *Twisted bilayer graphene: A phonon-driven superconductor*, *Phys. Rev. Lett.* **122** (Jun, 2019) 257002.

[211] A. Chandrasekaran, A. Shtyk, J. J. Betouras, and C. Chamon, *Catastrophe theory classification of fermi surface topological transitions in two dimensions*, *Phys. Rev. Research* **2** (Mar, 2020) 013355.

[212] J. Kondo, *Theory of dilute magnetic alloys*, in *Solid State Physics*, pp. 183–281. Elsevier, 1970.

[213] A. Bayat, P. Sodano, and S. Bose, *Negativity as the entanglement measure to probe the kondo regime in the spin-chain kondo model*, *Physical Review B* **81** (2010), no. 6 064429.

[214] A. K. Mitchell, M. Becker, and R. Bulla, *Real-space renormalization group flow in quantum impurity systems: Local moment formation and the kondo screening cloud*, *Physical Review B* **84** (2011), no. 11 115120.

[215] I. V Borzenets, J. Shim, J. C. Chen, A. Ludwig, A. D. Wieck, S. Tarucha, H.-S. Sim, and M. Yamamoto, *Observation of the kondo screening cloud*, *Nature* **579** (2020), no. 7798 210–213.

[216] J. R. Schrieffer and P. A. Wolff, *Relation between the anderson and kondo hamiltonians*, *Physical Review* **149** (1966), no. 2 491.

[217] J. B. Rigo and A. K. Mitchell, *Machine learning effective models for quantum systems*, *Physical Review B* **101** (2020), no. 24 241105.

[218] P. Anderson, *A poor man's derivation of scaling laws for the kondo problem*, *Journal of Physics C: Solid State Physics* **3** (1970), no. 12 2436.

[219] K. G. Wilson, *The renormalization group: Critical phenomena and the kondo problem*, *Reviews of modern physics* **47** (1975), no. 4 773.

[220] R. Bulla, T. A. Costi, and T. Pruschke, *Numerical renormalization group method for quantum impurity systems*, *Reviews of Modern Physics* **80** (2008), no. 2 395.

[221] K. Chen and C. Jayaprakash, *The kondo effect in pseudo-gap fermi systems: a renormalization group study*, *Journal of Physics: Condensed Matter* **7** (1995), no. 37 L491.

[222] R. Bulla, T. Pruschke, and A. Hewson, *Anderson impurity in pseudo-gap fermi systems*, *Journal of Physics: Condensed Matter* **9** (1997), no. 47 10463.

[223] F. B. Anders and A. Schiller, *Spin precession and real-time dynamics in the kondo model: Time-dependent numerical renormalization-group study*, *Physical Review B* **74** (2006), no. 24 245113.

[224] A. Weichselbaum and J. von Delft, *Sum-rule conserving spectral functions from the numerical renormalization group*, *Physical review letters* **99** (2007), no. 7 076402.

[225] R. Bulla, A. C. Hewson, and T. Pruschke, *Numerical renormalization group calculations for the self-energy of the impurity anderson model*, *Journal of Physics: Condensed Matter* **10** (1998), no. 37 8365.

[226] W. C. Oliveira and L. N. Oliveira, *Generalized numerical renormalization-group method to calculate the thermodynamical properties of impurities in metals*, *Physical Review B* **49** (1994), no. 17 11986.

[227] R. Bulla, N.-H. Tong, and M. Vojta, *Numerical renormalization group for bosonic systems and application to the sub-ohmic spin-boson model*, *Physical review letters* **91** (2003), no. 17 170601.

[228] R. Žitko and T. Pruschke, *Energy resolution and discretization artifacts in the numerical renormalization group*, *Physical Review B* **79** (2009), no. 8 085106.

[229] A. K. Mitchell, M. R. Galpin, S. Wilson-Fletcher, D. E. Logan, and R. Bulla, *Generalized wilson chain for solving multichannel quantum impurity problems*, *Physical Review B* **89** (2014), no. 12 121105.

[230] K. M. Stadler, A. K. Mitchell, J. von Delft, and A. Weichselbaum, *Interleaved numerical renormalization group as an efficient multiband impurity solver*, *Physical Review B* **93** (2016), no. 23 235101.

[231] S.-S. B. Lee, F. B. Kugler, and J. von Delft, *Computing local multipoint correlators using the numerical renormalization group*, *Physical Review X* **11** (2021), no. 4 041007.

[232] J. B. Rigo and A. K. Mitchell, *Automatic differentiable numerical renormalization group*, *Physical Review Research* **4** (2022), no. 1 013227.

[233] "Sometimes Eqs. 4.17 and 4.18 are written to include a rescaling of H_N at each step N [220], but we omit those factors here for brevity.."

[234] P. Nozieres and A. Blandin, *Kondo effect in real metals*, *Journal de Physique* **41** (1980), no. 3 193–211.

[235] A. O. Gogolin, *On the theory of the Kondo effect in two-dimensional metals*, *Zeitschrift für Physik B Condensed Matter* **92** (mar, 1993) 55–59.

[236] A. K. Zhuravlev and V. Y. Irkhin, *Kondo effect in the presence of van hove singularities: A numerical renormalization group study*, *Physical Review B* **84** (dec, 2011) 245111.

[237] A. Zhuravlev, A. Anokhin, and V. Y. Irkhin, *One-and two-channel kondo model with logarithmic van hove singularity: A numerical renormalization group solution*, *Physics Letters A* **382** (2018), no. 7 528–533.

[238] D. E. Logan, A. P. Tucker, and M. R. Galpin, *Common non-fermi liquid phases in quantum impurity physics*, *Physical Review B* **90** (2014), no. 7 075150.

[239] A. K. Mitchell, M. Vojta, R. Bulla, and L. Fritz, *Quantum phase transitions and thermodynamics of the power-law Kondo model*, *Physical Review B* **88** (nov, 2013) 195119.

[240] C. Gonzalez-Buxton and K. Ingersent, *Renormalization-group study of Anderson and Kondo impurities in gapless fermi systems*, *Phys. Rev. B* **57** (Jun, 1998) 14254–14293.

[241] M. Vojta and L. Fritz, *Upper critical dimension in a quantum impurity model: Critical theory of the asymmetric pseudogap Kondo problem*, *Phys. Rev. B* **70** (Sep, 2004) 094502.

[242] L. Fritz and M. Vojta, *Phase transitions in the pseudogap anderson and Kondo models: Critical dimensions, renormalization group, and local-moment criticality*, *Phys. Rev. B* **70** (Dec, 2004) 214427.

[243] P. Igoshev and V. Y. Irkhin, *Giant van hove density of states singularities and anomalies of electron and magnetic properties in cubic lattices*, *Physics of Metals and Metallography* **120** (2019) 1282–1290.

[244] P. Igoshev and V. Y. Irkhin, *Giant density-of-states van hove singularities in the face-centered cubic lattice*, *Physics Letters A* **438** (2022) 128107.

[245] A. Chandrasekaran and J. J. Betouras, *A practical method to detect, analyze, and engineer higher order van hove singularities in multi-band hamiltonians*, *Advanced Physics Research* (2023).

Samenvatting

Vaste stoffen bestaan uit elektronen en ionen. De meeste vaste stoffen kunnen effectief worden gemodelleerd met een theorie waarin de beweging van de elektronen allemaal als onafhankelijk van elkaar kan worden beschouwd. Dit proefschrift houdt zich bezig met enkele gevallen waarin deze beschrijving onvermijdelijk faalt, en meerdere-deeltjes-interacties de lage-energiefysica domineren. Dergelijke systemen zijn veel moeilijker te bestuderen. Soms kan vooruitgang worden geboekt met behulp van geavanceerde numerieke technieken, of door creatief geconstrueerde, precies oplosbare speelgoedmodellen.

Dit laatste is de benadering van het Sachdev-Ye-Kitaev (SYK)-model, dat een kwantumdot beschrijft met een groot aantal fermionen erop, die allemaal met elkaar interacteren door middel van een gerandomiseerde interactie met vier fermionen. De eenvoud van het model verhult een overvloed aan exotische verschijnselen die voortkomen uit een emergente conforme symmetrie in het infrarood, met eclectische toepassingen van vreemde metalen tot zwarte gaten. Door zogenaamde holografische dualiteit kan de lage-energietheorie van het model, die voortkomt uit het verbreken van de bovengenoemde conforme symmetrie, in kaart worden gebracht via verstoringen van een bijna AdS_2 ruimtetijd.

Eén van die verschijnselen staat bekend als maximale chaos. Het SYK-model verzadigt een grens aan de snelheid waarmee in een kwantumsysteem verstoringen kunnen dissiperen in zijn vrijheidsgraden. Dit kenmerk blijft bestaan, zelfs als men bepaalde gewijzigde versies van het SYK-model construeert, zoals het bipartiete SYK-model. De mate van chaos verandert niet, zelfs niet als de schaaldimensies van de samenstellende fermionen worden veranderd, zoals beschreven in hoofdstuk 2. De eerste subleidende correctie van de chaos exponent blijft ook onafhankelijk te zijn van de schaaldimensie.

Wanneer twee identieke kopieën van het SYK-model aan elkaar worden gekoppeld door een tunnelinteractie, bij lage temperatuur beschrijft het holografische duaal de ruimtetijd van een wormgat. Een op een dergelijke manier gemaakt Josephsoncontact kan worden bestudeerd met behulp van de SYK-versie van het elektron-fonon-gekoppelde systeem, dat bekend staat als het Yukawa SYK-model. Supergeleiding in het Yukawa SYK-model vindt plaats bij lage temperaturen als het systeem tijdinversie niet schendt. In hoofdstuk 3 wordt aangetoond dat de niet-supergeleidende

toestand de correcte niet-analytische afhankelijkheid van de "gap" vertoont van de sterkte van de tunnelinteractie, kenmerkend voor de wormgattoestand. Er wordt aangetoond dat de supergeleidende toestand effectief kan worden beschreven door een twee-vloeistoffenmodel, waarbij de Cooperparen onafhankelijk aan beide zijden leven, terwijl excitaties van ongebonden elektronen nog steeds de wormgattoestand vormen.

Als tegenpool van de hyperbolische geometrie van de AdS_2 ruimte, hebben we in het tweede deel van dit proefschrift een systeem beschouwd waarvan het niet-interagerende fermi-oppervlak is samengesteld uit een familie van hyperbolen. In gedraaid dubbellaags grafeen voor kleine draaihoeken is dit te zien in de vorm van van Hove-singulariteiten, die precies onder de magische hoek een hogere orde krijgen. In hoofdstuk 4 wordt aangetoond dat een kenmerk voor het waarnemen van het effect ervan in een realistische fysieke omgeving de reactie is op een magnetische onzuiverheid. De onzuiverheidsentropie vertoont duidelijke kenmerken nabij de magische hoek, en toont stromingen naar de verschillende soorten vaste punten die beschikbaar zijn in de faseruimte van het systeem. Totdat de magische hoek is bereikt, werkt het bestaan van de Dirac-kegel bij de laagste energieën als een afstootmiddel voor Kondo-screening, wat zich manifesteert als een entropie van log2 per onzuiverheid. Bij de magische hoek domineert de verschijning van de hogere orde Van Hove-singulariteit de bandstructuur, en dit leidt tot een versterkt Kondo-effect tot de laagst mogelijke energieschalen.

Summary

Solids are composed of electrons and ions. Most solids can be effectively modeled by a theory in which the motion of the electrons can all be considered independent to each other. This thesis is concerned with some cases where that description fails, and many body interactions dominate the low energy physics. Such systems are far more difficult to study, and sometimes progress can be made either with sophisticated numerical tools, or by creatively constructed exactly solvable toy models.

The latter is the approach taken by the Sachdev-Ye-Kitaev (SYK) model, which describes a quantum dot with a large number of fermions on it, all interacting with each other by means of a randomized four-fermion interaction. The simplicity of the model belies a plethora of exotic phenomena that arise from an emergent conformal symmetry in the infrared, with eclectic applications from strange metals to black holes. Through the holographic duality, the low energy theory of the model arising from the breaking of the aforementioned conformal symmetry can be mapped to perturbations of a nearly AdS_2 spacetime.

One such phenomenon is known as maximal chaos. The SYK model saturates a bound on the rate at which a quantum system can dissipate perturbations into its degrees of freedom. This feature persists even when one constructs certain modified versions of the SYK model, such as the bipartite SYK model, and the rate of chaos doesn't change even when the scaling dimensions of the constituent fermions are changed as is described in chapter 2. The first subleading correction to the chaos exponent is also found to be independent of the scaling dimension.

When two identical copies of the SYK model are coupled together by a tunneling interaction, its holographic dual describes a wormhole spacetime at low temperature. A Josephson contact made in such a way can be studied using the SYK version of the electron-phonon coupled system, which is known as the Yukawa SYK model. Superconductivity in the Yukawa SYK model occurs at low temperatures if time reversal symmetry is present. In chapter 3, it was shown that the non-superconducting state shows the correct non-analytic dependence of the gap on the strength of the tunneling interaction, characteristic of the wormhole state. The superconducting state was shown to be effectively described by a two-fluid model, where the Cooper pairs live independently on the two sides, while single electron excitations still form the wormhole state.

In juxtaposition to the hyperbolic geometry of the AdS_2 space, we consider a system whose non-interacting fermi surface was composed of a family of hyperbolae in the second part of this thesis. In twisted bilayer graphene for small twists, this is seen in the form of van Hove singularities, which turn higher order at precisely the magic angle. In chapter 4, a probe for sensing its effect in a realistic physical setting was shown to be the response of a magnetic impurity. The impurity entropy shows distinct signatures near the magic angle, showing flows to the different kinds of fixed points available in the phase space of the system. Until the magic angle is reached, the existence of the Dirac cone at the lowest energies acts as a deterrent for Kondo screening, which manifests itself as a log 2 entropy per impurity. At the magic angle, the appearance of the higher order van Hove singularity dominates the band structure, and it leads to an enhanced Kondo effect until the lowest energy scales possible.

List of Publications

1. " Lyapunov exponents in a Sachdev-Ye-Kitaev-type model with population imbalance in the conformal limit and beyond ",

   A. S. Shankar, M.Fremling, S. Plugge and L. Fritz
   Phys. Rev. D, 108, 094039 (2023).

2. " Kondo effect in twisted bilayer graphene ",

   A. S. Shankar, D. O. Oriekhov, Andrew K. Mitchell, and L. Fritz
   Phys. Rev. B, 107, 245102 (2023).

Curriculum Vitae

I was born on September 26th, 1996 in Chennai, a big city in the south of India. After finishing high school, I went to West Bengal for a five-year integrated Bachelor-Master program in Physics at the Indian Institute of Technology, Kharagpur.

During this period, I took courses in several areas of physics and engineering, including high energy physics and gravitational physics, with my favorite being condensed matter and statistical physics. I was also fortunate to get an early start at doing my own research by being selected for several internships throughout my bachelor and master studies. With Prof. Pinaki Sengupta at NTU Singapore, I worked on writing my first quantum Monte Carlo code to investigate the Heisenberg XXZ model on ladder-like systems. I then worked briefly with Prof. Barbara Terhal and Prof. Fabian Hassler on DMRG simulations at RTWH aachen, and then on numerical and analytical studies on the Anderson model on the Bethe lattice with Prof. Antonello Scardicchio at the ICTP, Trieste, looking for signatures of anomalous diffusion. I concluded my master studies with a thesis titled "Disordered Superconductors", working with Prof. Sudhansu Sekhar Mandal.

I started my PhD at Leiden university in the Quantum matter group of Prof. Jan Zaanen and Prof. Koenraad Schalm in August 2019. After a short stint there, I moved to the group of Prof. Vadim Cheianov in April 2021. It was also at this time that I started working very closely with Prof. Lars Fritz and his group at Utrecht University.

As the early years of my PhD programme were marred by the coronavirus pandemic, I attended several condensed matter schools online, including editions of the Princeton PSSC summer school and the Maglab winter school. After the pandemic ended, I was able to present my work at several schools and conferences, including poster presentations in Trieste, Italy, at the ICTP conference "From quantum criticality to flat bands", at the school "Emergence of quantum phases in novel materials", at CSIC, Madrid, Spain, at the Veldhoven Physics conference in the Netherlands, and an online talk at the APS March meeting in 2023, among others. I also had the opportunity to TA several undergraduate and graduate courses, an in particular to write a set of extensive lecture notes on Information Geometry with Prof. Subodh Patil.

After the defense of my PhD, I will move on to begin a Postdoctoral position at the International Center for Theoretical Physics(ICTP) in Trieste, Italy.

Acknowledgements

First and foremost, I would like to thank my promotors Prof. Vadim Cheianov and Prof. Koenraad Schalm for giving me the independence to carve my own path, even though it might have been slightly unconventional. I'm very thankful to Vadim for his infinite patience with my questions and for addressing them sincerely even if they might have been trivial at times. To Koenraad I'm thankful for teaching me to improve my scientific rigor and for the importance he taught me to place on communicating my results well. Thank you very much.

I'm most greatly indebted to Prof. Lars Fritz, his contribution to this work goes far beyond his supervision of the two published papers that form parts of this thesis. I'm exceedingly grateful to him for welcoming me into his group, and for his wonderful mentorship over the years. I'm also thankful to Lars for introducing me to Prof. Andrew K. Mitchell, who I greatly enjoyed collaborating with. I hope this collaboration will last for quite some time to come.

I'm also very grateful to the PhD students and postdocs that I worked with in Leiden and in Utrecht - Dima Oriekhov, Mikael Fremling and Stephan Plugge. I am also particularly grateful to the several intense discussions I had with Nicolas Chagnet over physics and on numerics in general. I would also like to acknowledge master students Alina Melissakis and Nina Doerfler whose theses I helped co-supervise- I learned quite a lot from this experience.

I extend thanks next to the several friends I made along the way. I will always have a special place for my covid-housemate Alicja Dutkiewicz, and my post-covid housemate Dimitrios Krommydas, with whom I felt that family was always close by.

I also thank Floris Balm, Luca Barbera, Alexander Barnaveli, Norman Bluemel, Meike Bos, Aleksandar Bukva, Zhenya Cheipesh, Jose Collado, Tjeerd de Leede, David Dechant, Emanuele di Salvio, Alvaro Donis-Vela, Patrick Emonts, Inci Erbilen, Matthias Flor, Ireth Garcia-Aguilar, Alice Garoffolo, Peter George, Joren Harms, Yaroslav Herasymenko, Ludwig Hoffman, Stef Koenis, Ilse Kuijf, Gal Lemut, Samadarshi Maity, Savvas Malikis, Simon Marshall, Kirsten Martens, Kamil Matuszelanski, Anna Negro, Vladimir Ohanesjan, Maialen Ortego-Larrazabal, Michal Pacholski, Adrian Perez, Stefano Polla, Kshiti Sneh Rai, Midas Ratsma, Philippe Sabella-Garnier, Katerina Saiti, Kolya Semenyakin, Tereza Vakhtel, Vova Zakharov and Masha Zakharova for their warm company, and for discussions both physics and otherwise.

I'm also very thankful to my friends from India - Mohit Chajjed, Mohit Dhariwal, Muthu Ganesh, Philip Jacob, Viraj Jangam, Daksh Khanter, Dilip Kumar, Pranai Kumar, Praveen PR, Saloni Priya, Suvrat Rao, Darvin Sai Teja Reddy, Baibhaw Kumar Singh, Tulja Varun for keeping me company with frequent phone calls, especially during the pandemic.

Lastly, I thank my family - Amma, Appa, Aparna and Paati-Thatha for your support, and for being understanding of my absence from home.